IUSS
Scuola Universitaria Superiore Pavia

Scuola Universitaria Superiore IUSS Pavia

DOCTORAL THESIS

Isogeometric mortar methods with applications in contact mechanics

by Ericka Brivadis

A thesis submitted in fulfillment of the requirements for the degree of Doctor of Philosophy

in

Computational Mechanics and Advanced Materials

XXVIII Cycle (2012-2015)

Supervisor: Annalisa Buffa IMATI Pavia

Declaration of authorship

I, Ericka Brivadis, declare that this thesis entitled, "Isogeometric mortar methods with applications in contact mechanics" and the work presented in it are my own. I confirm that:

- This work was done wholly or mainly while in candidature for a research degree at this University.
- Where any part of this thesis has previously been submitted for a degree or any other qualification at this University or any other institution.
- Where I have consulted the published work of others, this is always clearly attributed.
- Where I have quoted from the work of others, the source is always given. With the exception of such quotations, this thesis is entirely my own work.
- I have acknowledged all main sources of help.
- Where the thesis is based on work done by myself jointly with others, it is clearly mentioned.
- Either none of this work has been published before submission, or parts of this work have been published as: [17] and [18].

Signed: Brivadis

Date: 31/10/2016

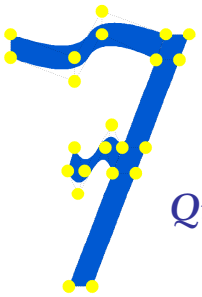

Quotes

"Better late than never." Drake

"The only true wisdom is to know that you know nothing." Socrate

"If your eyes are opened, you'll see the things worth seeing." Rumi

"I'm not telling you it is going to be easy, I'm telling you it's going to be worth it."
Williams Art

"Believe you can and you're halfway there." Theodore Roosevelt

"Education is the most powerful weapon which you can use to change the world."
Nelson Mandela

"And most important, have the courage to follow your heart and intuition, they somehow already know what you truly want to become. [...]
Stay hungry, stay foolish." Steve Jobs

Abstract

IsoGeometric Analysis (IGA) has been immediately considered as a promising technique to approximate Partial Differential Equations (PDEs) thanks to its most important feature: the use of smooth basis functions. IGA generates accurate and even exact geometry approximations, but generally at the price of a computational domain which is split into numerous patches. Thus, one needs efficient methods to treat the patch coupling. Weak couplings are privileged compared to strong point-wise ones as they allow the flexibility in the choice of the patch meshes as well as of the patch approximation space degrees.

This research work concerns the study of some weak coupling methods and their applications to contact mechanics. After an introductory chapter, Chapters 2 and 3 are devoted to the definition and the study of the mortar method for IGA, while Chapters 4 and 5 to their applications in the numerical approximation of contact mechanics.

Relying on the mortar mathematical background that exists with Finite Element Methods (FEMs), mortar methods have been studied theoretically as well as numerically using IGA in Chapter 2. Two multiplier spaces are proved to be stable and to provide best approximation results. Both are spline spaces defined on the slave boundary mesh but of different orders.

Once suitable multiplier spaces have been found, the most critical issue in the design of a mortar method is the evaluation of the so-called mortar integrals, i.e., the integrals of product of functions living on different meshes. A study on different integration strategies is presented in Chapter 3. An approximate integration strategy based on two existing quadratures gives optimal results, and as expected the exact integration strategy based on the construction of suitable quadrature formulae. We note that obtaining this latter requires the definition of a third mesh, called merged mesh, built during an expensive process known as segmentation process.

These optimal mortar methods inspired the treatment of a more challenging interface problem: the frictionless unilateral contact problem with

initial gap. In Chapter 4, in the design of optimal numerical contact methods, mixed methods are proposed to treat rigid-deformable contact problems, i.e., the contact between an elastic body with a rigid ground. Problem formulation, discretization, constraint enforcement methods and resolution strategies are discussed. Finally, in Chapter 5, we propose variationally consistent methods based on the mortar methods defined above to approach deformable-deformable contact problems, i.e., the contact between two elastic bodies. The optimality of the contact methods is shown on different benchmarks.

Italian abstract

L'Analisi IsoGeometrica (IGA) è stata considerata fin da subito come promettente per l'approssimazione delle equazione ai derivati parziali perché si basa su funzioni di base ad elevata continuità. Il metodo IGA genera delle geometrie precise o esatte, ma in generale questo comporta la decomposizione del dominio computazionale in diversi sottodomini, chiamati patches. È quindi necessario avere metodi efficaci per incollare questi diversi sottodomini. I metodi misti come i metodi mortar sono privilegiati rispetto agli altri metodi, poiché permettono la flessibilità nella scelta delle griglie nei diversi patches e del grado polinomiale dei rispettivi spazi di approssimazione.

Questo lavoro di ricerca riguarda lo studio di metodi variazionali di accoppiamento fra patches e le loro applicazioni alla meccanica del contatto. Dopo un capitolo di introduzione, i Capitoli 2 e 3 sono dedicati alla definizione ed allo studio del metodo mortar per l'IGA, mentre i Capitoli 4 e 5 all'applicazione numerica in meccanica del contatto.

Basandosi sulle conoscenze matematiche già esistenti nel contesto del metodo degli elementi finiti, i metodi mortar sono stati studiati sia teoricamente che numericamente usando IGA nel Capitolo 2. Dimostreremo che due spazi di moltiplicatori sono stabili e che hanno proprietà di approssimazione ottimali. Entrambi sono spazi di splines definiti sul bordo della griglia slave ma di ordini diversi.

Una volta scelti adeguatamente gli spazi di moltiplicatori, rimane da affrontare il problema della la valutazione degli integrali mortar, cioè degli integrali che contengono il prodotto di funzioni definite su griglie diverse. Uno studio fatto su diverse strategie di integrazione è presentato nel Capitolo 3. Una strategia di integrazione approssimata basata su due quadrature esistente dà dei risultati ottimali, così come la strategia basata sulla costruzione di formule di quadratura opportune. Si noti che per quest'ultima strategia è richiesta la definizione di una terza griglia, chiamata griglia di intersezione, costruita durante un costoso processo chiamato processo di segmentazione.

Questi metodi ottimali hanno ispirato il trattamento di un problema d'interfaccia più complesso: il trattamento del problema di contatto senza attrito con gap iniziale. Nel Capitolo 4, allo scopo di trovare dei metodi numerici ottimali per il problema di contatto, dei metodi misti sono proposti per trattare il contatto rigido-deformabile, cioè tra un corpo elastico ed una fondazione rigida. Si discutono in particolare la formulazione del problema, la sua discretizzazione, l'impostazione delle condizioni di contatto e delle strategie di risoluzione. Infine, nel Capitolo 5, proponiamo dei metodi variazionali basati sui metodi mortar definiti in precedenza per approssimare il contatto deformabile-deformabile, cioè tra due corpi elastici. L'ottimalità di questi metodi è dimostrata tramite diversi esempi numerici.

French abstract

L'Analyse IsoGéométrique (IGA) a immédiatement été considérée comme prometteuse pour l'approximation et la résolution des équations aux dérivées partielles, car elle possède notamment des fonctions de base très régulières. IGA génère des approximations géométriques précises ou exactes, mais généralement au prix d'une décomposition du domaine de calcul en différents sous-domaines appelés patches. Nous avons donc besoin de méthodes efficaces pour coupler ces différents sous-domaines. Les méthodes mixtes de mortier sont privilégiées par rapport aux autres méthodes. En effet, elles permettent de maintenir la flexibilité des maillages des patches comme de leurs degrés d'espaces d'approximation.

Ce mémoire concerne l'étude de méthodes variationnelles de couplage et leurs applications à la mécanique du contact. Après un chapitre d'introduction, les Chapitres 2 et 3 sont dédiés à la définition et à l'étude de la méthode de mortier en IGA, tandis que les Chapitres 4 et 5 à leurs applications numériques aux problèmes de contact.

En s'appuyant sur le recul mathématique qui existe déjà avec la méthode des éléments finis, des méthodes de mortier ont été étudiées théoriquement et numériquement en utilisant IGA dans le Chapitre 2. Deux espaces de multiplicateurs stables fournissent une estimation d'erreur *a priori* optimale. Ces deux espaces sont tous deux définis sur le bord du maillage esclave mais sont de degrés différents.

Après l'obtention d'un espace de multiplicateur adapté, un challenge demeure: l'évaluation des intégrales de mortier, c'est-à-dire d'intégrer le produit de fonctions définies sur des maillages différents. Dans le chapitre 3, différentes stratégies d'intégration sont présentées. Une approchée basée sur les deux quadratures existantes conduit à des résultats optimaux, comme celle basée sur des formules de quadrature adaptées. Nous précisons que l'obtention de cette dernière stratégie nécessite la définition d'un troisième maillage, appelé maillage d'intersection, construit lors d'un processus coûteux de segmentation.

Ces méthodes optimales ont inspiré le traitement d'un problème d'interface non-linéaire: le problème de contact unilatéral sans frottement avec gap initial. Dans le Chapitre 4, dans l'objectif de trouver des méthodes numériques optimales spécifiques au contact, des méthodes mixtes sont proposées pour traiter le contact rigide-déformable, c'est-à-dire entre un corps élastique et une fondation rigide. La formulation du problème, sa discrétisation, l'imposition des contraintes de contact et les stratégies de résolution y sont discutées. Finalement, dans le Chapitre 5, nous proposons des méthodes variationnelles consistantes qui s'appuient sur les méthodes de mortier définies ci-dessus pour approcher des problèmes de contact déformable-déformable, c'est-à-dire entre deux corps élastiques. L'optimalité de ces dernières est démontrée numériquement sur différents exemples.

Acknowledgements

Patrice, the acknowledgement section could not have started differently, because I will be forever grateful toward you. Moreover being the person who offered me this amazing opportunity, you always believed in me, even when I did not, you supported me and helped me finding my way at different occasions. Today, I am confident to face my challenging future with a clear mind and you are not for anything on it.

I then thank you, Thomas and Amine. Thank you for your interest on my work as well as the sharing of your experiences.

More generally, I am thankful toward the three of you for the time you allowed me to share your expertise. I would also like to show you my gratitude to have hired Mathieu to work on that topic.

More generally, I thank the company Michelin to have funded my PhD contract. No one can imagine what it represents for me and how proud and thankful I am, especially being from the region Auvergne. I will always remember my internship there, the dynamic, the synergy, the technicality and the atmosphere that are reigning there is something amazing and unforgettable.

Then I thank you, Annalisa. I am grateful to you as you offered me this opportunity by accepting to be my PhD supervisor. At your sides, I have learnt a lot. You shared with me your technical knowledges and above all your scientific rigorous. You shaped my PhD training and immersed it in an international environment in which research is linked to industry. In particular, thanks to you, I got the opportunity to lead some collaborations with other research centers and to attend international congresses. It represents a lot to me.

These PhD years have been a rich experience from the professional as well as the personal points of view. My technical but also cultural and human knowledges have exponentially increased. In these years, I can affirm to have grown up a lot.

In the life path, we meet people that can change our life in a different measure - some change it forever. I am sure I would have forgotten some people in this acknowledgement section, that is why for the sake of completion I am thanking all the people who shared with me parts of these years. Thanks for being part of my path. In a certain way, that you maybe do not measure, you contribute to allow me to arrive here today.

A special thank mention to the following people:

- My Master's degree supervisor, David and all of my forming engineering teachers, as well as the INSA staff,
- My office mates, my colleagues and the staff from the IMATI, the COMPMECH group, the maths department of the University of Pavia and the IUSS of Pavia,
- Laura, Linus, Barbara, Gershon, Fady as well as the other IGA people in the world,
- My neighbours, the staff and the direction board of the Residence Biomedica,
- My Italian teachers,
- My medical practitioners and the medical staff of the San Matteo hospital,
- My sport mates and instructors,
- My large family,
- and my friends.

No detail is necessary as each of you is already aware of the reason of my gratitude.

I address a special message for you, my close friends, my second family, whenever and wherever we met in life, as wherever we are now and we will be, despite the distance, we care and will always care for each others. And for this, there is any doubt that if I am here today, it is thank to you.

Crazy team spirit;) For that, I would like to transmit you my eternal recognition.

To finish, I would like to thank my close family members, and thus in my mother tongue. Je vous serai à jamais reconnaissante, reconnaissante de m'avoir éveillée au monde ainsi que de m'avoir permis de parcourir tout ce chemin. Même si nos points de vue diffèrent parfois, au final votre soutien n'a jamais fait défaut. Merci à vous qui m'avez inculpé des valeurs comme le respect, la loyauté, la persévérance et la détermination.

Affectionately

Merci

Ericka

May the force be with you. Always and forever ;)

Contents

For my ancestors,
my beloved ones,
our descendants,

Preface

Isogeometric analysis, introduced in [60], is a Galerkin method which approximates the solution of Partial Differential Equations (PDEs) with Non Uniform Rational B-Spline (NURBS) spaces. The idea of IGA arose from the desire to mind the gap between Computer Aided Geometrical Design (CAGD) and PDE solvers, especially to bypass a cost-full step inherent to other numerical methods, namely, the mesh process. The physical domain (i.e., the computational domain) is given by NURBS parametrizations, and the solution relative to the considered problem is approximated by NURBS spaces built on these geometries (more precisely on their meshes). We refer to [31] for a complete presentation of isogeometric analysis and to [5, 6] for its mathematical understanding.

Initially in [60], its pioneers considered a strong concept which is the isoparametric paradigm, i.e., the space used to generate the geometry is mapped to the physical domain and used as approximation space for the PDE solution approximation. Since, IGA has been generalised to a set of methods which use for the PDE solution approximation, spaces based on the geometry approximation, but not necessarily the same, see, e.g., [6]. Moreover furnishing a more accurate computational domain, the spline smoothness provides good approximation properties to their underlying NURBS spaces. Thanks to that, IGA has already been successfully applied in different contexts, among them we mention the vibration one, see, e.g., [32, 61], the electromagnetic one, see, e.g., [22] as well as in challenging and complete engineering applications, see, e.g., [88]. In Chapter 1 of this thesis, splines basics are recalled.

Complex geometry as well as complex material distributions can not be approximated by one NURBS parametrization. Thus with isogeometric methods, the computational domain is generally split into different parts,

named patches. Each of them is obtained as a NURBS mapping of the unit d-cube. On each of them, underlying approximation spaces are defined. Within this framework, techniques to couple the numerical solution of the considered PDE are required at the patch interfaces. To retain the flexibility of the interface meshes as well as of the space degrees, weak coupling methods are favourable in contrast to strong point-wise couplings.

Let us consider a domain $\Omega \subset \mathbb{R}^d$, $d = 2, 3$. Let us define on Ω, V a Hilbert space and V_0 its subspace with homogeneous boundary conditions. Let $a(\cdot, \cdot)$ continuous and coercive in V be the bilinear form and $f(\cdot)$ continuous in V be the linear form associated to the problem. The considered weak formulation is: find $u \in V$ such that

$$a(u, v) = f(v), \qquad \forall v \in V_0. \tag{1}$$

Under some assumptions on $a(\cdot, \cdot)$ and $f(\cdot)$, the problem stated in (1) is well-posed, see, e.g., [45]. When the domain Ω is a patch, IGA is just the Galerkin method using splines and NURBS. Let V_h be the solution discrete space, it is a push-forward of a NURBS space. Let $V_{h,0}$ be its subspace with homogeneous boundary conditions. The discrete problem of Equation (1) is: find $u_h \in V_h$ such that

$$a(u_h, v_h) = f(v_h), \qquad \forall v_h \in V_{h,0}. \tag{2}$$

If u satisfies Equation (2), the approximation u_h of the solution u is referred as consistent. Moreover it is conform if $V_h \subset V$.

In a multi-patch setting, Ω is approximated by the union of different NURBS patches, i.e., $\overline{\Omega} = \sum_k \overline{\Omega}_k$. In this context, $a(\cdot, \cdot)$ becomes the sum of the contributions of each patch, i.e., $a(\cdot, \cdot) = \sum_k a_k(u_k, v_k)$. And the same holds for the right-hand side $f(\cdot, \cdot) = \sum_k f_k(v_k)$. We choose as discrete space the product space $V_h = \prod_k V_{k,h}$ where $V_{k,h}$ stands for the discrete space on the patch k. The continuity of the discrete solution should be ensured at the interfaces in a variationnally way. With mixed methods, it is done by the use of a Lagrange multiplier. Thus the discrete problem of Equation (1) results in a saddle-point problem, that is: find $(u_h, \lambda_h) \in$

(V_h, M_h) such that

$$\begin{cases} a(u_h, v_h) + b(v_h, \lambda_h) = f(v_h), & \forall v_h \in V_{h,0}, \\ b(u_h, \phi_h) = 0, & \forall \phi_h \in M_h, \end{cases} \tag{3}$$

with M_h the discrete multiplier space and $b(\cdot, \cdot)$ the mixed bilinear form equal to $\int_\Gamma \lambda \cdot [\![u]\!] \, \mathrm{d}s$, where Γ stands for the union of all subdomain interfaces and $[\![\cdot]\!]$ for the jump of the unknown u across Γ. Equation (3) is well-posed if and only if an inf-sup condition is satisfied between primal and dual spaces on each interface and the form $a(\cdot, \cdot)$ is coercive on the kernel relative to the mixed bilinear form defined by $\{v_h \in V_h : \quad b(v_h, \lambda_h) = 0, \quad \forall \lambda_h \in M_h\}$, see, e.g., [13]. Thus given a primal approximation space, it is influencing the multiplier space choice.

The aim of this thesis is to address and analyse some aspects related to weak coupling methods that are of a high interest in the IGA multi-patch context. In particular, we focus our attention on the following topics:

1. isogeometric mortar methods. We lead a theoretical and numerical study to propose optimal isogeometric mortar methods to ensure weakly the continuity of the PDE solution at the patch interfaces. Furthermore, we study numerically the impact of some approximations that can be done on the classical mortar formulation to improve its efficiency.

2. isogeometric contact methods. We lead a numerical study to propose optimal mixed contact methods to enforce frictionless unilateral contact conditions with initial gap. We propose numerical methods for both, rigid-deformable and deformable-deformable contact cases. I.e, we consider the contact between an elastic body and a ground and the contact between two elastic bodies. The convergence properties of the proposed methods are analysed on different benchmarks.

The results of this thesis have been partially published or are about to be published, see [17, 18]. This research work was funded by the company Michelin. It was realised in collaboration with the company Michelin and the IMATI of Pavia. Both are gratefully acknowledged.

In the following, we describe the thesis content of each of these two topics.

Isogeometric mortar methods

It is interesting to consider mortar methods, which offer a flexible approach to domain decomposition to ensure the weak continuity at the interfaces. They were originally applied in spectral and finite element methods. Mortar methods have been successfully investigated in the finite element context for over two decades, [12, 11, 10, 8, 71], for a mathematical overview, see [111]. Further applications of the mortar methods include contact problems, [9, 69, 115, 112, 114], and interface problems, e.g., in multi-physics applications, [107].

In the IGA context, the coupling of multi-patch geometries has already been investigated in several articles, [68, 90, 99, 72, 3, 29, 119, 65, 116, 20, 64], and successful applications of the mortar method are shown in [53, 43, 4]. Additionally the use of mortar-like methods in contact simulations was considered, see, e.g., [37, 39, 104, 67, 42, 102].

In this thesis, in Chapter 2, the application of mortar methods in the framework of IGA is presented theoretically as well as numerically. As it is known, its optimality requires the fulfilment of an inf-sup condition between the primal and dual spaces and suitable approximation properties for the dual space. For the Lagrange multiplier two choices of uniformly stable spaces are given, both of them being spline spaces but of a different degree. In one case, we consider an equal order pairing for which a cross point modification is required to ensure a dual space not bigger than the primal one. In the other case, the degree of the dual space is reduced by two compared to the primal one. This pairing is proven to be inf-sup stable without any necessary cross point modification. Several numerical examples confirm the theoretical results and illustrate additional aspects.

After this mathematical analysis enlightening the use of various dual spaces, in Chapter 3, we investigate numerically the impact on the solution accuracy of a few consistency errors that may be introduced to make the method easier to implement. First, we examine the use of approximate L^2-projections instead of exact L^2-projection. It means in formulation (3) we replace $b(\cdot,\cdot)$ by one of its approximation $b_h(\cdot,\cdot)$. The approximation we

analyse is mainly motivated by the application in contact mechanics, where replacing the L^2-projection with a local one helps in limiting the matrices fill-in.

Second, we analyse the consistency error that appears when taking into account the quadrature error in the computation of the terms $b(v, \lambda)$ and $b(u, \phi)$ in (3), that we referred as mortar integrals. Note that the evaluation of these bilinear forms is numerically challenging as it involves the evaluation of integrals which contain products of functions defined on different meshes. Obviously, an exact evaluation of the mortar integrals can be achieved using a quadrature rule defined on a merged mesh, i.e., a mesh which respects the lines of reduced smoothness of master and slave functions. The construction of this auxiliary mesh is challenging, especially in the three-dimensional case, since the possible shape of the elements are many and difficult to determine, see, e.g., [86, 95, 96, 53, 42]. Due to this computational complexity, it would be very appealing to use a existing quadrature rule, i.e., one based on one of the two available meshes. However, early results in [23, 81] have already shown for the finite element case that it does not yield optimal methods, especially in the case the master quadrature rule is chosen. Since splines have a higher global smoothness than finite element functions, one might expect different results in the isogeometric analysis context. Motivated by finite element observations, we firstly consider on the interface a quadrature rule purely based on the slave mesh, referred as a slave integration approach. Secondly, we consider a method using on the interface quadrature rules based on both slave and master meshes, referred as a mixed integration approach. This later one results in a non-symmetric saddle point problem. While in the first case reduced convergence rates can be observed, in the second case barely. Therefore, it provides a good integration approach which avoids the use of a merged mesh.

As the construction of the merged mesh still remains of interest to evaluate integral of functions defined on different meshes, we also present a strategy to build it in the isogeometric context in Chapter 3. Its construction is done in the slave parametric space from the triangularisation of slave parametric elements by lines relative to master element counterparts. The

use of a unique normal to associate master to slave points, and thus to obtain these former master counterparts, as well as to associate slave to master points is a key aspect of the method. This normal is chosen as the master normal. It is ensuring a well-definition of the segmentation process under reasonable tessellation parameter and master mesh finesse assumptions.

Isogeometric unilateral contact methods

Even though a huge amount of work had already been done on contact, it is still a actively ongoing research topic. We refer to [66, 73, 115, 112, 38] for a general literature in a finite element and isogeometric analysis contexts. The use of isogeometric analysis in contact has added great advantages since it allows for smooth definition of the discrete contact area. It helps the evaluation of distances and the detection of contact, that are often delicate steps within a contact algorithm. The contact conditions may be included in the problem formulation with various approaches that we try to list as follows:

- via a penalty formulation, see, e.g., [74]. Even though its simple implementation, this formulation suffers from a consistency lack that prevents the solution to fulfill completely the contact conditions. Furthermore, its efficiency relies on the penalty coefficient definition. Indeed, it should be defined as a compromise between a not so bad matrix system conditioning number and reasonable constraint enforcement.

- via a Lagrange multiplier formulation, see, e.g., [55, 30, 56]. The additional unknown on which the contact constraints have been transferred allows to reach a solution that fulfills weakly the contact conditions. Although the new constraint system requires an iterative resolution strategy which is not always ensured to converge.

- via an augmented Lagrangian multiplier formulation, see, e.g., [1, 93, 97]. It benefits from both, penalty and Lagrange multiplier formulation advantages. The additional unknown coupled with an augmented term leads to a new unconstraint system. Its solution fulfills weakly the contact conditions without damaging the matrix system conditioning. One needs to evaluate additional matrix terms and tunes an augmentation parameter.

- finally, more recently, via a Nitsche's formulation, see, e.g., [26, 27, 46, 25]. It has the advantage of the Lagrange multiplier formulation, in the sense the solution fulfills the contact conditions, but this time with no necessary additional unknown. Although, the additional terms which restore the consistency involve high order derivative terms that have to be evaluated.

The choice of the formulation together with the strategy to impose and check the contact constraints are the ingredients for a resolution method. We highlight that the method robustness relies on a perfect accordance in the way the constraints are imposed and checked. In the following, we briefly recall the main strategies that can be used to impose weakly the contact conditions. They can be separated into two types, first the Gauss point to surface methods (initially called knots to surface in IGA) see, e.g., [48, 78, 105, 37, 41] for which the constraint imposition is done at the quadrature points, secondly the surface to surface methods for which it is done on the surface, see, e.g., [86, 95, 67, 39, 94, 42, 102, 54]. The formulation choice also gives direction to possible resolution strategies. As a numerical contact method can become easily expensive, some works focused on the computational cost improvement, see, e.g., [113, 19, 40, 82, 83].

Our work sits in the field of variationally consistent techniques for frictionless contact. Concerns with the use of mortar algorithms, we developed ingredients for the design of contact algorithms. This work is original in the sense, to our knowledge, it is the first to consider isogeometric mixed methods with different degree pairings. It is of a high interest in regards to the low regularity of the contact problem solution. Indeed, it allows to maintain good approximation properties on the displacement variable while saving some computational cost using a lower degree for the multiplier. The content of the second topic of the thesis is described in the following.

In Chapter 4, we present rigid-deformable contact methods. Different aspects are investigated in a context not yet affected by any integration issue. An augmented Lagrangian formulation is considered, it allows to analyse from a numerical perspective penalty and Lagrange multiplier

formulation counterparts. The use of a lumped L^2-projection as well as discrete active contact region definition choices are discussed. Numerical results illustrate the study.

In Chapter 5, we propose and analyse algorithms for deformable-deformable contact problems. The methods we propose are variationally consistent and based on the mortar methods defined in Chapters 2 and 3 and thus referred as mortar-like methods. We design an active set strategy which activates and inactivates functions depending on the sign of control variables of the multiplier and of a given projection of the gap. Such a projection is chosen as an approximate L^2-projection into the multiplier space (with lumped mass). Moreover, with the results of Chapter 3, we depict the method in such a way that no merged mesh is needed to evaluate the integrals and the accuracy is preserved. To our knowledge, it is the first work to present optimal contact methods without any segmentation process, and thus by using existing quadrature rules to evaluate the contact integrals. Numerical results show qualitative results, discuss the optimality of the proposed methods and show result comparisons with one of the most common integration method currently used in the deformable-deformable contact context, see, e.g., [48, 108, 37].

Chapter 1

Basics on splines, multi-patch gluing and contact

Contents

This chapter aims to introduce the different topics of this thesis. Herein, we recall some concepts and set notations used throughout all the thesis.

We start by spline basics, then we focus on the domain decomposition context on which we set mortar method basics. And finally, we introduce the setting of the considered unilateral frictionless contact problem with initial gap.

In the following, we use the classical bold notation for vector variables as well as the double underline one for tensor variables.

1.1 Spline basics

Hereafter, we give the basics of the spline theory used in IGA. For more details, we refer to the classical literature [36, 92, 98, 100].

1.1.1 Univariate functions

Univariate B-Spline Let us denote by p the degree of the univariate B-Splines and by Ξ a univariate knot vector, i.e., a ordered sequence of points called knots. Let us consider

$$\Xi = \{0 = \xi_1 = \ldots = \xi_{p+1} < \xi_{p+2} \leq \ldots \leq \xi_n < \xi_{n+1} = \ldots = \xi_{n+p+1} = 1\}$$

where the first and last entries are repeated $(p+1)$-times. This kind of knot vector is the most common one used and is called an open knot vector. Note that without loss of generality, the parametric segment is chosen herein as $\mathcal{I} = (0,\, 1)$, i.e., $\xi_1 = 0$ and $\xi_{n+p+1} = 1$.

Let us define $U = \{\zeta_1,\, \zeta_2,\, \ldots,\, \zeta_E\}$ the knot vector without any repetition, also called breakpoint vector. For each breakpoint ζ_j of U, we define its multiplicity m_j as its number of repetitions in Ξ then

$$\Xi = \{\underbrace{\zeta_1,\, \ldots,\, \zeta_1}_{m_1 \text{ times}},\, \underbrace{\zeta_2,\, \ldots,\, \zeta_2}_{m_2 \text{ times}},\, \ldots,\, \underbrace{\zeta_E,\, \ldots,\, \zeta_E}_{m_E \text{ times}}\}.$$

The points in U form a partition of the parametric interval $\mathcal{I}$, i.e., a mesh.

The univariate $(p+1)$-order B-Spline is defined recursively by the Cox, De Boor, Mansfield formula [92, 31] based on the univariate knot vector Ξ. It defines n univariate B-Spline functions $\widehat{B}_i^p(\zeta)\,(i = 1, \ldots, n)$ starting from the univariate B-Spline functions of degree 0 defined by:

$$\widehat{B}_i^0(\zeta) = \begin{cases} 1 & \text{if } \xi_\text{i} \leq \zeta < \xi_\text{i+1} \\ 0 & \text{otherwise} \end{cases}$$

to the univariate B-Spline functions of degree q, for $1 \leq q \leq p$, defined by:

$$\widehat{B}_i^q(\zeta) = \frac{\zeta - \xi_i}{\xi_{i+q} - \xi_i}\, \widehat{B}_i^{q-1}(\zeta) + \frac{\xi_{i+q+1} - \zeta}{\xi_{i+q+1} - \xi_{i+1}}\, \widehat{B}_{i+1}^{q-1}(\zeta).$$

Where at its occurrence it is formally assumed that $\frac{0}{0} = 0$.

It holds the following relation between the total multiplicity, the degree of the basis and its number of functions:

$$\sum_{j=1}^{E} m_j = n + p + 1.$$

Let us define $S^p(\Xi)$ the univariate spline space of degree p defined on the knot vector Ξ spanned by the corresponding B-Spline functions, i.e.,

$$S^p(\Xi) = \text{span}\{\widehat{B}_i^p, i = 1, \ldots, n\}.$$

We recall hereafter some important properties of the univariate B-Splines which can be observed on an example of a quadratic B-Spline in Figure 1.1. Each $\widehat{B}_i^p$ is a piecewise positive polynomial of degree p and has a local support. $\widehat{B}_i^p$ is non-zero only on at most $(p+1)$ elements and $\text{supp}\, \widehat{B}_i^p = [\xi_i, \xi_{i+p+1}]$. Consequently on an element $[\zeta_i, \zeta_{i+1}]$, at most $(p+1)$ basis functions have non-zero values.

The inter-element continuity is defined by the breakpoint multiplicity. More precisely, the basis functions are C^{p-m_j} at each $\zeta_j \in Z$.

The B-Spline forms a partition of unity.

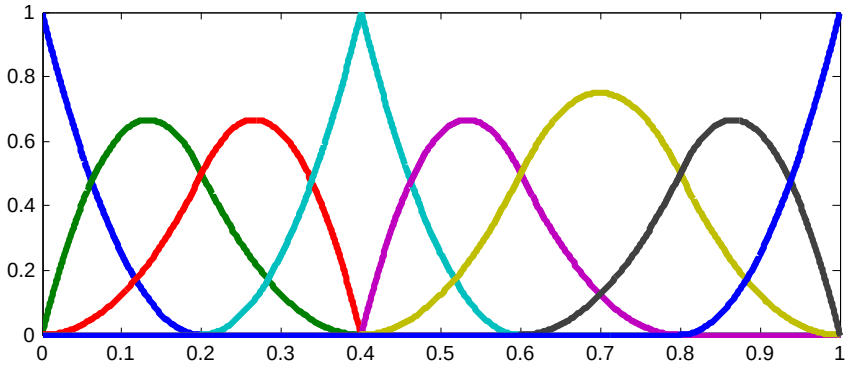

Figure 1.1: A univariate quadratic B-Spline built on the open knot vector $\Xi = \{0, 0, 0, \frac{1}{5}, \frac{2}{5}, \frac{2}{5}, \frac{3}{5}, \frac{4}{5}, 1, 1, 1\}$. We note the C^0 continuity in $\zeta_j = \frac{2}{5}$.

Assuming that the multiplicities of the internal knots are such that the B-Spline is at least C^1 on $(0, 1)$, the derivative of each function in the basis can be represented, see [6, 100]. The derivatives belong to the spline space

$S^{p-1}(\Xi')$, where $\Xi' = \{\xi_2, \xi_3, \ldots, \xi_{E-1}\}$ is an open knot vector with first and last knots repeated p-times.

Moreover, the application derivation $\frac{d}{d\zeta} : S^p(\Xi) \to S^{p-1}(\Xi')$ is a linear surjective application, i.e., $d_\zeta S^p(\Xi) = S^{p-1}(\Xi')$([100] Theorem 4.49). The derivatives are expressed by

$$\frac{d\widehat{B}_i^p}{d\zeta}(\zeta) = \frac{p}{\xi_{i+p} - \xi_i}\,\widehat{B}_i^{p-1}(\zeta) - \frac{p}{\xi_{i+p+1} - \xi_{i+1}}\,\widehat{B}_{i+1}^{p-1}(\zeta) \quad \forall \zeta \in (0,1),$$

where it is formally assumed that $\widehat{B}_1^{p-1}(\zeta) = \widehat{B}_{n+1}^{p-1}(\zeta) = 0$.

Univariate NURBS Let us introduce $\widehat{DW}(\zeta)$ the weight function as

$$\widehat{DW}(\zeta) = \sum_{i=1}^{n} \omega_i\,\widehat{B}_i^p(\zeta),$$

with w_i some positive coefficients usually called weights.

The NURBS functions of degree p relative to the univariate knot vector Ξ are defined as a function of the weights and B-Spline functions by

$$\widehat{N}_i^p(\zeta) = \frac{\omega_i\ \widehat{B}_i^p(\zeta)}{\widehat{DW}(\zeta)} \quad i = 1, \ldots, n.$$

As rational B-Spline functions, they have similar properties to them. Note that B-Spline functions can indeed be regarded as NURBS functions with all the weights taken equal to 1, which implies $\widehat{DW}(\zeta) = 1$.

Let us define $N^p(\Xi)$ the univariate NURBS space of degree p defined on the knot vector Ξ spanned by the NURBS functions, i.e.,

$$N^p(\Xi) = \mathrm{span}\{\widehat{N}_i^p(\zeta), i = 1, \ldots, n\}.$$

1.1.2 Multivariate B-Splines and NURBS

Multivariate B-Spline These functions are defined as a tensor product of univariate B-Spline ones.

Let d be the space dimensions. For any direction δ ($\delta = 1, \ldots, d$), we introduce p_δ the degree of the relative univariate B-Spline, n_δ the number of the relative univariate B-Spline functions, Ξ_δ the relative univariate open knot vector and U_δ the relative univariate breakpoint vector.

We then define by $\boldsymbol{\Xi} = (\Xi_1 \times \Xi_2 \times \ldots \times \Xi_d)$ the multivariate knot vector and by $\mathbf{U} = (U_1 \times U_2 \times \ldots \times U_d)$ the multivariate breakpoint vector. For simplicity of notation, we are not defining the degree vector but instead we assume in the following that the degree is the same in all parametric directions and denote it by p.

$\mathbf{U}$ forms a partition $\widehat{\mathcal{M}}$ of the parametric domain denoted $\widehat{\Omega} = (0,1)^d = \otimes_{\delta=1}^{d} \mathcal{I}_\delta$. The partition is called cartesian grid or parametric Bézier mesh, and is defined as

$$\widehat{\mathcal{M}} = \{\mathbf{Q_j} = \widehat{\tau}_{1,j_1} \times \ldots \times \widehat{\tau}_{d,j_d},\ \widehat{\tau}_{\delta,j_\delta} = [\zeta_{\delta,j_\delta}, \zeta_{\delta,j_\delta+1}],\ \mathbf{j} = (j_1, \ldots, j_d),$$

$$1 \leq j_\delta \leq E_\delta - 1\}.$$

The mesh size of each underlying univariate partition U_δ $(\delta = 1, \ldots, d)$ is denoted by $\widehat{h}_{\delta,j}$ $(j = 1, \ldots, E_\delta - 1)$. We do the following assumption regarding the mesh uniformity.

Assumption 1 (Quasi-uniform parametric mesh)**.** *The partition defined by the breakpoints is globally quasi-uniform, i.e., there exists a constant θ such that the univariate element size ratio is uniformly bounded: $\widehat{h}_{\delta,i}/\widehat{h}_{\delta',j} \leq \theta$, with $\delta, \delta' = 1, \ldots, d$ and $i = 1, \ldots, E_\delta - 1$, $j = 1, \ldots, E_{\delta'} - 1$.*

Note that Assumption 1 excludes the case of anisotropic meshes which are used, e.g., for boundary layers and of graded meshes which are used in case of singularities. This assumption is made here only to reduce the technicality of the following proofs.

We introduce a set of multi-indices $\mathbf{I} = \{\mathbf{i} = (i_1, \ldots, i_d) : 1 \leq i_\delta \leq n_\delta\}$ to numerate the basis functions. Multivariate B-Spline functions are defined for each multi-index $\mathbf{i}$ by tensorization of the univariate B-Spline ones as

$$\widehat{B}^p_{\mathbf{i}}(\boldsymbol{\zeta}) = \widehat{B}^p_{i_1}(\zeta_1) \ldots \widehat{B}^p_{i_d}(\zeta_d), \quad \mathbf{i} \in \mathbf{I}.$$

The multivariate spline space in the parametric domain is then defined by

$$S^p(\boldsymbol{\Xi}) = \otimes_{\delta=1}^{d} S^p(\Xi_\delta) = \operatorname{span}\{\widehat{B}^p_{\mathbf{i}}(\boldsymbol{\zeta}), \mathbf{i} \in \mathbf{I}\}.$$

Multivariate NURBS They are rational functions of multivariate B-Spline functions. A weight $\omega_{\mathbf{i}}$ $(\mathbf{i} \in \mathbf{I})$ should be given for each of one of these

functions. Thus, in general multivariate NURBS functions are not obtained and indeed can not be obtained as a tensor product of univariate NURBS functions due to the need of the weights $\omega_{\mathbf{i}}$ in their definition.

We set $N^p(\boldsymbol{\Xi})$ as the multivariate NURBS space spanned by the multivariate NURBS functions $\widehat{N}^p_{\mathbf{i}}(\boldsymbol{\zeta})$.

1.1.3 Parametrization

NURBS have widely been used in the CAGD since they are capable to describe various geometries very accurately. For a set of points $\mathbf{C}_{\mathbf{i}} \in \mathbb{R}^d$, $\mathbf{i} \in \mathbf{I}$, called control points, we define $\mathbf{F}(\boldsymbol{\zeta})$ a parametrization of a NURBS curve ($d = 1$), surface ($d = 2$) or solid ($d = 3$) as a linear combination of NURBS functions and control points

$$\mathbf{F}(\boldsymbol{\zeta}) = \sum_{\mathbf{i}\in\mathbf{I}} \mathbf{C}_{\mathbf{i}}\, \widehat{N}^p_{\mathbf{i}}(\boldsymbol{\zeta}).$$

A NURBS patch also called NURBS geometry is the image of the parametric domain $\widehat{\Omega}$ by the parametrization $\mathbf{F}$, i.e.,

$$\mathbf{F} : \widehat{\Omega} \to \Omega, \quad \Omega = \mathbf{F}(\widehat{\Omega}), \quad \mathbf{F} \in N^p(\boldsymbol{\Xi}).$$

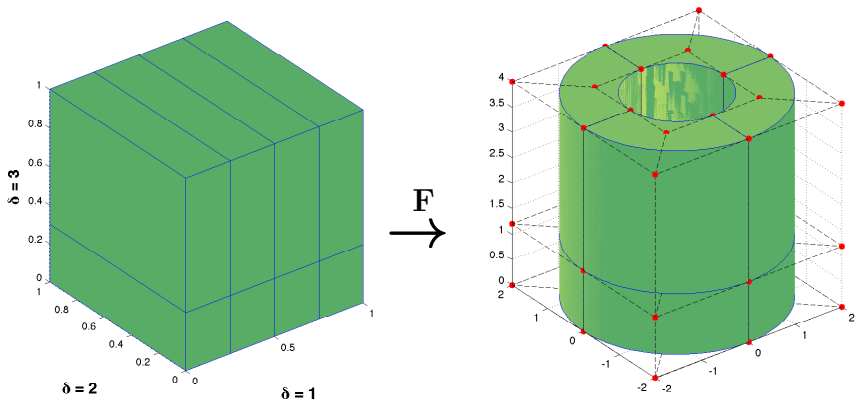

Figure 1.2: Left: A parametric mesh. Right: Its geometrical mapping. We note that the red points are the control points.

We note that $\mathbf{F}$ is also called the geometrical mapping. In Figure 1.2, an example of mapping is given. It is visible that the control points do not necessarily belong to the NURBS geometry, indeed they are located at a distance of order $\mathcal{O}(h^2)$ to the geometry, see, e.g., [28, 35]. The geometry has the continuity of the basis which defined it and the control points belong to

it only at the low continuity locations, i.e, at the C^0 and even lower order continuity locations.

The linear geometrical interpolation of the control points defines the control lattice. The NURBS geometry is contained inside the convex hull of the control lattice. Moreover, any affine transformation of the NURBS geometry can be obtained transforming the control points accordingly.

We define a physical mesh $\mathcal{M}$ as the image of the parametric mesh $\widehat{\mathcal{M}}$ through $\mathbf{F}$, and denote by $\mathbf{O}$ its elements, i.e.,

$$\mathcal{M} = \{\mathbf{O} \subset \Omega : \mathbf{O} = \mathbf{F}(\mathbf{Q}),\ \mathbf{Q} \in \widehat{\mathcal{M}}\}.$$

We emphasise that according to this definition, the control points do not enter in the mesh definition, and thus the control lattice should not be mistaken with the mesh. It is important to highlight that aspect which is a common mistake done by people from the finite element community. Let us set the ideas on an example. In Figure 1.3, we consider two patches with a common interface. On the first line, the two interface meshes are identical while the interface control lattices are not as the geometries are approximated by spline spaces of different degrees. On the second line, both, interface meshes and interface control lattices differ, as the geometries are approximated by spline spaces defined on different knot vectors.

Let us assume the following regularity of $\mathbf{F}$.

Assumption 2 (Regularity of the mapping $\mathbf{F}$)**.** *The parametrization $\mathbf{F}$ is a bi-Lipschitz homeomorphism. Moreover, $\mathbf{F}_{|\overline{\mathbf{Q}}}$ is in $C^\infty(\overline{\mathbf{Q}})$ for all elements of the parametric mesh, and $\mathbf{F}^{-1}_{|\overline{\mathbf{O}}}$ is in $C^\infty(\overline{\mathbf{O}})$ for all elements of the physical mesh.*

Let us define the mesh size for any parametric element as $h_{\mathbf{Q_j}} = \mathrm{diam}(\mathbf{Q_j})$ and analogously for any physical element as $h_{\mathbf{O_j}}$. We note that Assumption 2 ensures that $h_{\mathbf{Q_j}} \approx h_{\mathbf{O_j}}$. Thus, no distinction is required between parametric and physical mesh sizes and we use in the following the simple notation $h_{\mathbf{j}}$ for the mesh size. We denote the maximal one by $h = \max_{\mathbf{j}} h_{\mathbf{j}}$.

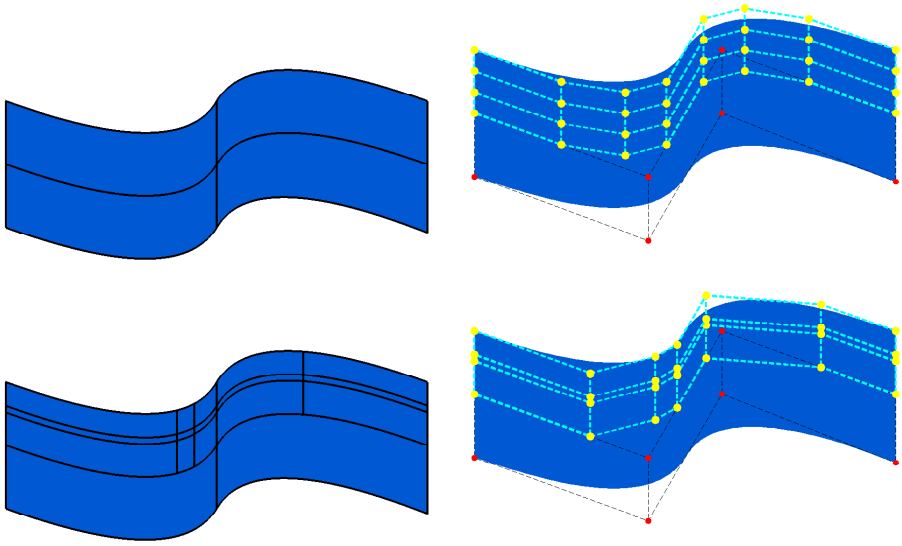

Figure 1.3: Mesh (left) versus control lattice (right) definition. Top: Geometry approximation spaces of different degrees. Bottom: Geometry approximation spaces defined on different knot vectors. The red and yellow points are the control points.

1.1.4 Spaces and refinement procedures

Let v the variable we aim to approximate numerically. It is the solution of a PDE we are going to approximate on NURBS spaces. We introduce V_h the approximation space on Ω defined by

$$V_h = \{v = \widehat{v} \circ \mathbf{F}^{-1}, \quad \widehat{v} \in N^p(\boldsymbol{\Xi})\}.$$

It is defined on the knot vector $\boldsymbol{\Xi}$ and it is of degree p. This space is a push-forward of a NURBS space. It is known to have optimal approximation properties as stated in the following lemma, see, e.g., [5, 100, 7].

Lemma 3. *Given a quasi-uniform mesh and let r, s be such that $0 \leq r \leq s \leq p+1$. Then, there exists a constant C depending only on p, θ, $\mathbf{F}$ and $\widehat{DW}$, such that for any $v \in H^s(\Omega)$ there exists an approximation $v_h \in V_h$, such that*

$$\|v - v_h\|_{H^r(\Omega)} \leq Ch^{s-r}\|v\|_{H^s(\Omega)}.$$

Spline and NURBS spaces have three different refinement strategies: h, p and k-refinement ones which can affect the mesh element number, the basis function number and the basis degree. We refer to [92, 31] for some

algorithmic details on the refinement procedures and [33] for a study on them.

The h-refinement procedure consists in an insertion of further knots in univariate knot vector(s) defining Ξ. It results either in an increase of the mesh element number or a local reduction of the space continuity. In Figure 1.3, to set clearly the idea, we show it influences on some geometry approximation spaces. E.g., the second line of Figure 1.3 has been obtained by a non-uniform h-refinement procedure of the top subdomain of the geometry visible in Figure 1.4.

The p-refinement procedure consists in an increase of the degree, it results in an increase of the space continuity at the relative mesh lines. E.g., the first line of Figure 1.3 has been obtained by a p-refinement procedure of the top subdomain of the geometry visible in Figure 1.4.

And the k-refinement procedure, specificity of the spline, is a p-refinement procedure followed by a h-refinement one. It allows to maintain a certain continuity in the approximation space while refining.

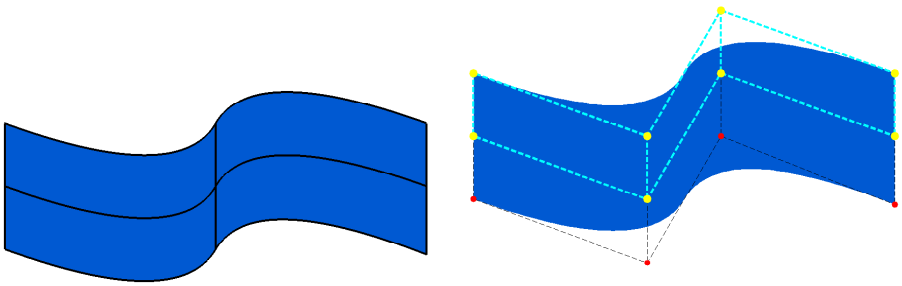

Figure 1.4: Mesh (left) versus control lattice (right) of a geometry split into two subdomains, each of them being approximated with the coarsest possible approximation space. The red and yellow points are the control points.

We precise that the refinement procedure is done starting from an initial mesh denoted $\mathcal{M}_0$ for which we require quasi-uniformity, i.e., Assumption 1.

The refinement procedures are such that once a geometry has been approximated by a NURBS parametrization, i.e., defined on an initial knot vector, an initial degree, an initial set of control points and weights, any refinement procedures applied to the NURBS space is not modifying the geometry approximation.

In the following, by refinement procedure we only refer to the h-refinement one, i.e., we keep the degree fixed while refining. Applying the refinement procedure, it yields a family of meshes $\mathcal{M}_k$, each mesh being a refinement of the initial one. Under the assumptions 1 and 2, this family of meshes is shape regular.

1.2 Isogeometric methods on multi-patch domains

Hereafter, after stating the problem setting, we define the multi-patch geometry approximation context. Then we introduce the necessary functional framework and finally we give the discrete problem relative to the mortar method context.

Let $\Omega \subset \mathbb{R}^d$, $d = 2, 3$, be a bounded domain, $\alpha, \beta \in L^\infty(\Omega)$, $\alpha > \alpha_0 > 0$ and $\beta \geq 0$. We consider the following second order elliptic boundary value problem with homogeneous Dirichlet conditions

$$-\operatorname{div}(\alpha \nabla u) + \beta u = f \quad \text{in } \Omega, \tag{1.1a}$$

$$u = 0 \quad \text{on } \partial\Omega_D = \partial\Omega. \tag{1.1b}$$

We assume α, β to be sufficiently regular, but allow jumps in special locations, which are specified later.

1.2.1 Description of the computational domain

Let a decomposition of the domain Ω into K non-overlapping subdomains Ω_k be given:

$$\overline{\Omega} = \bigcup_{k=1}^{K} \overline{\Omega}_k, \text{ and } \Omega_i \cap \Omega_j = \emptyset, i \neq j.$$

For $1 \leq k_1 < k_2 \leq K$, $k_1 \neq k_2$, we define the interface as the interior of the intersection of the boundaries, i.e., $\overline{\gamma}_{k_1 k_2} = \partial\Omega_{k_1} \cap \partial\Omega_{k_2}$, where $\gamma_{k_1 k_2}$ is open. Let the non-empty interfaces be enumerated by γ_l, $l = 1, \ldots, L$, and define the skeleton $\Gamma = \bigcup_{l=1}^{L} \gamma_l$ as the union of all interfaces. For each interface, one of the adjacent subdomains is chosen as the master side and one as the slave side.

We denote the index of the former by $M(l)$, the index of the latter one by $S(l)$, and thus $\overline{\gamma}_l = \partial\Omega_{M(l)} \cap \partial\Omega_{S(l)}$. Note that one subdomain can at

the same time be classified as a master domain for one interface and as a slave domain for another interface, see Figure 1.5. On the interface γ_l, we define the outward normal $\mathbf{n_l}$ of the master side $\partial\Omega_{M(l)}$ and denote by $\dfrac{\partial u}{\partial \mathbf{n_l}}$ the normal derivative on γ_l from the master side.

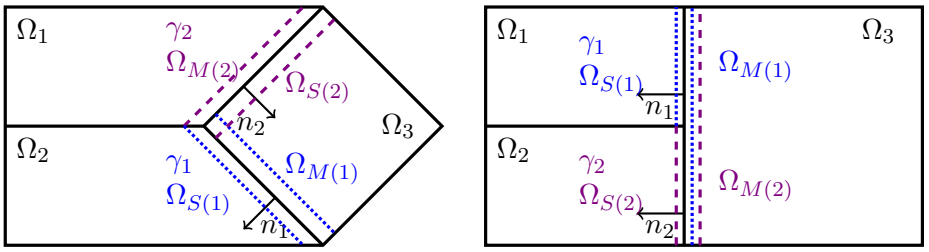

Figure 1.5: Geometrical conforming case (left) and *slave conforming* case (right).

Each subdomain Ω_k is given as the image of the parametric space $\widehat{\Omega}$ by one single NURBS parametrization $\mathbf{F}_k : \widehat{\Omega} \to \Omega_k$, see Subsection 1.1.3, which satisfies the Assumption 2. The h-refinement procedure, see Subsection 1.1.4, yields a family of meshes denoted $\mathcal{M}_{k,h}$, each mesh being a refinement of the initial one for which we require Assumption 1. Thus, the family of meshes is shape regular. We anticipate that a more detailed analysis may show the same results under milder assumptions on the meshes (as the local quasi-uniformity).

We furthermore assume that for each interface, the pull-back with respect to the slave domain is a whole face of the unit d-cube in the parametric space. Under these assumptions, we are not necessarily in a geometrically conforming situation, but we call it a *slave conforming* situation, see the right setting in Figure 1.5. If we also assume that the pull-back with respect to the master domain is a whole face of the unit d-cube, we are in a fully geometrically conforming situation, see the left picture of Figure 1.5. We note that in this latter case, for the respective interface, the master-slave choice is arbitrary.

1.2.2 Variational problem

Hereafter, we recall main functional analysis properties to introduce our abstract framework and then set the variational problem.

We use standard Lebesgue and Sobolev spaces on a bounded Lipschitz domain $D \subset \mathbb{R}^{d-1}$ or $D \subset \mathbb{R}^d$. $L^2(D)$ denotes the Lebesgue space of square integrable functions, endowed with the norm $\|f\|_{L^2(D)} = (\int_D |f|^2 \ \mathrm{d}x)^{1/2}$.

For $l \in \mathbb{N}$, $H^l(D)$ denotes the Sobolev space of functions $f \in L^2(D)$ such that their weak derivatives up to the order l are also in $L^2(D)$. For a fractional index $s > 0$, $H^s(D)$ denotes the fractional Sobolev space as defined in [51]. Let us mention that $H^{1/2}(\partial D)$ is the trace space of $H^1(D)$.

The Sobolev space of order one with vanishing trace is $H_0^1(D) = \{v \in H^1(D), tr(v) = 0\}$. Working on subsets of the boundary $\gamma \subset \partial D$, special care has to be taken about the value on the boundary of γ. We define by $H_{00}^{1/2}(\gamma) \subset H^{1/2}(\gamma)$ the space of all functions that can be trivially extended on $\partial D \setminus \gamma$ by zero to an element of $H^{1/2}(\partial D)$. The dual space of $H_{00}^{1/2}(\gamma)$ is denoted $H^{-1/2}(\gamma)$. Note that on closed surfaces, i.e., $\gamma = \partial D$, it holds $H^{1/2}(\gamma) = H_{00}^{1/2}(\gamma)$. Furthermore, in the following we omit the trace operator whenever there is no ambiguity.

For each Ω_k, we introduce the space $H_*^1(\Omega_k) = \{v_k \in H^1(\Omega_k), v_{k|_{\partial\Omega\cap\partial\Omega_k}} = 0\}$. And in order to set a global functional framework on Ω, we consider the broken Sobolev spaces $V = \prod_{k=1}^{K} H_*^1(\Omega_k)$, endowed with the broken norm $\|v\|_V^2 = \sum_{k=1}^{K} \|v\|_{H^1(\Omega_k)}^2$, and $M = \Pi_{l=1}^{L} H^{-1/2}(\gamma_l)$.

The standard weak formulation of (1.1) reads as follows: find $u \in H_0^1(\Omega)$ such that

$$\int_\Omega \alpha \nabla u \cdot \nabla v + \beta\, u\, v \,\mathrm{d}x = \int_\Omega f\, v \,\mathrm{d}x, \quad v \in H_0^1(\Omega). \tag{1.2}$$

It is well-known that under the assumptions on α and β, the variational problem (1.2) is uniquely solvable.

From now on, we assume that jumps of α and β are solely located at the skeleton, and we define the linear and bilinear forms $a\colon V \times V \to \mathbb{R}$ and $f\colon V \to \mathbb{R}$, such that

$$a(u,v) = \sum_{k=1}^{K} \int_{\Omega_k} \alpha \nabla u \cdot \nabla v + \beta\, u\, v \,\mathrm{d}x, \quad f(v) = \sum_{k=1}^{K} \int_{\Omega_k} f v \,\mathrm{d}x.$$

1.2.3 Discretization

On Ω, we define the product space $V_h = \prod_{k=1}^{K} V_{k,h} \subset V$, which forms a $H^1(\Omega)$ non-conforming space discontinuous over the interfaces, where $V_{k,h}$ is the approximation space defined on the subdomain Ω_k

The mortar method is based on a weak enforcement of continuity across the interfaces γ_l in broken Sobolev spaces. Let $M_{l,h} \subset L^2(\gamma_l)$ be a space of discrete Lagrange multipliers defined on each interface γ_l and built on the slave mesh. On the skeleton Γ, we define the discrete product Lagrange multiplier space M_h as $M_h = \prod_{l=1}^{L} M_{l,h}$. Furthermore, we define the discrete trace space with additional zero boundary conditions by $W_{l,h} = \{v_{|\gamma_l}, v \in V_{S(l),h}\} \cap H_0^1(\gamma_l)$.

One possibility for a mortar method, starting from the standard weak formulation (1.2) on which we impose weakly the interface continuity conditions and then discretise, is to specify the discrete weak formulation as a saddle point problem: find $(u_h, \lambda_h) \in V_h \times M_h$, such that

$$a(u_h, v_h) + b(v_h, \lambda_h) = f(v_h), \quad v_h \in V_h, \tag{1.3a}$$

$$b(u_h, \phi_h) = 0, \quad \phi_h \in M_h, \tag{1.3b}$$

where $b(u, \phi) = \sum_{l=1}^{L} \int_{\gamma_l} \phi[u]_l \, \mathrm{d}s$ and $[\cdot]_l$ denotes the jump from the master to the slave side over γ_l. We note that the Lagrange multiplier λ_h gives an approximation of the normal flux across the skeleton.

To completely define the mortar method, it remains to explicit the multiplier space. We point out that it has to be done carefully, see, e.g., [8, 13]. Choices of different spaces are discussed in Chapter 2.

1.3 Formulations for contact problems

Hereafter, after stating the unilateral frictionless contact problem with initial gap, we define its weak formulations as well as their discretizations.

1.3.1 Description of the problem

In a contact problem, different elastic bodies may interact. We immediately restrict our attention to two specific cases, the first one named rigid-deformable which is the contact between a rigid body and an elastic one, the second one named deformable-deformable one which is the contact between two elastic bodies. We note that the general case of self-contact problems is excluded. Moreover, we do the following linear assumptions, i.e., the small displacement-deformation and the plane linear isotropic

elastic material assumptions. The classical slave-master distinction is used. I.e., one body is referred as the master one and denoted in the following by the index M. We note that for the rigid-deformable case, the rigid subdomain is always set as the master. The other subdomain is referred as the slave one and denoted by the index S.

In presence of potential contact, the boundary of each discretised subdomain Ω_k is split into three non overlapping parts $\Gamma_{D,k}$, $\Gamma_{N,k}$ and $\Gamma_{C,k}$. The boundary conditions being either a pressure $\boldsymbol{l}_k$ on $\Gamma_{N,k}$ the part of $\partial\Omega_k$ referred as its Neumann boundary, or a prescribed displacement $\boldsymbol{u_{D,k}}$ on $\Gamma_{D,k}$ the part of $\partial\Omega_k$ referred as its Dirichlet boundary, or contact conditions on $\Gamma_{C,k}$ the part of $\partial\Omega_k$ referred as its potential area of contact. $\Gamma_{N,k}$, $\Gamma_{D,k}$ and $\Gamma_{C,k}$ satisfy the following relations which ensure the problem to be well posed: $\partial\Omega_k = (\Gamma_{N,k} \cup \Gamma_{D,k} \cup \Gamma_{C,k})$, $(\Gamma_{N,k} \cap \Gamma_{D,k} \cap \Gamma_{C,k}) = \emptyset$ and $\text{meas}(\Gamma_{D,k}) \neq \emptyset$.

In order to set the frictionless unilateral contact conditions with initial gap it is necessary to introduce some preliminary contact variables, i.e., the gap g_N and the contact pressure σ_N for both contact cases.

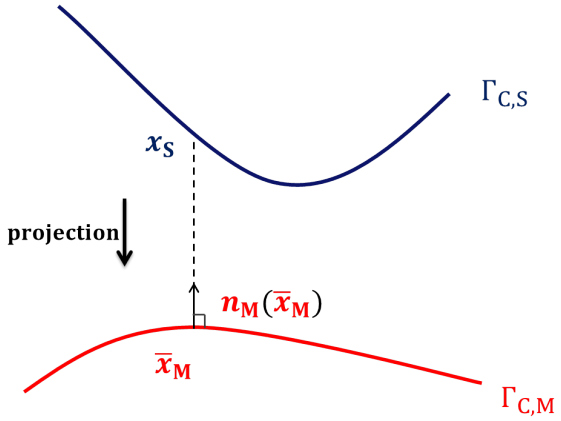

Figure 1.6: Projection of a slave point on the master.

Given a $\boldsymbol{x_S} \in \Gamma_{C,S}$, we define its projected point(s) $\bar{\boldsymbol{x}}_{\boldsymbol{M}} \in \Gamma_{C,M}$ as the solution of:

$$\min_{\boldsymbol{x_M} \in \Gamma_{C,M}} d(\boldsymbol{x_S}, \boldsymbol{x_M}),$$

i.e., the closest point(s) on the master to the current slave point, see some examples in Figures 1.6, 1.7 and 1.8 and the Appendix. We point out that the existence as well as the uniqueness of the solution of this minimisation problem are not warranted and this may have an impact on the optimality

of the proposed contact methods. Although, in the isogeometric analysis context, thanks to the high smoothness of splines, they may be better ensured than in the finite element context. We note that some assumptions on the geometry approximations can alleviate these aspects.

Rigid-deformable contact Figure 1.7. In this case, the master domain is described by a parametric equation, i.e., it is not discretised.

The contact variables g_N and σ_N are respectively defined as a function of the initial configuration of the two domains $\boldsymbol{X_S}$ and $\boldsymbol{X_M}$, the slave displacement $\boldsymbol{u_S}$, the slave stress and the contact normal chosen as the master normal and thus denoted $\boldsymbol{n_M}$, by

$$g_N = \boldsymbol{u_S} \cdot \boldsymbol{n_M} + (\boldsymbol{X_S} - \overline{\boldsymbol{X}}_{\boldsymbol{M}}) \cdot \boldsymbol{n_M} = \boldsymbol{u_S} \cdot \boldsymbol{n_M} + g,$$

$$\sigma_N = (\underline{\underline{\sigma_S}} \cdot \boldsymbol{n_S}) \cdot \boldsymbol{n_S} = -(\underline{\underline{\sigma_S}} \cdot \boldsymbol{n_S}) \cdot \boldsymbol{n_M}.$$

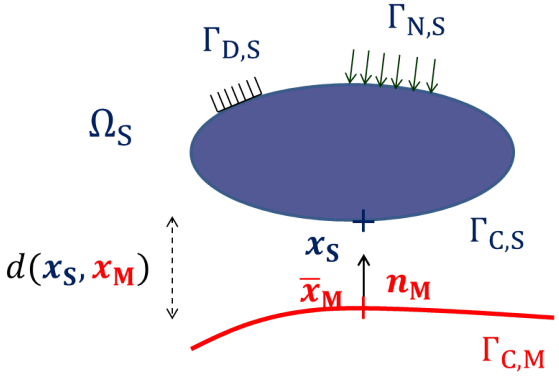

Figure 1.7: Contact problem setting in the rigid-deformable case.

We highlight that even though the small displacement-deformation assumption is done, to define the contact variables and then the active contact region, one needs to distinguish between the initial and current configurations of the slave domain. Here, the unilateral contact conditions are obviously verified on $\Gamma_{C,S}$.

We point out that in the finite element context choosing the contact normal as the master normal, i.e., the normal of a parametric equation is a way to ensure smooth properties on the contact normal. While in the isogeometric analysis context they can also be ensured by choosing the slave normal as the contact normal thanks to the smoothness of splines, functions

on which the geometry approximations are based on. This arbitrary choice is done, we note that it will be commented in further details later on.

Deformable-deformable contact Figure 1.8. In this case, the contact variables g_N and σ_N are respectively defined as a function of either the current configuration of the two subdomains $\boldsymbol{x_S}$ and $\boldsymbol{x_M}$ or the initial configuration of the two subdomains $\boldsymbol{X_S}$ and $\boldsymbol{X_M}$, their displacements $\boldsymbol{u_S}$ and $\boldsymbol{u_M}$, either the master or slave stress and the contact normal still chosen as the master normal, by

$$g_N = (\boldsymbol{x_S} - \overline{\boldsymbol{x}}_{\boldsymbol{M}}) \cdot \boldsymbol{n_M} = (\boldsymbol{u_S} - \overline{\boldsymbol{u}}_{\boldsymbol{M}}) \cdot \boldsymbol{n_M} + (\boldsymbol{X_S} - \overline{\boldsymbol{X}}_{\boldsymbol{M}}) \cdot \boldsymbol{n_M},$$

$$= (\boldsymbol{u_S} - \overline{\boldsymbol{u}}_{\boldsymbol{M}}) \cdot \boldsymbol{n_M} + g,$$

$$\sigma_N = (\underline{\underline{\sigma_M}} \cdot \boldsymbol{n_M}) \cdot \boldsymbol{n_M} = (\underline{\underline{\sigma_S}} \cdot \boldsymbol{n_S}) \cdot \boldsymbol{n_S} = -(\underline{\underline{\sigma_S}} \cdot \boldsymbol{n_S}) \cdot \boldsymbol{n_M}.$$

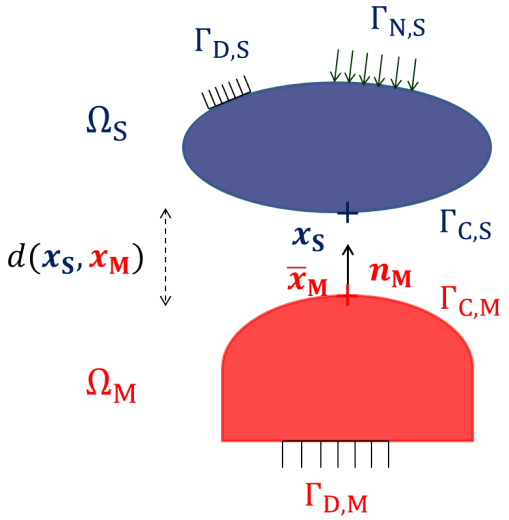

Figure 1.8: Contact problem setting in the deformable-deformable case.

We still highlight that even though the small displacement-deformation assumption is done, to define the contact variables and then the active contact region, one needs to distinguish between the initial and current configurations of the two subdomains. Here, we consider that the contact can occur between $\Gamma_{C,S}$ and $\Gamma_{C,M}$. The unilateral contact conditions are verified on $\Gamma_{C,S}$. Due to the small displacement-deformation assumption, in the neighbourhood of the active contact region it is implicitly assumed that $\Gamma_{C,S}$ and $\Gamma_{C,M}$ differ only a little as any configuration update is done in

the resolution process. In a more general case, both subdomain geometries are updated while getting the solution. Thus even though the unilateral contact conditions are verified on $\Gamma_{C,S}$, as the two different $\Gamma_{C,k}$ (with $k = \{S,\ M\}$) tend to match in the active contact region due to the geometry updates, the contact conditions will be satisfied on both $\Gamma_{C,k},\ k = \{S,\ M\}$.

With the notations introduced above, the contact conditions referred as unilateral contact conditions or Karush-Kuhn-Tucker conditions are

$$g_N \geq 0, \qquad \sigma_N \leq 0, \qquad g_N\ \sigma_N = 0 \quad \text{on } \Gamma_{C,S}. \tag{1.4}$$

The first condition ensures the non-penetration of the subdomains, the second one ensures a compressive resulting reaction and the third one ensures the complementary condition, i.e., either an active contact and thus a compressive force or an inactive contact and thus a separation of the subdomains.

Let $\Omega_k \subset \mathbb{R}^d$, d the dimension being 2 or 3, be a bounded subdomain which is subjected to an internal load $\boldsymbol{f_k}$ and different boundary conditions on its boundary $\partial\Omega_k$.

The static balance equation relative to $\Omega = \bigcup_k \Omega_k$ with either $k = \{S\}$ in the rigid-deformable case or $k = \{S,\ M\}$ in the deformable-deformable case is written as

$$\begin{cases} -\mathbf{div}(\underline{\underline{\sigma_k}}) &= \boldsymbol{f_k} & \text{in } \Omega_k, \\ \boldsymbol{u_k} &= \boldsymbol{u_{D,k}} & \text{on } \Gamma_{D,k}, \\ \underline{\underline{\sigma_k}} \cdot \boldsymbol{n_k} &= \boldsymbol{l_k} & \text{on } \Gamma_{N,k}. \\ g_N \geq 0, \sigma_N &\leq 0, g_N\ \sigma_N = 0 & \text{on } \Gamma_{C,S}, \end{cases} \tag{1.5}$$

where $\boldsymbol{n_k}$ is the outward normal on $\partial\Omega_k$, $\boldsymbol{u_k} \in \mathbb{R}^{d_u}$ is the displacement, $\underline{\underline{\sigma_k}}$ and $\underline{\underline{\varepsilon_k}}$ are respectively the stress and strain tensors relative to the subdomain Ω_k. Under plane linear isotropic elastic assumptions, it holds:

$$\underline{\underline{\sigma_k}} = \lambda_{\text{Lamé},k}\ tr(\underline{\underline{\varepsilon_k}})\ \underline{\underline{\mathbb{I}}} + 2\ \mu_{\text{Lamé},k}\ \underline{\underline{\varepsilon_k}} \quad \text{and} \quad \underline{\underline{\varepsilon_k}} = \frac{1}{2}\left(\underline{\underline{\nabla \boldsymbol{u_k}}} + (\underline{\underline{\nabla \boldsymbol{u_k}}})^T\right) = \underline{\underline{\nabla^s \boldsymbol{u_k}}},$$

where $\mathbf{div}$, ∇ and ∇^s stand respectively for the standard divergence, gradient and symmetric gradient operators, $\lambda_{\text{Lamé},k}$ and $\mu_{\text{Lamé},k}$ for the Lamé coefficients. We note that the the Lamé coefficients are related to the Young modulus E_k and the Poisson ratio ν_k via the following relations:

$$\lambda_{\text{Lamé},k} = \frac{E_k\ \nu_k}{(1+\nu_k)(1-2\nu_k)}, \qquad \mu_{\text{Lamé},k} = \frac{E_k}{2\,(1+\nu_k)}.$$

Herein, we have just recalled the balance equation relative to the assumptions done, for more details about solid mechanics see, e.g., [15, 75].

1.3.2 Weak formulation

Hereafter, we present the functional framework relative to each contact case in order to introduce weak contact formulations for the problem stated in Equation (1.5).

We use standard Sobolev spaces, as defined in [51], endowed with their usual norms.

Rigid-deformable contact framework On Ω_S, we consider the Sobolev space

$$V = (H^1(\Omega_S))^{d_u},$$

endowed with the norm $\|\boldsymbol{v}\|_V^2 = \|\boldsymbol{v}\|^2_{(H^1(\Omega_S))^{d_u}}$, which is the classical H^1 vectorial norm in Ω_S, and its subspaces

$$V_D = \{\boldsymbol{v} \in V, \quad \boldsymbol{v} = \boldsymbol{u_{D,S}} \quad \text{on } \Gamma_{D,S}\,\},$$

$$V_0 = \{\boldsymbol{v} \in V, \quad \boldsymbol{v} = \boldsymbol{0} \quad \text{on } \Gamma_{D,S}\}.$$

We introduce $[\boldsymbol{v}]$ the classical jump of $\boldsymbol{v}$ defined as $[\boldsymbol{v}] = \boldsymbol{v_S} \cdot \boldsymbol{n_M}$.

In order to define weak formulations of the considered contact problem, we define the following linear and bilinear forms:

$$a\colon V \times V \to \mathbb{R}, \qquad a(\boldsymbol{u},\boldsymbol{v}) = \int_{\Omega_S} \lambda_{\text{Lamé,S}}\ \mathbf{div}(\boldsymbol{u}) \cdot \mathbf{div}(\boldsymbol{v}) + 2\,\mu_{\text{Lamé,S}}\, \underline{\underline{\nabla^s \boldsymbol{u}}} : \underline{\underline{\nabla^s \boldsymbol{v}}}\ \mathrm{d}x,$$

$$f\colon V \to \mathbb{R}, \qquad f(\boldsymbol{v}) = \int_{\Omega_S} \boldsymbol{f_S} \cdot \boldsymbol{v}\ \mathrm{d}x\ + \int_{\Gamma_{N,S}} \boldsymbol{l_S} \cdot \boldsymbol{v}\ \mathrm{d}s.$$

Deformable-deformable contact framework On $(\Omega_S \cup \Omega_M)$, we consider the broken Sobolev space

$$V = \prod_{k=\{S,\,M\}} V_k = \prod_{k=\{S,\,M\}} (H^1(\Omega_k))^{d_u}$$

endowed with the broken norm $\|\boldsymbol{v}\|_V^2 = \sum_{k=\{S,\,M\}} \|\boldsymbol{v}\|^2_{(H^1(\Omega_k))^{d_u}}$, and its subspaces

$$V_D = \{\boldsymbol{v} \in V, \quad \boldsymbol{v} = \boldsymbol{u_{D,k}} \quad \text{on } \Gamma_{D,k} \quad k = \{S,\, M\}\},$$

$$V_0 = \{\boldsymbol{v} \in V, \quad \boldsymbol{v} = \boldsymbol{0} \quad \text{on } \Gamma_{D,k} \quad k = \{S,\, M\}\}.$$

$[\boldsymbol{v}]$ the classical jump of $\boldsymbol{v}$ is defined in this case by $[\boldsymbol{v}] = (\boldsymbol{v_S} - \overline{\boldsymbol{v}}_{\boldsymbol{M}}) \cdot \boldsymbol{n_M}$.

We also define the following linear and bilinear forms:

$$a\colon V \times V \to \mathbb{R}, \qquad a(\boldsymbol{u},\boldsymbol{v}) = \sum_{k=\{S,\,M\}} \int_{\Omega_k} \lambda_{\text{Lamé,k}}\ \mathbf{div}(\boldsymbol{u}) \cdot \mathbf{div}(\boldsymbol{v}) + 2\,\mu_{\text{Lamé,k}}\, \underline{\underline{\nabla^s \boldsymbol{u}}} : \underline{\underline{\nabla^s \boldsymbol{v}}}\ \mathrm{d}x,$$

$$f\colon V \to \mathbb{R}, \qquad f(\boldsymbol{v}) = \sum_{k=\{S,\,M\}} \int_{\Omega_k} \boldsymbol{f_k} \cdot \boldsymbol{v}\ \mathrm{d}x\ + \sum_{k=\{S,\,M\}} \int_{\Gamma_{N,k}} \boldsymbol{l_k} \cdot \boldsymbol{v}\ \mathrm{d}s.$$

In the following, we give three different weak formulations based on the way the contact constraints are taken account, namely a penalty formulation, a Lagrange multiplier formulation and an augmented Lagrangian multiplier formulation. We note that we restrict the study to these three formulations but point out that others exist such as Nitsche's formulations, see, e.g., [26, 27, 46, 25].

Penalty formulation Find $\boldsymbol{u} \in V_D$ such that

$$a(\boldsymbol{u},\,\boldsymbol{v}) + \int_{\Gamma_{C,S}} \varepsilon\ <g_N>_-\ [\boldsymbol{v}]\ \mathrm{d}s\ =\ f(\boldsymbol{v}), \qquad \forall \boldsymbol{v} \in V_0 \tag{1.6}$$

with $<\cdot>_-$ the Macauley bracket and ε the penalty parameter that has to be infinite to ensure an exact contact constraint enforcement.

We note that the Macauley bracket is here considered defined as:

$$<a>_- = \begin{cases} 0 & \text{if } a \geq 0, \\ a & \text{if } a < 0. \end{cases} \tag{1.7}$$

The contact pressure is expressed as $\sigma_N = \varepsilon\, g_N$.

Lagrange multiplier formulation This formulation requires a multiplier space. On the contact interface $\Gamma_{C,S} \subset \partial\Omega_S$, we define by $H^{-1/2}(\Gamma_{C,S})$ the dual space of $H^{1/2}(\Gamma_{C,S})$, which is the space of all functions that can be extended on $\partial\Omega_S \setminus \Gamma_{C,S}$ to an element of $H^{1/2}(\partial\Omega_S)$. We then introduce a multiplier space M defined by

$$M = \{\phi \in H^{-1/2}(\Gamma_{C,S})\},$$

as its subspace

$$M^- = \{\phi \in M, \quad \int_{\Gamma_{C,S}} \phi\, [\boldsymbol{u}]\ \mathrm{d}s \leq 0, \quad \forall\, [\boldsymbol{u}] \in H^{1/2}(\Gamma_{C,S}), \quad [\boldsymbol{u}] \geq 0\}.$$

We also define the following bilinear and linear forms:

$$b\colon V \times M \to \mathbb{R}, \qquad b(\boldsymbol{u},\, \phi) = \int_{\Gamma_{C,S}} \phi\, [\boldsymbol{u}]\ \mathrm{d}s,$$

$$g\colon M \to \mathbb{R}, \qquad g(\phi) = \int_{\Gamma_{C,S}} \phi\, g\ \mathrm{d}s.$$

A mixed formulation of the contact problem is: find $(\boldsymbol{u},\, \lambda) \in V_D \times M^-$ such that

$$\begin{cases} a(\boldsymbol{u},\, \boldsymbol{v}) + b(\boldsymbol{v}, \lambda) = f(\boldsymbol{v}), & \forall \boldsymbol{v} \in V_0, \\ b(\boldsymbol{u},\, \lambda - \phi) \leq -g(\lambda - \phi), & \forall \phi \in M^-. \end{cases} \tag{1.8}$$

The constraint conditions have been transferred to the dual variable.

It is well known that this problem admits a unique solution, see, e.g., [52] and that the multiplier, taken here as a scalar, is directly related to the contact pressure by

$$\lambda = \sigma_N = (\underline{\underline{\sigma_S}} \cdot \boldsymbol{n_S}) \cdot \boldsymbol{n_S} = -(\underline{\underline{\sigma_S}} \cdot \boldsymbol{n_S}) \cdot \boldsymbol{n_M}.$$

Augmented Lagrangian multiplier formulation See, e.g., [49, 1, 93, 97]. This formulation also requires a multiplier space, defined here as $M = L^2(\Gamma_{C,S})$. Another mixed formulation of the contact problem is: find

$(\boldsymbol{u},\, \lambda) \in V_D \times M$ such that

$$\begin{cases} a(\boldsymbol{u},\, \boldsymbol{v}) \,+\, \displaystyle\int_{\Gamma_{C,S}} <\lambda \,+\, \varepsilon\, g_N>_- \,[\boldsymbol{v}]\, \mathrm{d}s = \, f(\boldsymbol{v}), & \forall \boldsymbol{v} \in V_0, \\ \displaystyle\int_{\Gamma_{C,S}} \frac{1}{\varepsilon} \,<\lambda \,+\, \varepsilon\, g_N>_- \,\phi \;\mathrm{d}s \,-\, \int_{\Gamma_{C,S}} \frac{1}{\varepsilon}\, \lambda\, \phi \;\mathrm{d}s \;=\; 0, & \forall \phi \in M. \end{cases} \tag{1.9}$$

with $<\cdot>_-$ the Macauley brackets (see (1.7)) and ε a penalty parameter.

We note that in this later case the penalty parameter should not necessarily be large to enforce the contact constraints as more than one term contributes to the constraint imposition.

We point out that this later formulation can only be set by requiring more regularity on the multiplier λ, i.e., assuming it is in $L^2(\Gamma_{C,S})$. Otherwise the sign notion encountered in the Macauley brackets has no meaning.

The contact pressure is in this case $\sigma_N = \lambda + \varepsilon\, g_N = \lambda$.

Remark 4. *In the following we consider as weak formulations of the contact problem stated in Equation (1.5), the formulations given above. Although, we would like to recall that the following problems are equivalent:*

- $\boldsymbol{u}$*, solution of the considered contact mechanical equilibrium, Equation (1.5), is the solution of the variational inequality*
  find $\boldsymbol{u} \in K$ *with* $K = \{\boldsymbol{v} \in V_D, \quad g_N \geq 0 \quad$ *on* $\Gamma_{C,S}\}$ *such that*

  $$a(\boldsymbol{u},\, \boldsymbol{v} - \boldsymbol{u}) \;\geq\; f(\boldsymbol{v} - \boldsymbol{u}) \qquad \forall\, \boldsymbol{v} \in K,$$

  and of the following energy minimisation problem

  $$\boldsymbol{u} \text{ in } K, \quad \mathcal{J}(\boldsymbol{u}) = \min_{\boldsymbol{v} \in K} \mathcal{J}(\boldsymbol{v})$$

  with $\mathcal{J}(\boldsymbol{v}) = \dfrac{1}{2}\, a(\boldsymbol{v},\, \boldsymbol{v}) - f(\boldsymbol{v})$.

- $(\boldsymbol{u}, \lambda)$ *is the solution of the problem (1.8) and thus it is the saddle-point of the functional* $\mathcal{L}(\cdot,\, \cdot)$ *over* $V_D \times H^{-1/2}(\Gamma_{C,S})$ *with*

  $$\mathcal{L}(\boldsymbol{v}, \phi) = \frac{1}{2}\, a(\boldsymbol{v}, \boldsymbol{v}) - f(\boldsymbol{v}) + b(\boldsymbol{v}, \phi) = \mathcal{J}(\boldsymbol{v}) + b(\boldsymbol{v}, \phi).$$

  Moreover, if we restrict to $V_D \times L^2(\Gamma_{C,S})$, $(\boldsymbol{u}, \lambda)$ *is also the solution of the problem (1.9) and thus it is the saddle-point of the functional* $\mathcal{L}_{\mathcal{A}}(\cdot,\, \cdot)$ *over*

$V_D \times L^2(\Gamma_{C,S})$ *with*

$$\begin{aligned}\mathcal{L}_{\mathcal{A}}(\boldsymbol{v},\phi) &= \tfrac{1}{2}\,a(\boldsymbol{v},\boldsymbol{v}) - f(\boldsymbol{v}) + b(\boldsymbol{v},\phi) + \tfrac{\varepsilon}{2}\int_{\Gamma_{C,S}} {g_N}^2\,\mathrm{d}s \\ &= \mathcal{L}(\boldsymbol{v},\phi) + \tfrac{\varepsilon}{2}\int_{\Gamma_{C,S}} {g_N}^2\,\mathrm{d}s.\end{aligned}$$

We note that the ellipticity property of $\mathcal{L}_{\mathcal{A}}(\cdot,\cdot)$ contributes to the robustness of augmented Lagrangian methods compared to Lagrange multiplier ones.

We refer to [50, 49, 14, 58, 52, 62] for more theoretical details.

1.3.3 Discretization

Let us now set the different approximation spaces in each contact case.

Rigid-deformable contact framework Ω_S is approximated by a NURBS parametrization $\mathbf{F}_S$ based on a knot vector $\boldsymbol{\Xi}_S$ and a degree p_S, see Subsection 1.1.3, such that Ω_S is the image of the parametric space $\widehat{\Omega}$ by $\mathbf{F}_S$.

Herein, h stands for the mesh parameter and in this context it is equal to h_S.

On Ω_S, based on the NURBS parametrization, we introduce the displacement approximation space $V_h = \{\boldsymbol{v} = \widehat{\boldsymbol{v}} \circ \mathbf{F}_S^{-1}, \widehat{\boldsymbol{v}} \in (N^{p_S}(\boldsymbol{\Xi}_S))^{d_u}\} \subset V$ and analogously its subspaces $V_{0,h}$ and $V_{D,h}$ which contain respectively the homogeneous and inhomogeneous Dirichlet conditions.

Deformable-deformable contact framework In this case, each subdomain Ω_k is approximated by a NURBS parametrization $\mathbf{F}_k$ based on a knot vector $\boldsymbol{\Xi}_k$ and a degree p_k, see Subsection 1.1.3, such that Ω_k is the image of the parametric space $\widehat{\Omega}$ by $\mathbf{F}_k$. Herein, h stands for the global mesh parameter defined as the maximal mesh parameter, i.e., $h = \max_{k=\{S,\,M\}} h_k$.

On each subdomain Ω_k, based on the NURBS parametrization, we introduce the displacement approximation space $V_{k,h} = \{\boldsymbol{v_k} = \widehat{\boldsymbol{v}}_{\boldsymbol{k}} \circ \mathbf{F}_k^{-1}, \widehat{\boldsymbol{v}}_{\boldsymbol{k}} \in (N^{p_k}(\boldsymbol{\Xi}_k))^{d_u}\}$.

On $(\Omega_S \cup \Omega_M)$, we define the discrete product space $V_h = \prod_{k=\{S,\,M\}} V_{k,h} \subset V$, which forms a $(H^1(\Omega_S \cup \Omega_M))^{d_u}$ non-conforming space discontinuous over the potential region of contact $\Gamma_{C,S}$, and analogously its subspaces $V_{0,h}$ and $V_{D,h}$ which contain respectively the homogeneous and inhomogeneous Dirichlet conditions.

We point out that under the assumptions done on the meshes, Assumption 1, and parametrizations, Assumption 2, the introduced NURBS spaces have optimal approximation properties, see Lemma 3 and, e.g., [5, 6].

Moreover, we precise that the potential contact area $\Gamma_{C,S}$ is defined as the mapping of a full boundary of the parametric space $\widehat{\Omega}$ by the slave parametrization $\mathbf{F}_S$.

In the following, we give the semi-discrete formulations of the weak formulations introduced in Subsection 1.3.2 by simply applying the Galerkin method. Clearly, in order to have a full discrete problem we should specify the numerical treatment of the contact non-linearity and the choice of multiplier spaces. This is the object of Chapters 4 and 5.

The semi-discrete problems can be written as follows:

Penalty formulation

Find $\boldsymbol{u_h} \in V_{D,h}$ such that

$$a(\boldsymbol{u_h}, \boldsymbol{v_h}) + \int_{\Gamma_{C,S}} \varepsilon < (g_N)_h >_- [\boldsymbol{v_h}] \, \mathrm{d}s = f(\boldsymbol{v_h}), \qquad \forall \boldsymbol{v_h} \in V_{0,h}.$$

We note the use of the notation $(g_N)_h$ to refer to the discrete gap which has to be defined to characterise completely the numerical contact methods.

Remark 5. *Even though we introduce a weak penalty formulation of the considered contact problem, see (1.6), this discrete penalty formulation has not to be seen as its discretisation. Indeed, once a constraint enforcement is done by penalisation, its solution is the constraint problem solution if and only if the penalty parameter is infinite which is never reached in practise. Otherwise it has a different solution which depends on the penalty parameter value. For this reason, it is more correct to say that the discrete formulation is penalised to impose the contact constraints than to mention that a penalty formulation is discretised. In this later case, you are trying to approximate a solution of a slightly different problem. In other word, the discretisation is done before the constraint penalisation to approximate the solution of the desired problem.*

The penalty parameter affects the conditioning number of the underlying matrix system which affects the solver efficiency. Moreover, it also influences the order of convergence of the numerical methods. Indeed, it is

well-known that this parameter should be taken as a function of the mesh parameter h to keep the optimality of the method, otherwise it is introducing a threshold error value which is reached at a certain refinement level.

The penalty parameter is defined as a compromise between a not so high value to ensure a not so bad matrix conditioning and a enough high value to ensure a fair constraint enforcement.

We note that it is typical for a penalty contact method to have gap values that do not fulfill exactly (1.4).

Lagrange multiplier formulation

Find $(\boldsymbol{u_h},\, \lambda_h) \in V_{D,h} \times M_h^-$ such that

$$\begin{cases} a(\boldsymbol{u_h},\, \boldsymbol{v_h}) \,+\, b(\boldsymbol{v_h}, \lambda_h) \,=\, f(\boldsymbol{v_h}), & \forall \boldsymbol{v_h} \in V_{0,h}, \\ b(\boldsymbol{u_h},\, \lambda_h - \phi_h) \,\leq\, -g(\lambda_h - \phi_h), & \forall \phi_h \in M_h^-. \end{cases} \tag{1.10}$$

This formulation contains dual constraints and thus is requiring special numerical strategies to be solved. We refer to [57, 59] for some works on this topic.

Augmented Lagrangian multiplier formulation

Find $(\boldsymbol{u_h},\, \lambda_h) \in V_{D,h} \times M_h$ such that

$$\begin{cases} a(\boldsymbol{u_h},\, \boldsymbol{v_h}) \,+\, \displaystyle\int_{\Gamma_{C,S}} <\lambda_h \,+\, \varepsilon\, (g_N)_h>_- \,[\boldsymbol{v_h}]\, \mathrm{d}s \,=\, f(\boldsymbol{v_h}), & \forall \boldsymbol{v_h} \in V_{0,h}, \\ \displaystyle\int_{\Gamma_{C,S}} \frac{1}{\varepsilon} \,<\lambda_h \,+\, \varepsilon\, (g_N)_h>_- \,\phi_h \;\mathrm{d}s \,-\, \int_{\Gamma_{C,S}} \frac{1}{\varepsilon}\, \lambda_h\, \phi_h \;\mathrm{d}s \,=\, 0, & \forall \phi_h \in M_h. \end{cases} \tag{1.11}$$

We also use here the notation $(g_N)_h$ to refer to the discrete gap which has to be defined to characterise completely the numerical contact methods. We point out that its discrete definition is involving the multiplier space, as the method has to be based on a sign check of the variable $(\lambda + \varepsilon g_N)$ which is approximated by one spline space, i.e., the multiplier one.

The main advantage of this later formulation is to be a formulation without any constraint. It is also a more robust method than the Lagrange multiplier ones, although it is requiring more matrix evaluation terms among them some of the stiffness matrix.

Chapter 2

Isogeometric mortar methods

Contents

2.1 Introduction

In this chapter we present the results of a study done on the application of mortar methods in the framework of isogeometric analysis. It is a joined work with A. Buffa, B. Wohlmuth and L. Wunderlich which has been published in [17].

The important point of a mortar method is the choice of the Lagrange multiplier. From the classical mixed and mortar theories, two abstract requirements for the Lagrange multiplier space are given, see [13, 8]. One is the sufficient approximation order, the other is the requirement of an inf-sup stability condition. For a primal spline space of degree p, we investigate three different degrees for the Lagrange multiplier: p, $p-1$ and $p-2$. Each choice is from some points of view natural but has quite different characteristical features.

This chapter is structured as follows. In Section 2.2, we give the main results on the proposed isogeometric mortar methods introduced in Chapter 1. In Section 2.3, we explicitly detail three different types of Lagrange multipliers. The theoretical results are investigated numerically in Section 2.4, where also additional aspects are considered.

2.2 Isogeometric mortar theory

Before giving the main results relative to our mortar methods, let us recall the discrete weak formulation we consider. It was stated in Equation (1.3) in Chapter 1. It consists in finding $(u_h, \lambda_h) \in V_h \times M_h$, such that:

$$\begin{cases} a(u_h, v_h) + b(v_h, \lambda_h) &= f(v_h), \quad v_h \in V_h, \\ b(u_h, \phi_h) &= 0, \quad \phi_h \in M_h. \end{cases}$$

It is well known that the following abstract requirements guarantee the method to be well-posed and of optimal order, see [8, 13]. In the following, we will denote by $0 < C < \infty$ a generic constant that is independent of the mesh sizes but possibly depends on p_k.

The first assumption is a uniform inf-sup stability for the discrete trace spaces. Although the primal variable of the saddle point problem is in a broken H^1 space, the inf-sup stability can be formulated as an L^2 stability

over each interface. This implies the $H_{00}^{1/2} - H^{-1/2}$ stability, which can be used in the geometrically conforming situation for $d = 2$ and in weighted L^2 norms, for the other cases, see [16].

Assumption 6. *For $l = 1, \dots, L$ and any $\phi_l \in M_{l,h}$ it holds*

$$\sup_{w_l \in W_{l,h}} \frac{\int_{\gamma_l} w_l \, \phi_l \, \mathrm{d}s}{\|w_l\|_{L^2(\gamma_l)}} \geq C \|\phi_l\|_{L^2(\gamma_l)}.$$

The second assumption is the approximation order of the dual space. Since for the dual space weaker norms are used, the approximation order of $M_{l,h}$ with respect to the L^2 norm can be smaller than the one of $W_{l,h}$.

Assumption 7. *For $l = 1, \dots, L$ there exists a fixed $\eta(l)$, such that for any $\lambda \in H^{\eta(l)}(\gamma_l)$ it holds*

$$\inf_{\lambda_h \in M_{l,h}} \|\lambda - \lambda_h\|_{L^2(\gamma_l)} \leq C h^{\eta(l)} \|\lambda\|_{H^{\eta(l)}(\gamma_l)}.$$

We now give the following a-priori estimates in the broken V and M norms, which can be shown by standard techniques, see [12, 10].

Theorem 8. *Given Assumptions 6 and 7, the following convergence is given for the primal solution of (1.3). For $u \in H^{\sigma+1}(\Omega)$, $1/2 < \sigma \leq \min_{k,l}(p_k, \eta(l) + 1/2)$ it holds*

$$\frac{1}{h^2} \|u - u_h\|_{L^2(\Omega)}^2 + \|u - u_h\|_V^2 \leq C \sum_{k=1}^{K} h_k^{2\sigma} \|u\|_{H^{\sigma+1}(\Omega_k)}^2.$$

We can also give an estimate for the dual solution which approximates the normal flux:

$$\sum_{l=1}^{L} \|\alpha \frac{\partial u}{\partial \mathbf{n}_l} - \lambda_h\|_{H^{-1/2}(\gamma_l)}^2 \leq C \sum_{k=1}^{K} h_k^{2\sigma} \|u\|_{H^{\sigma+1}(\Omega_k)}^2.$$

In the geometrically non-conforming case, as well as for $d = 3$, the ratio of the mesh sizes on the master and the slave side enters in the *a priori* estimate, see [70]. But due to our global quasi-uniformity assumption, see Assumption 1, this ratio does not play a role.

We note that if $\eta(l) = p_{S(l)} - 1/2$ can be chosen, optimality of the mortar method holds. Moreover, the dual estimate could still be improved under additional regularity assumptions, see [87].

Remark 9. *Isogeometric methods allow for smooth approximations, and thus they are of special interest for higher order PDEs. The abstract concept of mortar methods can also be used to couple higher derivatives resulting in weakly constrained solutions. In this case, multiple coupling conditions are necessary on each interface, see, e.g., [85, 117, 84]. As an example, for the biharmonic problem*

$$\Delta\Delta u = f \text{ in } \Omega, \quad u = 0,\ \partial_n u = 0 \text{ on } \Gamma,$$

the coupling terms on each interface γ_l are

$$\int_{\gamma_l} \phi_1 [u]_l \, \mathrm{d}s = 0, \quad \int_{\gamma_l} \phi_2 [\frac{\partial u}{\partial \mathbf{n_l}}]_l \, \mathrm{d}s = 0, \quad \phi_i \in M^i_{l,h}.$$

The Lagrange multipliers ϕ_1 and ϕ_2 from appropriate discrete spaces $M^1_{l,h}$ and $M^2_{l,h}$ approximate respectively the normal derivative $\frac{\partial \Delta u}{\partial \mathbf{n_l}}$ and the trace of Δu.

2.3 Possible choices of Lagrange multiplier spaces

For a given interface γ_l, we aim at providing multiplier spaces that satisfy the inf-sup stability of Assumption 6. In our setting, i.e., a geometrically slave conforming situation, see Figure 1.5, γ_l is a whole face of $\Omega_{S(l)}$, which is defined as $\mathbf{F}_{S(l)}(\widehat{\Omega})$ and without loss of generality we suppose that $\gamma_l = \mathbf{F}_{S(l)}(\widehat{\gamma} \times \{0\})$, $\widehat{\gamma} = (0,1)^{d-1}$. As we consider each interface γ_l separately, to shorten the notations we will omit the index l in the following.

Given a Lagrange multiplier space $\widehat{M}_h$ on the parametric space, we set the Lagrange multiplier space $M_h = \{\phi = \widehat{\phi} \circ \mathbf{F}_s^{-1}, \widehat{\phi} \in \widehat{M}_h\}$. By change of variable, the integral in Assumption 6 can be transformed into a weighted integral on the parametric space. Denoting $\widehat{w} = (w \circ \mathbf{F}_s)\, \widehat{DW} \in S^p(\widehat{\gamma})$ for $w \in W_h$ and $\widehat{\phi} = \phi \circ \mathbf{F}_s \in \widehat{M}_h$ for $\phi \in M_h$, the integral becomes

$$\begin{aligned} \int_\gamma w\, \phi \, \mathrm{d}s &= \int_{\widehat{\gamma}} (w \circ \mathbf{F}_s)\, (\phi \circ \mathbf{F}_s) \det(\nabla_{\hat{\gamma}} \mathbf{F}_s) \, \mathrm{d}x \\ &= \int_{\widehat{\gamma}} \widehat{w}\, \widehat{\phi}\, (\widehat{DW})^{-1} \det(\nabla_{\hat{\gamma}} \mathbf{F}_s) \, \mathrm{d}x, \end{aligned} \tag{2.1}$$

where $\nabla_{\hat{\gamma}}$ denotes the surface gradient on $\widehat{\gamma}$. Due to the Assumption 2 and the uniform positivity of NURBS weights, we can firstly concentrate on the following problem. Given $\widehat{\gamma} = (0,1)^{d-1}$, a degree p and knot vectors Ξ_δ with $\delta = 1, \ldots, d-1$, we denote by $S^p(\widehat{\gamma})$ the corresponding spline space

and $S_0^p(\widehat{\gamma}) = S^p(\widehat{\gamma}) \cap H_0^1(\widehat{\gamma})$, and study the following inf-sup stability

$$\sup_{\widehat{w} \in S_0^p(\widehat{\gamma})} \frac{\int_{\widehat{\gamma}} \widehat{w}\, \widehat{\phi}\, \mathrm{d}x}{\|\widehat{w}\|_{L^2(\widehat{\gamma})}} \geq C \|\widehat{\phi}\|_{L^2(\widehat{\gamma})}. \tag{2.2}$$

for any $\widehat{\phi} \in \widehat{M}_h$ for three choices of Lagrange multiplier spaces $\widehat{M}$. Then, in the case (2.2) is satisfied, we show that the desired inf-sup stability, i.e., Assumption 6, is satisfied.

In the following, we give the details of this inf-sup study, then conclude the underlying approximation properties of the isogeometric mortar methods and briefly comment on biorthogonal basis spaces.

2.3.1 Choice 1: unstable pairing $p/p-1$

Theorem 8 states that an order $p = \min_k p_k$ a priori bound can only be obtained if $\eta(l)$ can be set equal to $p - 1/2$. This observation motivates our choice to use a spline space of order $p-1$ as dual space. Then $\eta(l)$ in Assumption 7 can be set to p and provided that the uniform inf-sup stability, Assumption 6, can be proved, a convergence rate equal to p might be reached.

We denote by $\widehat{M}_h^1 = \mathrm{span}_{i=1,\dots,n_{\widehat{M}_h^1}} \{\widehat{B}_i^{p-1}\}$ the spline space of order $p-1$ built on the knot vector(s) Ξ'_δ with $\delta = 1, \dots, d-1$ obtained from the restriction of $\boldsymbol{\Xi}$ to the corresponding direction(s) removing in the underlying univariate knot vector the first and the last knots. The superscript 1 refers to the degree difference between the primal and the dual space.

As we will see this choice unfortunately lacks the uniform inf-sup condition (2.2) and thus also Assumption 6. Indeed, a checkerboard mode which yields an h-dependent inf-sup constant can be constructed.

Let us consider B-Splines on a uniform knot vector $\Xi = \{0, \dots, 0, h, 2h, \dots, 1, \dots, 1\}$ for $h = 2^{-j}$, where j is the number of uniform refinements. Let us now construct a multiplier $\widehat{\phi}_c \in \widehat{M}_h^1$, which yields an h-dependent inf-sup constant. The choice

$$\widehat{\phi}_c = \sum_{i=1}^{n_{\widehat{M}_h^1}} \widehat{\phi}_i \widehat{B}_i^{p-1}, \quad \widehat{\phi}_i = (-1)^i (i-1)(n_{\widehat{M}_h^1} - i),$$

is shown in Figure 2.1. For the bivariate case, a tensor product using $\widehat{\phi}_c$ in each direction is chosen. The numerical stability constants were computed

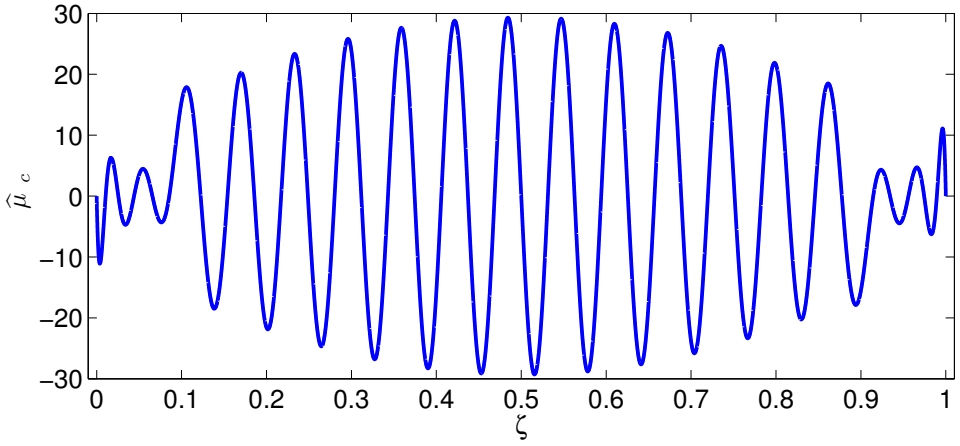

Figure 2.1: Checkerboard mode for $d = 2$ and $p = 6$.

by a direct evaluation of the supremum

$$\sup_{\widehat{w} \in S^p(\hat{\gamma})} \frac{\int_{\hat{\gamma}} \widehat{w}\, \widehat{\phi}_c \mathrm{d}x}{\|\widehat{w}\|_{L^2(\hat{\gamma})}},$$

and dividing the result by $\|\widehat{\phi}_c\|_{L^2(\hat{\gamma})}$. The results are shown in Figure 2.2 for $d = 2$ and $d = 3$, where an h-dependency of order $\mathcal{O}(h^{d-1})$ can be observed. Note that on the same mesh, the stability constant is larger for high degrees, but the asymptotic rate of the h-dependency is the same.

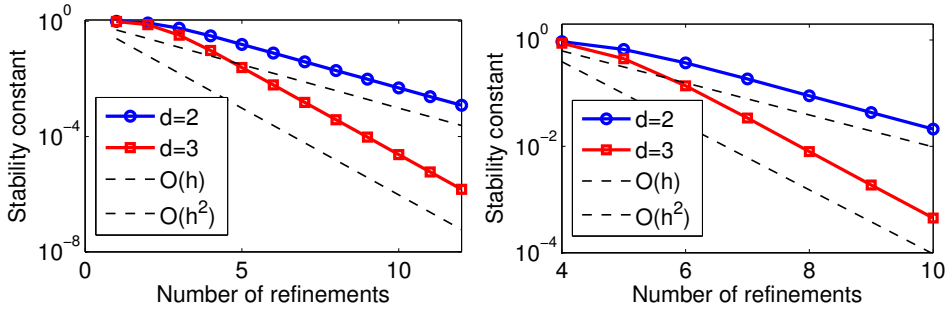

Figure 2.2: h-dependency of the L^2 inf-sup constant for dimension $d = 2$ and $d = 3$. Left: $p = 2$, Right: $p = 10$.

Remark 10. *Numerical experiments show that the inf-sup constant can be recovered by the use of a staggered grid, which is similar to the behavior known from the finite element methods. Another possibility is to use a coarse dual mesh for the Lagrange multipliers.*

2.3.2 Choice 2: stable pairing $p/p-2$

Having an unstable pairing means roughly speaking that the chosen Lagrange multiplier space is too rich. An easy way to overcome this is by using a smaller space which motivates our second choice. If the spline space $S^p(\widehat{\gamma})$ is at least C^1, then it is also possible to construct a spline space of degree $p-2$ on the knot vector(s) Ξ''_δ with $\delta = 1, \dots, d-1$ obtained from the restriction of $\boldsymbol{\Xi}$ to the corresponding direction(s) removing in the underlying univariate knot vector the first and the last two knots. We denote this space by $\widehat{M}_h^2 = \mathrm{span}_{i=1,\dots,n_{\widehat{M}_h^2}}\{\widehat{B}_i^{p-2}\}$, where the superscript 2 refers to the degree difference between the primal and the dual space. Clearly, this choice will never provide an order p convergence rate. The best approximation property of the Lagrange multiplier space only allows for a $p-1/2$ order convergence in the broken V and M norms, provided that the pairing is uniformly stable. In what follows, we prove that $\widehat{M}_h^2$ verifies the inf-sup stability (2.2).

Remark 11. *We recall that the internal knot multiplicity is the same for the primal and the dual space, noting that the requirement $S^p \subset C^1$ yields a primal maximal knot multiplicity of $p-1$. It is obvious to see that this requirement can be weakened in one direction: indeed if the univariate knot vector of the primal space is a h-refinement of the univariate knot vector of the dual space, the inf-sup stability remains satisfied. Beyond this setting, the proposed proof does not apply in general.*

The proof is based on an identification of both spaces using derivatives and integrals as well as on an auxiliary stability result for the degree $p-1$. Let us first introduce some preliminary notation.

To shorten our notation, we denote by S^q with $q = p-2, p-1$, and p the spline spaces of degree q constructed on $\boldsymbol{\Xi}'', \boldsymbol{\Xi}'$ and $\boldsymbol{\Xi}$, respectively. Furthermore let us define the spline space with zero mean value $S^{p-1}_{\mathrm{zmv}} = \{\widehat{s} \in S^{p-1} : \int_0^1 \widehat{s}\,\mathrm{d}x = 0\}$ for $d=2$ and

$$S^{p-1}_{\mathrm{zmv}} = \left\{ \widehat{s} \in S^{p-1} : \int_0^1 \widehat{s}(x,\bar{y})\mathrm{d}x = 0 = \int_0^1 \widehat{s}(\bar{x},y)\mathrm{d}y, \quad \bar{x},\bar{y} \in [0,1] \right\},$$

for $d=3$. While for $d=2$, we consider a single derivative $D = \partial_x$ as the derivative operator, for $d=3$, due to the tensor product structure, we also consider the mixed derivative $D = \partial_{xy}$. Associated with the mixed

derivative, we consider the tensor product Sobolev space

$$H^{1,1}(\widehat{\gamma}) = H^1(0,1) \otimes H^1(0,1) = \{\widehat{v} \in L^2(\widehat{\gamma}) : \partial_x^i \partial_y^j \widehat{v} \in L^2(\widehat{\gamma}), i,j \in \{0,1\}\},$$

endowed with the norm $\|\widehat{v}\|^2_{H^{1,1}(\widehat{\gamma})} = \|\widehat{v}\|^2_{H^1(\widehat{\gamma})} + \|\partial_{xy}\widehat{v}\|^2_{L^2(\widehat{\gamma})}$. To simplify the notation, we will denote in the following $Z = H^1(\widehat{\gamma})$ for $d = 2$ and $Z = H^{1,1}(\widehat{\gamma})$ for $d = 3$. Let Z' denotes the dual space of Z.

The following lemma shows that the given derivative operator maps bijectively the spaces S_0^p, S^{p-1}_{zmv} and S^{p-2} into each other.

Lemma 12. *The operators $D : S_0^p \to S^{p-1}_{\text{zmv}}$ and $D : S^{p-1}_{\text{zmv}} \to S^{p-2}$ are bijections. Moreover for any $v \in Z \cap H^1_0(\widehat{\gamma})$, it holds $\|v\|_{L^2(\widehat{\gamma})} \leq C\|Dv\|_{Z'}$.*

Proof. Based on [100, Theorem 5.9] the derivative of a spline of degree p is a spline of degree $p-1$, see also Section 1.1.1. The injectivity follows from the additional constraints of the spline space. To show the surjectivity, we construct an element of the pre-image space. Note that this property holds independently of the knot multiplicity, as long as S^{p-2} is well defined. The coercivity of the derivative can be seen by an explicit computation using partial integration.

Case $d = 2$. Given $\widehat{s}^{p-2} \in S^{p-2}$, we define $\widehat{s}^{p-1}(x) = \int_0^x \widehat{s}^{p-2}(\xi)\mathrm{d}\xi - m$, where $m \in \mathbb{R}$ is chosen such that $\int_0^1 \widehat{s}^{p-1}\mathrm{d}x = 0$. Obviously $\widehat{s}^{p-1} \in S^{p-1}_{\text{zmv}}$. For any $\widehat{s}^{p-1} \in S^{p-1}_{\text{zmv}}$ we may define $\widehat{s}^{p}(x) = \int_0^x \widehat{s}^{p-1}(\xi)\mathrm{d}\xi$ and it holds $\widehat{s}^{p} \in S_0^p$.

To show the coercivity, consider any $\widehat{w} \in L^2(0,1)$. We can find $\widehat{z} \in H^1_{\text{zmv}}(0,1) = \{\widehat{z} \in Z : \int_0^1 \widehat{z}\,\mathrm{d}x = 0\}$, such that $\partial_x \widehat{z} = \widehat{w}$ and then

$$\begin{aligned}\|\widehat{v}\|_{L^2(\widehat{\gamma})} &= \sup_{\widehat{w}\in L^2(\widehat{\gamma})} \frac{\int_0^1 \widehat{v}\,\widehat{w}\,\mathrm{d}x}{\|\widehat{w}\|_{L^2(\widehat{\gamma})}} = \sup_{\widehat{z}\in H^1_{\text{zmv}}(\widehat{\gamma})} \frac{\int_0^1 \widehat{v}\,\partial_x\widehat{z}\,\mathrm{d}x}{|\widehat{z}|_Z} \\ &\leq C \sup_{\widehat{z}\in H^1_{\text{zmv}}(\widehat{\gamma})} \frac{\int_0^1 \widehat{z}\,\partial_x\widehat{v}\,\mathrm{d}x}{\|\widehat{z}\|_Z} \leq C\|\partial_x\widehat{v}\|_{Z'},\end{aligned}$$

where C is the Poincaré constant, i.e., $\|\widehat{z}\|_Z \leq C\,|\widehat{z}|_Z$ for $\widehat{z} \in H^1_{\text{zmv}}(\widehat{\gamma})$.

Case $d = 3$. Given $\widehat{s}^{p-2} \in S^{p-2}$, we construct the spline $\widehat{s}^{p-1}(x) = \int_0^x \int_0^y \widehat{s}^{p-2}(\xi,\eta)\,\mathrm{d}\eta\,\mathrm{d}\xi - \widehat{f}^{p-1}(x) - \widehat{g}^{p-1}(y) - m$, where $m \in \mathbb{R}$ and $\widehat{f}^{p-1}, \widehat{g}^{p-1}$ are univariate splines of degree $p-1$ with zero mean value. These unknowns can be chosen such that $\widehat{s}^{p-1} \in S^{p-1}_{\text{zmv}}$. As for the univariate case, given $\widehat{s}^{p-1} \in S^{p-1}_{\text{zmv}}$ we consider $\widehat{s}^{p}(x,y) = \int_0^x \int_0^y \widehat{s}^{p-1}(\xi,\eta)\,\mathrm{d}\eta\,\mathrm{d}\xi$ and it holds $\widehat{s}^{p} \in S_0^p$.

For the proof of the coercivity, partial integration needs to be performed twice. The integration will be shown in more details in the proof of Theorem 14. □

To apply the bijectivity of the derivative in the proof of the inf-sup condition, we can no longer work with the L^2 norm, but need to consider the Z' and Z norms. Let us remark that $S^{p-1} \subset Z$ holds independently of the knot multiplicity because of the assumption $S^p \subset C^1$.

The following lemma states an auxiliary stability result in these norms.

Lemma 13. *For any $\widehat{g}^{p-1} \in S^{p-1}_{\mathrm{zmv}}$, it holds*

$$\sup_{\widehat{f}^{p-1} \in S^{p-1}_{\mathrm{zmv}}} \frac{\int_{\widehat{\gamma}} \widehat{g}^{p-1} \widehat{f}^{p-1} \,\mathrm{d}x}{\|\widehat{f}^{p-1}\|_{Z'}} \geq C \|\widehat{g}^{p-1}\|_{Z}.$$

Proof. The equal order pairing $Z - Z'$ inf-sup condition of S^{p-1} is first considered by introducing the Fortin operator $\Pi : L^2 \to S^{p-1}$ and proving its Z stability. Then we show that the inf-sup condition remains satisfied for the constrained space S^{p-1}_{zmv}. Since the infimum over a sub-space is an upper-bound of the infimum over a space, the critical part is the restriction of the primal space.

Case $d = 2$. Standard techniques show that the Fortin operator associated with S^{p-1}, which is the L^2-projection, is uniformly Z stable, see, e.g., [70, Lemma 1.8]. Thus the $Z - Z'$ inf-sup condition holds on S^{p-1}, i.e., for $\widehat{q}^{p-1} \in S^{p-1}$ it holds,

$$\sup_{\widehat{r}^{p-1} \in S^{p-1}} \frac{\int_{\widehat{\gamma}} \widehat{r}^{p-1} \widehat{q}^{p-1} \,\mathrm{d}x}{\|\widehat{r}^{p-1}\|_{Z}} \geq C \|\widehat{q}^{p-1}\|_{Z'}. \tag{2.3}$$

Next, we show that the restriction to S^{p-1}_{zmv} retains this stability.

Let us consider $\widehat{f}^{p-1} \in S^{p-1}_{\mathrm{zmv}}$, since the inf-sup condition remains satisfied for $\widehat{q}^{p-1} \in S^{p-1}$ and $\widehat{f}^{p-1} \in S^{p-1}_{\mathrm{zmv}}$. Let us define $\widehat{g}^{p-1} \in S^{p-1}_{\mathrm{zmv}}$ such that $\widehat{g}^{p-1}(x) = \widehat{q}^{p-1}(x) - \int_{\widehat{\gamma}} \widehat{q}^{p-1}(\xi) \mathrm{d}\xi \in S^{p-1}_{\mathrm{zmv}}$ and note that for $\widehat{f}^{p-1} \in S^{p-1}_{\mathrm{zmv}}$

$$\int_{\widehat{\gamma}} \widehat{f}^{p-1} \widehat{q}^{p-1} \mathrm{d}x = \int_{\widehat{\gamma}} \widehat{f}^{p-1} \widehat{g}^{p-1} \mathrm{d}x$$

and $\|\widehat{g}^{p-1}\|_Z \leq \|\widehat{q}^{p-1}\|_Z$. This shows

$$\inf_{\widehat{f}^{p-1}\in S^{p-1}_{\mathrm{zmv}}} \sup_{\widehat{g}^{p-1}\in S^{p-1}_{\mathrm{zmv}}} \frac{\int_{\widehat{\gamma}} \widehat{g}^{p-1}\widehat{f}^{p-1}\,\mathrm{d}x}{\|\widehat{f}^{p-1}\|_{Z'}\|\widehat{g}^{p-1}\|_Z} \geq C > 0.$$

Now using [13, Proposition 3.4.3], we interchange the spaces of the infimum and the supremum which yields the result.

Case $d = 3$. Although we follow the same structure as in the case $d = 2$, there are some essential differences. We note that $Z = H^{1,1}(\widehat{\gamma})$ is no longer a standard Sobolev space, and thus the Z stability of the Fortin operator cannot be shown as in the case $d = 2$. Instead, we make use of a tensor product of the univariate Fortin operators. See [7] for another application of a tensor product of projection operators.

We first show, that the tensor product of univariate L^2-projections is the multivariate L^2-projection, i.e., the Fortin operator. Then we show that the H^1 stability of the univariate projections yield the Z stability of their tensor product. We define $\overline{\Pi}_i : L^2(0,1) \to S^{p-1}(\Xi_i)$ as the L^2-projection into the univariate spline spaces. Their tensor product $\Pi = \overline{\Pi}_1 \otimes \overline{\Pi}_2$ is defined as described in the following. We first extend the projections to $\widehat{\gamma}$ by $\Pi_1 : L^2(\widehat{\gamma}) \to L^2(\widehat{\gamma})$ and $\Pi_2 : L^2(\widehat{\gamma}) \to L^2(\widehat{\gamma})$, such that

$$[\Pi_1\widehat{f}](\xi,\eta) = [\overline{\Pi}_1\bar{f}_\eta](\xi), \quad [\Pi_2\widehat{f}](\xi,\eta) = [\overline{\Pi}_2\bar{f}_\xi](\eta).$$

Here $\bar{f}_\eta$ denotes the univariate function depending on ξ, where the coordinate η plays the role of a parameter. $\bar{f}_\xi$ is defined analogously and it holds $\widehat{f}(\xi,\eta) = \bar{f}_\xi(\eta) = \bar{f}_\eta(\xi)$. Now the tensor product of the projections can be defined as $\Pi = \overline{\Pi}_1 \otimes \overline{\Pi}_2 : L^2(\widehat{\gamma}) \to S^{p-1}$ by $\overline{\Pi}_1 \otimes \overline{\Pi}_2 = \Pi_1 \circ \Pi_2 = \Pi_2 \circ \Pi_1$.

Applying the univariate projection property of $\overline{\Pi}_i$, a direct calculation shows that Π is the L^2-projection into S^{p-1}. Let $\widehat{B}_{i,1}, \widehat{B}_{j,2}$ denote the univariate basis functions in the two parametric directions, then we get

$$\int_{\widehat{\gamma}} (\Pi\widehat{v})(x,y)\widehat{B}_{i,1}(x)\widehat{B}_{j,2}(y)\,\mathrm{d}x\,\mathrm{d}y \quad = \int_{\widehat{\gamma}} \widehat{v}(x,y)\widehat{B}_{i,1}(x)\widehat{B}_{j,2}(y)\,\mathrm{d}x\,\mathrm{d}y.$$

For a fixed $\bar{x}, \bar{y} \in (0,1)$, we denote $I_{\bar{y}} = \{(x,\bar{y}) \in (0,1)^2\}$ and $I_{\bar{x}} = \{(\bar{x},y) \in (0,1)^2\}$. For the calculation, we need the two steps resulting from the univariate stability of the unidirectional projectors in $L^2(I_k)$ and $H^1(I_k)$ for $k = \overline{x}$ or $\overline{y}$:

First, for any $\bar{y} \in (0,1)$, we have

$$\begin{aligned}\|\partial_{xy}\Pi_1\widehat{w}\|_{L^2(I_{\bar{y}})} &= \|\partial_x\Pi_1(\partial_y\widehat{w})\|_{L^2(I_{\bar{y}})} = |\Pi_1(\partial_y\widehat{w})|_{H^1(I_{\bar{y}})} \leq C\|\partial_y\widehat{w}\|_{H^1(I_{\bar{y}})} \\ &= C\|\partial_y\widehat{w}\|_{L^2(I_{\bar{y}})} + C\|\partial_{xy}\widehat{w}\|_{L^2(I_{\bar{y}})}\end{aligned}$$

We will use this result for $\widehat{w} = \Pi_2\widehat{v}$. Of course the analogue result for Π_2 and any $\bar{x} \in (0,1)$ also holds.

Hence, we see

$$\begin{aligned}\|\partial_{xy}\Pi\widehat{v}\|^2_{L^2(\widehat{\gamma})} &= \int_{y\in I^2} \|\partial_{xy}\Pi\widehat{v}\|^2_{L^2(I_y)}\,\mathrm{d}y \\ &\leq \int_{y\in I^2} \|\partial_y\Pi_2\widehat{v}\|^2_{L^2(I_y)}\,\mathrm{d}y + \int_{y\in I^2} \|\partial_{xy}\Pi_2\widehat{v}\|^2_{L^2(I_y)}\,\mathrm{d}y \\ &= \int_{x\in I^1} \|\partial_y\Pi_2\widehat{v}\|^2_{L^2(I_x)}\,\mathrm{d}x + \int_{x\in I^1} \|\partial_{xy}\Pi_2\widehat{v}\|^2_{L^2(I_x)}\,\mathrm{d}x \\ &\leq C\|\widehat{v}\|^2_Z,\end{aligned}$$

i.e., the operator is Z stable.

The $Z - Z'$ stability of S^{p-1}_{zmv} can be concluded similarly to the univariate case starting from the $Z - Z'$ inf-sup condition for $\widehat{q}^{p-1}$ and $\widehat{r}^{p-1} \in S^{p-1}$, see (2.3). We can consider $\widehat{f}^{p-1} \in S^{p-1}_{\mathrm{zmv}}$, since the inf-sup condition remains valid for $\widehat{q}^{p-1} \in S^{p-1}$ and $\widehat{f}^{p-1} \in S^{p-1}_{\mathrm{zmv}}$. Now we define $\widehat{g}^{p-1} \in S^{p-1}_{\mathrm{zmv}}$ such that $\widehat{g}^{p-1}(x,y) = \widehat{q}^{p-1}(x,y) - \widehat{s}^1_0(x) - \widehat{s}^2_0(y) - c \in S^{p-1}_{\mathrm{zmv}}$ with $\widehat{s}^1_0 \in S^{p-1}(\Xi_1), \widehat{s}^2_0 \in S^{p-1}(\Xi_2)$ and $c \in \mathbb{R}$, and note that for $\widehat{f}^{p-1} \in S^{p-1}_{\mathrm{zmv}}$ it holds

$$\int_{\widehat{\gamma}} \widehat{f}^{p-1}\widehat{q}^{p-1}\mathrm{d}x = \int_{\widehat{\gamma}} \widehat{f}^{p-1}\widehat{g}^{p-1}\mathrm{d}x.$$

Now, the $Z - Z'$ stability can be concluded by noting that $\|\widehat{g}^{p-1}\|_Z \leq \|\widehat{q}^{p-1}\|_Z$. The proof ends the same way as the case $d = 2$ using [13, Proposition 3.4.3]. □

It remains to combine these preliminary results to prove the main theorem of this section. We use the bijectivity between the spline spaces of different degrees, stated in Lemma 12, and partial integration to estimate the inf-sup term by the equal order $p - 1$ stability which was estimated in Lemma 13.

Theorem 14. *Let $p \geq 2$ and the knot vectors Ξ_δ, $\delta = 1, \ldots, d-1$, be such that $S^p(\widehat{\gamma}) \subset C^1(\widehat{\gamma})$. The dual space $\widehat{M}_h^2$ verifies*

$$\sup_{\widehat{w} \in S_0^p} \frac{\int_{\widehat{\gamma}} \widehat{\phi}\, \widehat{w}\, \mathrm{d}x}{\|\widehat{w}\|_{L^2(\hat{\gamma})}} \geq C \|\widehat{\phi}\|_{L^2(\hat{\gamma})}, \quad \widehat{\phi} \in \widehat{M}_h^2,$$

with a constant C independent of the mesh size, but possibly dependent on p.

Proof. As before, the cases $d = 2$ and $d = 3$ are considered separately. We perform partial integration, noting that in the bivariate case, a tensor product structure is exploited.

Given any $\widehat{\phi}^{p-2} \in S^{p-2}$, we may introduce $\widehat{g}^{p-1} \in S^{p-1}_{\mathrm{zmv}}$, such that $\partial_x \widehat{g}^{p-1} = \widehat{\phi}^{p-2}$ as constructed in Lemma 12.

For the case $d = 2$, partial integration yields

$$\sup_{\widehat{w}^p \in S_0^p} \frac{\int_{\widehat{\gamma}} \widehat{w}^p\, \widehat{\phi}^{p-2} \mathrm{d}x}{\|\widehat{w}^p\|_{L^2(\hat{\gamma})}} = \sup_{\widehat{w}^p \in S_0^p} \frac{\int_{\widehat{\gamma}} \widehat{w}^p\, \partial_x \widehat{g}^{p-1} \mathrm{d}x}{\|\widehat{w}^p\|_{L^2(\hat{\gamma})}} = \sup_{\widehat{w}^p \in S_0^p} \frac{\int_{\widehat{\gamma}} \widehat{g}^{p-1}\, \partial_x \widehat{w}^p \mathrm{d}x}{\|\widehat{w}^p\|_{L^2(\hat{\gamma})}}.$$

Now, let us denote $\widehat{f}^{p-1} = \partial_x \widehat{w}^p \in S^{p-1}_{\mathrm{zmv}}$ and use the coercivity of the derivative as stated in Lemma 12. Since ∂_x is bijective from S_0^p onto S^{p-1}_{zmv}, we have

$$\begin{aligned}\sup_{\widehat{w}^p \in S_0^p} \frac{\int_{\widehat{\gamma}} \widehat{g}^{p-1}\, \partial_x \widehat{w}^p \,\mathrm{d}x}{\|\widehat{w}^p\|_{L^2(\hat{\gamma})}} &\geq \sup_{\widehat{w}^p \in S_0^p} C \frac{\int_{\widehat{\gamma}} \widehat{g}^{p-1}\, \partial_x \widehat{w}^p \,\mathrm{d}x}{\|\partial_x \widehat{w}^p\|_{Z'}} \\ &= \sup_{\widehat{f}^{p-1} \in S^{p-1}_{\mathrm{zmv}}} C \frac{\int_{\widehat{\gamma}} \widehat{f}^{p-1}\, \widehat{g}^{p-1} \,\mathrm{d}x}{\|\widehat{f}^{p-1}\|_{Z'}}.\end{aligned}$$

Now, we make use of the $Z' - Z$ stability on the equal order pairing, as stated in Lemma 13. Since $\partial_x \widehat{g}^{p-1} = \widehat{\phi}^{p-2}$, we have

$$\sup_{\widehat{f}^{p-1} \in S^{p-1}_{\mathrm{zmv}}} C \frac{\int_{\widehat{\gamma}} \widehat{f}^{p-1}\, \widehat{g}^{p-1} \,\mathrm{d}x}{\|\widehat{f}^{p-1}\|_{Z'}} \geq C \|\widehat{g}^{p-1}\|_Z \geq C \left|\widehat{g}^{p-1}\right|_Z = C \|\widehat{\phi}^{p-2}\|_{L^2(\hat{\gamma})},$$

which yields the stated inf-sup condition.

The proof for the case $d = 3$ is analogue, but special care must be taken due to the tensor product structure. In this case, the suitable differential operator is the mixed derivative ∂_{xy}, so the partial integration has to be performed twice. Since most parts of the proof were shown in the previous lemmas, proving the analogue partial integration formula is the only remaining part. Given $\widehat{f}^{p-2} \in S_0^{p-2}$, define $\widehat{g}^{p-1} \in S^{p-1}_{\mathrm{zmv}}$ such that $\partial_{xy} \widehat{g}^{p-1} = \widehat{\phi}^{p-2}$. We apply Gauß theorem twice and note that in both cases

the boundary term vanishes

$$\int_{\widehat{\gamma}} \widehat{g}^{p-1}\, \partial_i \widehat{w}^p \,\mathrm{d}x = \int_{\partial\widehat{\gamma}} \widehat{w}^p\, \widehat{g}^{p-1} n_i \,\mathrm{d}s - \int_{\widehat{\gamma}} \widehat{w}^p\, \partial_i \widehat{g}^{p-1} \,\mathrm{d}x,$$

where n_i is the i-th component of the outward unit normal on $\partial\widehat{\gamma}$, i.e., $n_i \in \{0, \pm 1\}$.

Using the zero trace of $w^p \in H_0^{1,1}(\widehat{\gamma})$, the first step

$$\begin{aligned}\int_{\widehat{\gamma}} \widehat{w}^p\, \widehat{\phi}^{p-2}\mathrm{d}x &= \int_{\widehat{\gamma}} \widehat{w}^p \partial_{xy} \widehat{g}^{p-1}\mathrm{d}x \\ &= -\int_{\widehat{\gamma}} \partial_x \widehat{w}^p\, \partial_y \widehat{g}^{p-1}\mathrm{d}x + \int_{\partial\widehat{\gamma}} \widehat{w}^p\, \partial_y \widehat{g}^{p-1} n_1 \mathrm{d}\sigma \\ &= -\int_{\widehat{\gamma}} \partial_x \widehat{w}^p\, \partial_y \widehat{g}^{p-1}\mathrm{d}x\end{aligned}$$

follows.

For the second step, we use that on the part of $\partial\widehat{\gamma}$ parallel to the x-axis, it holds $\partial_x \widehat{w}^p = 0$. On the orthogonal part (parallel to the y-axis), it holds $n_2 = 0$.

$$\begin{aligned}-\int_{\widehat{\gamma}} \partial_x \widehat{w}^p\, \partial_y \widehat{g}^{p-1}\mathrm{d}x &= \int_{\widehat{\gamma}} \partial_{xy} \widehat{w}^p\, \widehat{g}^{p-1}\mathrm{d}x - \int_{\partial\widehat{\gamma}} \partial_x \widehat{w}^p\, \widehat{g}^{p-1} n_2 \mathrm{d}\sigma \\ &= \int_{\widehat{\gamma}} \partial_{xy} \widehat{w}^p\, \widehat{g}^{p-1}\mathrm{d}x.\end{aligned}$$

We define $\widehat{f}^{p-1} = \partial_{xy}\widehat{w}^p \in S^{p-1}_{\mathrm{zmv}}$ and continue analogously to the univariate case. Note, that this proof is not restricted to the bivariate case, but can be applied to tensor products of arbitrary dimensions. □

While we considered an inf-sup condition in the parametric space (2.2), the inf-sup condition, Assumption 6, needs to be fulfilled in the physical domain. Now we prove from Theroem 14 the inf-sup stability in the physical space.

Theorem 15. *Let (2.2) holds and let* $M_h^2 = \{\phi = \widehat{\phi} \circ \mathbf{F}_s^{-1}, \widehat{\phi} \in S^{p-2}(\widehat{\gamma})\}$, *and* $W_h = \{w = ((\widehat{w}/\widehat{DW}) \circ \mathbf{F}_s^{-1}), \widehat{w} \in S_0^p(\widehat{\gamma})\}$ *be respectively the Lagrange multiplier space and the primal trace space given in the physical domain. Then, for* h *sufficiently small, the pairing* $W_h - M_h^2$ *fulfills a uniform inf-sup condition, i.e.,*

for each $\phi \in M_h^2$, it holds

$$\sup_{w \in W_h} \frac{\int_\gamma \phi\, w \,\mathrm{d}s}{\|w\|_{L^2(\gamma)}} \geq C \|\phi\|_{L^2(\gamma)}.$$

Proof. After a change of variable, the integral over the physical boundary can be expressed as a weighted integral over the parametric one. The proof is based on a super-approximation of the product of the dual variable with the weight. In contrast to the previous proofs, we do not need to distinguish between the cases $d = 2$ and 3.

We recall the transformation of the integral onto the parametric space (2.1)

$$\int_\gamma \phi\, w \,\mathrm{d}s = \int_{\widehat{\gamma}} \widehat{\phi}\, \widehat{w}\, \rho \,\mathrm{d}x,$$

where $\rho = (\widehat{DW})^{-1} \, |\det \nabla_\gamma \mathbf{F}_s|$ is uniformly bounded by above and below and is h-independent. We also note the norm equivalence

$$C^{-1} \|\widehat{v}\|_{L^2(\hat{\gamma})} \leq \|\rho \widehat{v}\|_{L^2(\hat{\gamma})} \leq C \|\widehat{v}\|_{L^2(\hat{\gamma})}. \tag{2.4}$$

Let $\Pi : L^2(\widehat{\gamma}) \to S^{p-2}(\widehat{\gamma})$ denote any local projection with best approximation properties, e.g., [5, Equation 37]. The integration weight ρ is smooth except at the mesh lines, where it is only C^{p-m-1} for a breakpoint of multiplicity m and hence the following super-approximation holds

$$\|\widehat{\phi}\rho - \Pi(\widehat{\phi}\rho)\|_{L^2(\hat{\gamma})} \leq Ch \|\widehat{\phi}\|_{L^2(\hat{\gamma})}. \tag{2.5}$$

The proof of the super-approximation given in [110, Theorem 2.3.1] can be easily extended to the isogeometric setting using the standard approximation results for splines, see [5].

Then, for $\phi = \widehat{\phi} \circ \mathbf{F}_s^{-1}$, we choose $\widehat{w}_{\hat{\phi}\rho} \in S_0^p(\widehat{\gamma})$, such that

$$\frac{\int_{\widehat{\gamma}} \widehat{w}_{\hat{\phi}\rho} \Pi(\widehat{\phi}\rho) \,\mathrm{d}x}{\|\widehat{w}_{\hat{\phi}\rho}\|_{L^2(\gamma)}} \geq C \|\Pi(\widehat{\phi}\rho)\|_{L^2(\hat{\gamma})}.$$

We replace in the inf-sup integral the term $\widehat{\phi}\rho$ by its projection, use the super-approximation and the norm equivalence (2.4) to obtain:

$$\begin{aligned}\sup_{w\in W_h}\frac{\int_\gamma \phi\, w\,\mathrm{d}x}{\|w\|_{L^2(\gamma)}} &\geq C\sup_{\widehat{w}\in S_0^p(\hat{\gamma})}\frac{\int_{\hat{\gamma}}\widehat{w}\,\widehat{\phi}\rho\,\mathrm{d}x}{\|\widehat{w}\|_{L^2(\hat{\gamma})}}\\ &= C\,\frac{\int_{\hat{\gamma}}\widehat{w}_{\hat{\phi}\rho}\,\Pi(\widehat{\phi}\rho)\,\mathrm{d}x}{\|\widehat{w}_{\hat{\phi}\rho}\|_{L^2(\hat{\gamma})}}+C\frac{\int_{\hat{\gamma}}\widehat{w}_{\hat{\phi}\rho}(\widehat{\phi}\rho-\Pi(\widehat{\phi}\rho))\,\mathrm{d}x}{\|\widehat{w}_{\hat{\phi}\rho}\|_{L^2(\hat{\gamma})}}\\ &\geq C\|\Pi(\widehat{\phi}\rho)\|_{L^2(\hat{\gamma})}-C\|\widehat{\phi}\rho-\Pi(\widehat{\phi}\rho)\|_{L^2(\hat{\gamma})}\\ &\geq C\|\Pi(\widehat{\phi}\rho)\|_{L^2(\hat{\gamma})}-C'h\|\widehat{\phi}\rho\|_{L^2(\hat{\gamma})}.\end{aligned}$$

Now, we use the approximation result (2.5) and the norm equivalence (2.4) to bound $\|\Pi(\widehat{\phi}\rho)\|_{L^2(\hat{\gamma})}$:

$$\|\widehat{\phi}\|_{L^2(\hat{\gamma})}\leq\|\Pi(\widehat{\phi}\rho)\|_{L^2(\hat{\gamma})}+\|\Pi(\widehat{\phi}\rho)-\widehat{\phi}\rho\|_{L^2(\hat{\gamma})}\leq\|\Pi(\widehat{\phi}\rho)\|_{L^2(\hat{\gamma})}+C''h\|\widehat{\phi}\|_{L^2(\hat{\gamma})},$$

which shows $\|\Pi(\widehat{\phi}\rho)\|_{L^2(\hat{\gamma})}\geq C\|\widehat{\phi}\|_{L^2(\hat{\gamma})}$ for sufficiently small h. Then standard norm equivalences show the inf-sup condition in the physical domain. □

Remark 16. *An analogue proof shows the stability of a pairing of order p and $p-2k\geq 0$ for $k\in\mathbb{N}$. However, for $k>1$ the dual approximation order in the L^2 norm $p-2k$ is very low and will reduce the convergence order drastically, i.e., to $p-2k+3/2$. Since for Signorini and contact problems, the regularity of the solution is usually bounded by $H^{5/2-\varepsilon}(\Omega)$, see, e.g., [89], low dual degrees might be reasonably used in these cases.*

2.3.3 Choice 3: stable p/p pairing with boundary modification

The first two choices had been motivated by Assumptions 6 and 7. While the choice 1 does not yield uniformly stable pairings, the choice 2 does not guarantee optimal order p convergence. Thus let us consider the natural equal order pairing in more details. In the finite element context, it is well-known that the simple choice of taking the space of Lagrange multiplier as the space of traces from the slave side yields to troubles at the so-called cross points for $d=2$ and wirebaskets for $d=3$, i.e., $(\bigcup_{l\neq j}\partial\gamma_l\cap\partial\gamma_j)\cup(\bigcup_l\partial\gamma_l\cap\partial\Omega_D)$. As a remedy, in the finite element method a modification is performed, see [10, 111]. We adapt this strategy to isogeometric analysis, thus a modification of the dual spaces is performed to

ensure at the same time accuracy, see Assumption 7, and stability, see Assumption 6. This modification results in a reduction of dimension of the dual space such that a counting argument for the dimensions still holds. Roughly speaking there are two possibilities: in the first case, the mesh for the Lagrange multiplier is coarsened locally in the neighborhood of the cross point (resp. wirebasket), and in the second case the degree is reduced in the neighborhood of the cross point (resp. wirebasket). Here we only consider the second possibility.

Let us start the construction for the univariate case ($d = 2$), since the construction for the bivariate case ($d = 3$) can be done as a tensor product. Given an open knot vector and the corresponding B-Spline functions $\widehat{B}_i^p$. We define the modified basis $\widetilde{B}_i^p$, $i = 2, \ldots, n-1$ as follows

$$\widetilde{B}_i^p(\zeta) = \begin{cases} \widehat{B}_i^p(\zeta) + \alpha_i \widehat{B}_1^p(\zeta), & i \in \{2, \ldots, p+1\}, \\ \widehat{B}_i^p(\zeta), & i \in \{p+2, \ldots, n-p-1\}, \\ \widehat{B}_i^p(\zeta) + \beta_i \widehat{B}_n^p(\zeta), & i \in \{n-p, n-1\}. \end{cases}$$

The coefficients α_i and β_i are chosen such that the basis function is a piecewise polynomial of degree $p-1$ on the corresponding element while retaining the inter-element continuity on $\widehat{\gamma}$, i.e., as

$$\begin{aligned} \alpha_i &= -\widehat{B}_i^{p\,(p)}(\zeta)/\widehat{B}_1^{p\,(p)}(\zeta), \quad \zeta \in (0, \zeta_2), \\ \beta_i &= -\widehat{B}_i^{p\,(p)}(\zeta)/\widehat{B}_n^{p\,(p)}(\zeta), \quad \zeta \in (\zeta_{E-1}, 1). \end{aligned}$$

An example for degree $p = 3$ is shown in Figure 2.3. Note that $\widehat{B}_i^p$ is a polynomial of degree p on one single element, so the coefficients are well-defined and constant. Since derivatives of B-Spline functions are a combination of lower order B-Spline functions, a recursive algorithm for the evaluation exists, see [31, Section 2.1.2.2]. Using the recursive formula it can easily be seen that the coefficients are uniformly bounded under the assumption of quasi-uniform meshes. We define the space of Lagrange multipliers of the same order as the primal basis, as $\widehat{M}_h^0 = \operatorname{span}_{2,\ldots,n-1}\{\widetilde{B}_i^p\}$. The construction guarantees that the resulting basis forms a partition of unity.

Theorem 17. *Assumption 7 holds for the dual space $\widehat{M}_h^0$.*

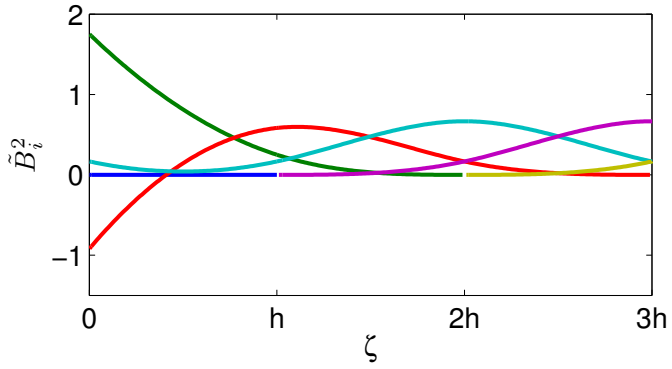

Figure 2.3: Boundary modification of a spline of degree 3 for $d = 2$, left modification.

Proof. Since the space of global polynomials of degree $p-1$ is contained in the dual space $\widehat{M}_h^0$, we can directly argue as in [5, Section 3]. □

2.3.4 Summary of the three considered trace spaces

Finally hereafter, we summarize the results for the three pairings considered:

- the pairing $p/p-1$ satisfies the necessary convergence order p in the L^2 norm, Assumption 7, but it does not fulfill Assumption 6. As a result, Theorem 8 cannot be applied and no optimal convergence can be expected.
- the pairing $p/p-2$ fulfills Assumption 6 and Assumption 7, hence this choice yields an order $p-1/2$ convergence by Theorem 8.
- the pairing p/p cannot satisfy Assumption 6 without a cross point modification. We propose a modification based on a local degree reduction at the boundary of the interface and show the uniform inf-sup stability numerically. And obviously it ensures Assumption 7, hence Theorem 8 guarantees an optimal convergence order p.

2.3.5 An alternative choice: a biorthogonal space as dual space

An alternative concept to the previously considered trace spaces are biorthogonal basis functions. Hereafter, we briefly discuss their constructions, but note that due to possible difficulties concerning the approximation order, this approach is not considered in the following.

A Lagrange multiplier basis $\{\psi_i\}_{i=1}^n$ is called biorthonormal, if it fulfills

$$\int_{\widehat{\gamma}} \widehat{B}_i^p(x)\psi_j(x)\mathrm{d}x = \delta_{ij} \int_{\widehat{\gamma}} \widehat{B}_i^p(x)\mathrm{d}x.$$

Of special interest, are biorthogonal basis functions which span on each element the same space as the primal basis and fulfill $\operatorname{supp} \widehat{B}_i^p = \operatorname{supp} \psi_i, i = 1, \ldots, n$. The construction of such a biorthogonal basis is easily possible by an inversion of a mass matrix on each element, see Figure 2.4 for a primal quadratic basis function and its corresponding biorthogonal basis function.

The inf-sup condition stated in Assumption 6 is easily fulfilled, see [70, Remark 2.11], but the critical requirement is the approximation property stated in Assumption 7. As for the high order finite element case, this property is not easy to obtain. Indeed, in a finite element context, it has been shown that the optimal approximation order can only be achieved by a suitable change of the primal basis, see [71]. However, the situation is different if we do not require the condition $\operatorname{supp} \widehat{B}_i^p = \operatorname{supp} \psi_i$. In [91] for high order finite elements, the existence of biorthogonal basis functions with a local support and optimal approximation properties has been shown. The algorithm proposed in [91] to build a biorthogonal basis can be tailored to B-Splines, see an example in Figure 2.4. We highlight that the support of each biorthogonal basis function consists of no more than $2p + 1$ elements, i.e., although the support enlarges it still remains local. Due to the complicated construction and the enlarged support, we do not follow this approach any further, but we note that biorthogonal bases are particularly popular for contact problems, see, e.g., [114].

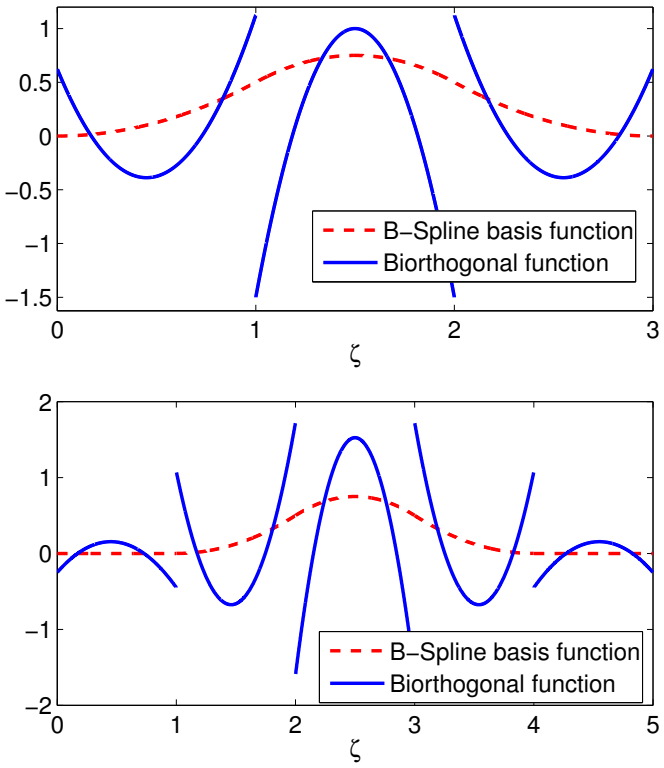

Figure 2.4: A quadratic basis function and its corresponding biorthogonal basis function (rescaled) on a uniform mesh. Top: Biorthogonal function with the same support as the primal basis. Bottom: Biorthogonal function with a local support and optimal approximation properties.

2.4 Numerical results

In this section, we apply the proposed mortar method to six examples, in order to validate its optimality and enlighten some additional practical aspects. All our numerical results were obtained on a Matlab code, using GeoPDEs, [34, 109]. Previous to the examples, we numerically evaluate the inf-sup constant for the considered pairings, and also for further choices. The first example is a multi-patch NURBS geometry with a curved interface, for which the computed L^2 and broken V rates are optimal. The second example is a re-entrant corner, where we investigate whether the presence of a singularity disturbs the proposed mortar method. Since the results are as expected, it can be said that the singularity does not have a large influence on the proposed coupling. An interface problem with jumping coefficients is considered as a third example, since for these problems domain decomposition methods are very attractive. Although NURBS are

capable of exactly representing many geometries, it is not always possible to have a matching interface between subdomains. For this reason in the fourth example, we introduce an additional variational crime by a geometry approximation. It can be seen, that the proposed method is robust with respect to a non-matching interface. In the fifth example, the effect on the Lagrange multiplier of an unstable pairing is considered. The last example is a problem of linear elasticity and it is shown that the mortar method behaves as well as for scalar problems. We note that in all of these examples the mortar integrals are evaluated in an optimal way. It is achieved by the use of specific geometry parametrizations that allow to build the merged mesh in the slave parametric space, and thus without any difficulty.

2.4.1 A numerical evaluation of the inf-sup condition

We consider one subdomain Ω_k resulting from the identity mapping of the unit square and assume that its mesh is uniformly refined. We identify elements in $M_{l,h}$ and $W_{l,h}$ with their algebraic vector representations. Then the inf-sup condition on one interface γ_l reads

$$\inf_{\lambda\in\mathbb{R}^{n'}} \sup_{v\in\mathbb{R}^{n}} \frac{\lambda^\top G\, v}{\left(\lambda^\top S\lambda\right)^{1/2}\left(v^\top T v\right)^{1/2}} \geq C > 0, \tag{2.6}$$

where $n' = \dim M_{l,h}$ and $n = \dim W_{l,h}$ and G, S, T denote the L^2 inner product matrices. Here we use the technique of Chapelle and Bathe, [24], to verify our theoretical results on the inf-sup stability. The proof of this approach can be found in [13, Chapter 3].

The h-dependency of the inf-sup condition was studied first for primal spaces without any Dirichlet boundary condition and with homogeneous conditions. Precisely, primal spaces are either $\{v_{|\gamma_l}, v \in V_{S(l),h}\}$ or $\{v_{|\gamma_l}, v \in V_{S(l),h}\} \cap H^1_0(\gamma_l) = W_{l,h}$, and dual spaces are $\{\lambda = \widehat{\lambda} \circ \mathbf{F}^{-1}_{S(l)}, \widehat{\lambda} \in \widehat{S}^p\}$ or $\left\{\lambda = \widehat{\lambda} \circ \mathbf{F}^{-1}_{S(l)}, \widehat{\lambda} \in \operatorname{span}_{2,\dots,n-1}\{\widetilde{B}^p_i\}\right\}$ for same degree pairings as it is necessary to consider a boundary modification.

This study leads us to the following conclusion: the inf-sup condition is satisfied for couples of the same parity, see Figure 2.5 for the pairings of primal degree $p = 5$. Moreover regarding the p-dependence, a reasonable behavior has been observed for primal space without boundary condition, whereas an exponential behavior has been found for primal space

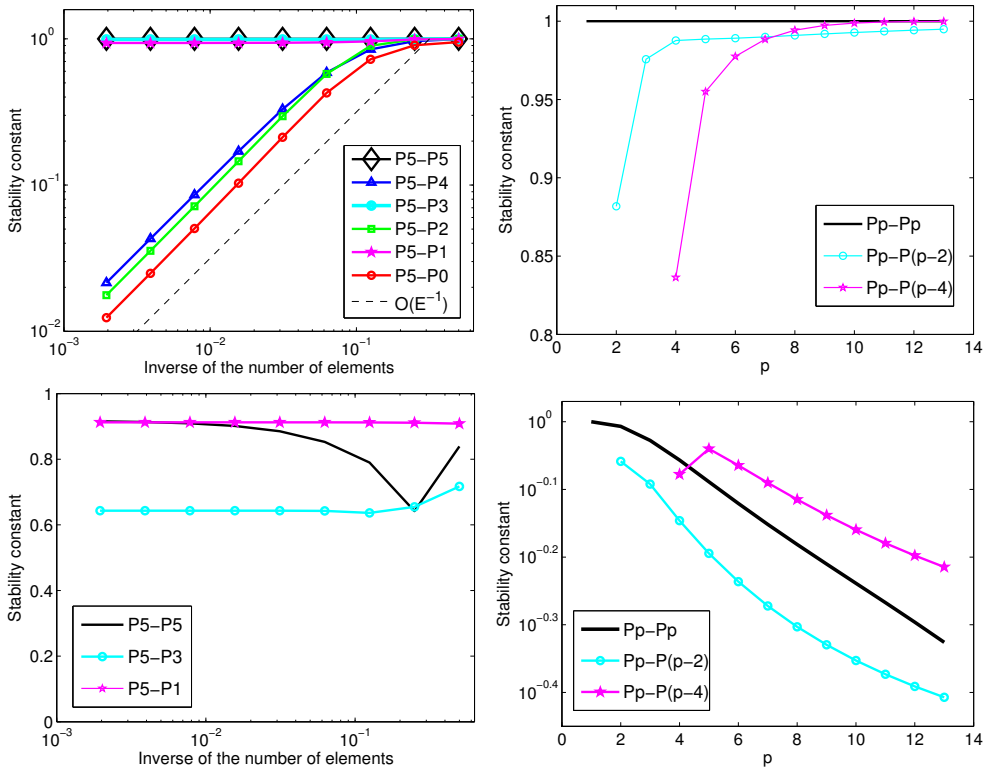

Figure 2.5: Problem of Subsection 2.4.1 - Left: h-dependency for pairing $P5/Pp$ $(p = 0, \ldots, 5)$. Right: p-dependency. Top: primal spaces without boundary condition. Bottom: primal spaces with homogeneous boundary conditions.

with boundary conditions, see Figure 2.5.

Comparing the three stable pairings of the top right picture of Figure 2.5, we note that although the dual space dimension decreases, the stability constant gets smaller with a lower dual degree. Once more, this shows that the inf-sup condition is not only a matter of dimensions of the spaces, especially for splines for which the spaces of different degrees are not nested in general. We also note that, considering homogeneous Dirichlet conditions, the stability constant for the case $P5/P3$ is less than for the other cases. However, the difference is quite small and should not lead to any remarkable effect.

2.4.2 A scalar problem on a multi-patch NURBS domain

Let us consider the standard Poisson equation $-\Delta u = f$, solved on the domain $\Omega = \{(r, \varphi),\, 0.2 < r < 2,\, 0 < \varphi < \pi/2\}$ which is given in polar coordinates. The domain is decomposed into two patches, which are presented in Figure 2.6. The internal load and the boundary conditions have been manufactured to have the solution $u(x, y) = \sin(\pi x)\sin(\pi y)$, given in Cartesian coordinates. To test the same degree pairings, we consider a case such that no boundary modification is required. This can be granted by setting Neumann boundary conditions on $\partial\Omega_N = \{(r, \varphi),\, 0.2 < r < 2,\, \varphi \in \{0, \pi/2\}\}$ and Dirichlet boundary conditions on $\partial\Omega \backslash \partial\Omega_N$.

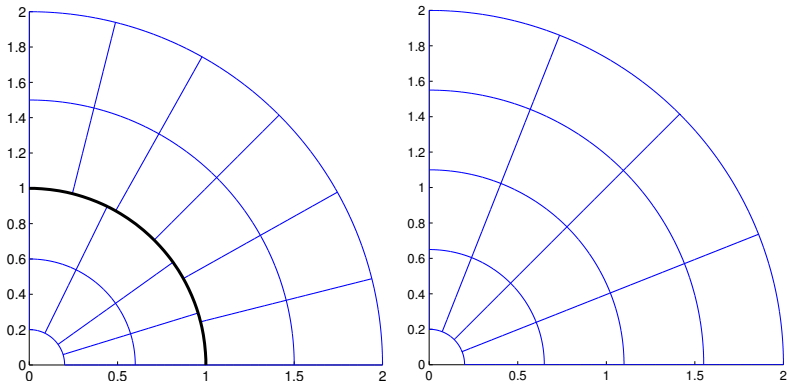

Figure 2.6: Problem of Subsection 2.4.2 - Left: a non-conforming mesh. Right: a conforming mesh.

In Figure 2.7, we show the numerically obtained error decay in the L^2 and the broken V norm for the primal variable and $p = 2, 3, 4$. As expected from the theory, for an equal order p pairing we observe a convergence order of $p + 1$ for the L^2 error. We also compare the error of a matching and

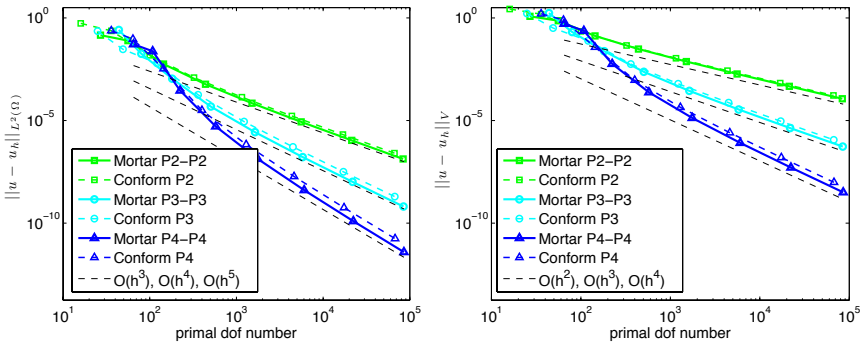

Figure 2.7: Problem of Subsection 2.4.2 - L^2 (left) and broken V (right) primal error curves for same degree pairings.

non-matching mesh situation and recall that in the matching case we are within the standard conforming setting. As Figure 2.7 shows, no significant quantitative difference can be observed. Note that the comparison is based on results issued from similar meshes not from similar control point repartition, see Figure 2.6. In Table 2.1, the numerically computed order of the L^2 error decay is given. Asymptotically, the optimal order of $p+1$ is obtained in each refinement step.

	$P2-P2$		$P3-P3$		$P4-P4$	
level	error value	slope	error value	slope	error value	slope
0	1.445757e-01		2.603045e-01		5.221614e-02	
1	7.871436e-02	0.877	1.799185e-02	3.855	2.373889e-02	1.137
2	5.651043e-03	3.800	1.100586e-03	4.031	2.897823e-04	6.356
3	5.904159e-04	3.259	4.794994e-05	4.521	5.162404e-06	5.811
4	7.021278e-05	3.072	2.719572e-06	4.140	1.361467e-07	5.245
5	8.663724e-06	3.019	1.661382e-07	4.033	4.059923e-09	5.068
6	1.079348e-06	3.005	1.033782e-08	4.006	1.253044e-10	5.018
7	1.347999e-07	3.001	6.458495e-10	4.001	3.902800e-12	5.005

Table 2.1: Problem of Subsection 2.4.2 - $||u - u_h||_{L^2(\Omega)}$ and its estimated order of convergence.

2.4.3 A singular scalar problem

Let us now consider the Laplace equation $-\Delta u = 0$, solved on a non-convex domain Ω with a re-entrant corner decomposed into three patches, presented in Figure 2.8. We need to precise for this example the mortar geometry setting. The patches are enumerated from 1 to 3 from the left to the right. We set the interface 1 as the interface between the subdomain 1 and 3, the interface 2 between 2 and 3 and the interface 3 between 1 and 2, see Figure 2.8. The singular function associated to a re-entrant corner

with Dirichlet condition is given by $r^{2/3}\sin(2/3\varphi)$, see [51]. We consider this singular case, which can be granted by setting all the boundary of Ω as a Dirichlet boundary with the value $r^{2/3}\sin(2/3\varphi)$.

The order of the numerical method is bounded by the singularity. Standard techniques to obtain better convergence rates include the use of graded meshes, [2], and hp-refinement, [101, 21]. Here we do not wish to improve these rates, but to test if the proposed mortar method is disturbed by the presence of a singularity.

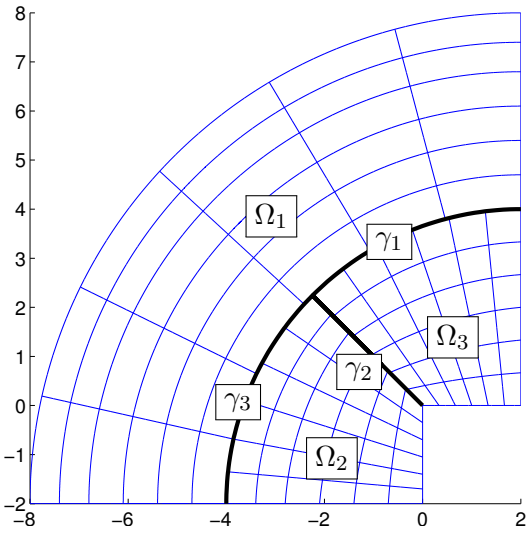

Figure 2.8: Problem of Subsection 2.4.3 - A non-conforming mesh.

The results are compared to the analytical solution and a numerical error study is provided. The errors are shown in Figures 2.9 and 2.10, the L^2 and broken V errors are considered for the primal solution and the L^2 error for the dual solution.

Considering the same degree pairing the boundary modification is necessary and the results show the optimality of the method with respect to the regularity of the solution, see Figure 2.9. We note an initial bad behavior of the L^2 dual error on interface 2. The increase in the error might be related to the fact, that the exact Lagrange multiplier of interface 2 is zero. More precisely, the convergence rate $1/6$ for the dual variable is a very slow rate, but induced by the regularity of the solution at this interface, as we can see that the rate on the remaining interfaces is better. Moreover, we have also

considered different degree pairings, and observed numerically the stability of the methods. In Figure 2.9, the results for the pairing $P4 - P2$ and $P3 - P1$ are given and show asymptotically the same convergence rates as best approximations.

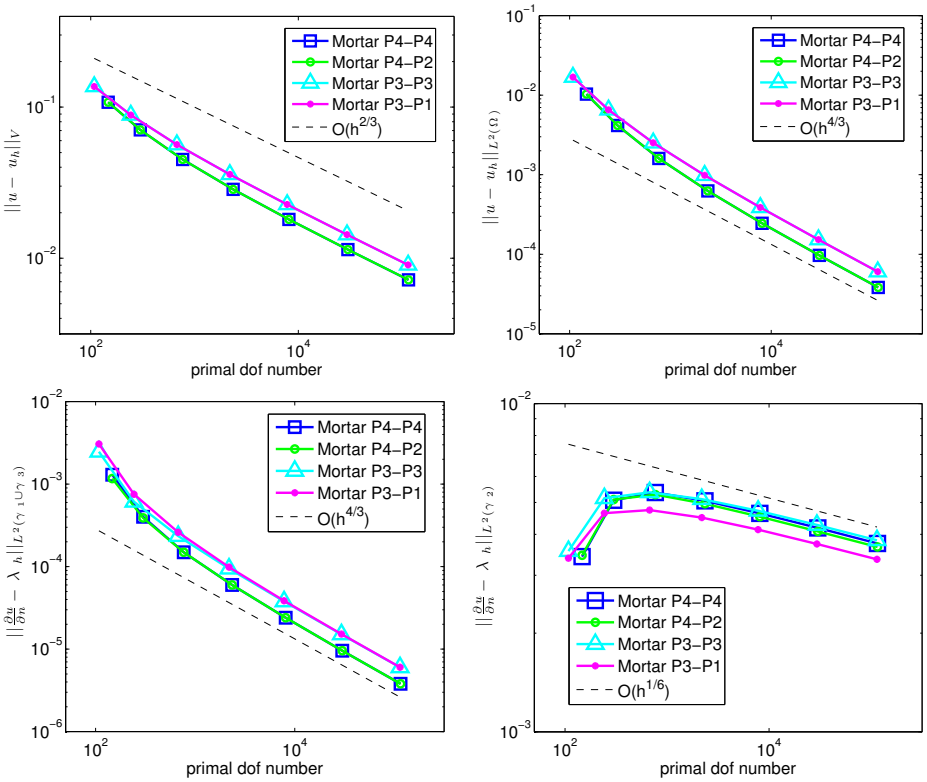

Figure 2.9: Problem of Subsection 2.4.3 - Error curves for several pairings. Top left: broken V primal error. Top right: L^2 primal error. Bottom left: L^2 dual error at the interfaces 1 and 3. Bottom right: L^2 dual error at interface 2.

We also studied the error distribution over the different subdomains and interfaces, see Figure 2.10. The results clearly show the pollution effect in the L^2 norm, i.e., also in the subdomain 1 far away from the singularity no better L^2 convergence rate can be observed. The situation is different if we consider the H^1 norm subdomain-wise. Here a better rate can be observed for subdomain 1 although it is significantly smaller than the best approximation rate restricted to this subdomain. This effect can be explained by local Wahlbin type error considerations in combination with the already mentioned pollution effect. Regarding the dual error, the same behavior as for the H^1 primal error is observed. A discrepancy between the interface 2 and the remaining interfaces can also be seen in the L^2 primal trace error.

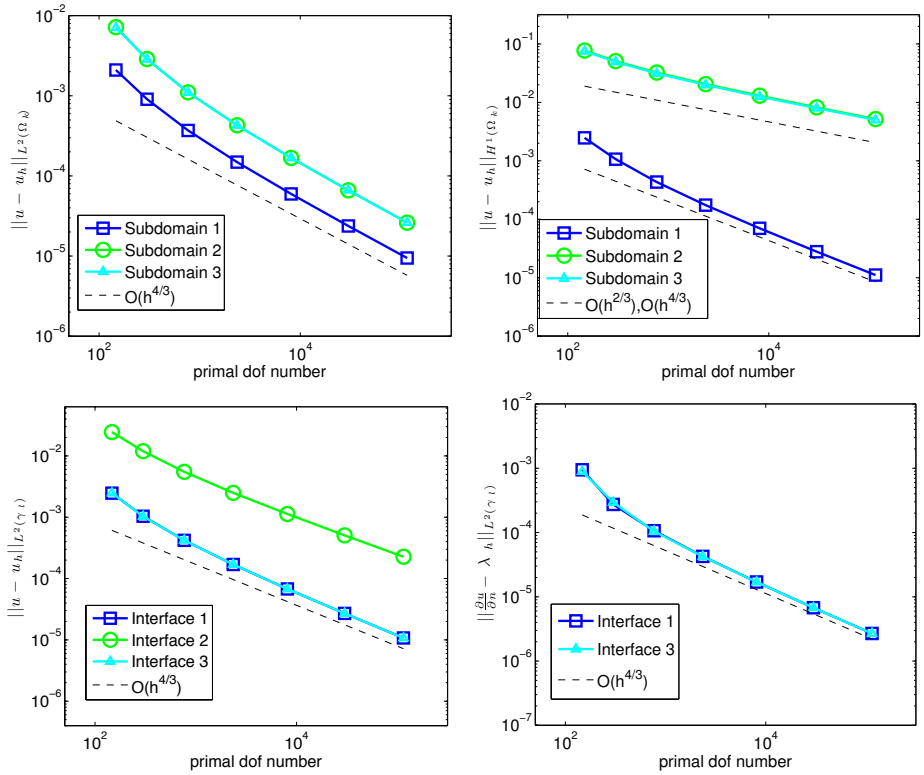

Figure 2.10: Problem of Subsection 2.4.3 - Error curves for the pairing $P4-P4$. Top left: L^2 error on each subdomain. Top right: H^1 error on each subdomain. Bottom left: L^2 primal trace error at each interface. Bottom right: L^2 dual error at interface 1 and 3.

2.4.4 A scalar problem with jumping coefficients

We consider the domain $\Omega = (0,2) \times (0,2.8)$ with homogeneous Dirichlet conditions applied on $\partial\Omega_D = (0,2) \times \{0, 2.8\}$ and homogeneous Neumann conditions on $\partial\Omega_N = \partial\Omega \backslash \partial\Omega_D$.

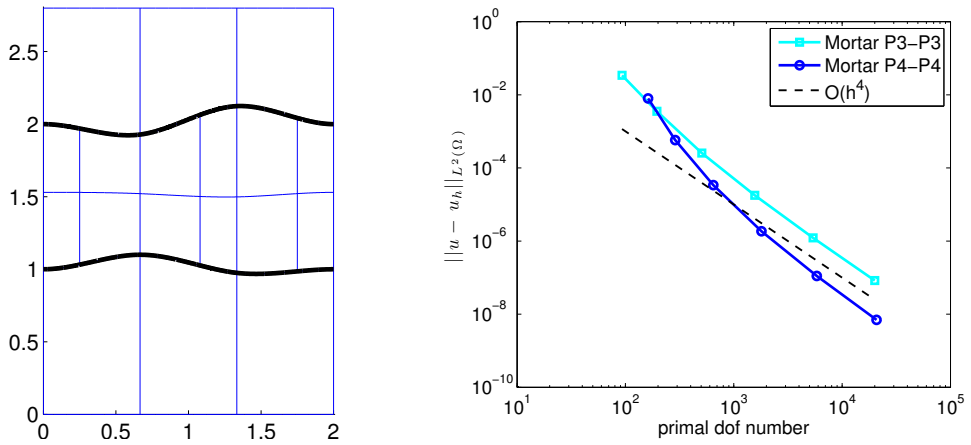

Figure 2.11: Problem of Subsection 2.4.4 - Left: initial mesh. Right: primal L^2 error curves for two equal order pairings.

We consider three patches, see a distribution in Figure 2.11, with α being constant on each patch, see Equation (1.1). The interface is a B-Spline curve of degree 3 and exactly represented on the initial mesh. The external layers have the constant $\alpha = 1$, and the internal one $\alpha = 1/100$ and the right hand side is $f = 1$. Due to the different values of α, the mesh of the interior layer is chosen finer compared to the one of the other two layers. A uniform refinement starting from the initial mesh in Figure 2.11 is performed.

In Figure 2.11 the L^2 primal error of an equal degree pairing for $p = 3$ and $p = 4$ is shown. Lacking an exact solution, we compute the error by comparing to a reference solution, visible in Figure 2.12. The reference solution is obtained by two more h-refinement steps starting from the finest mesh.

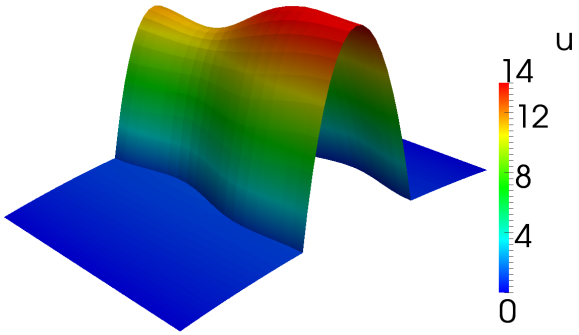

Figure 2.12: Problem of Subsection 2.4.4 - Solution for the pairing $P3 - P3$ on the finest mesh.

We note that jumping coefficients can cause singularities in the case where more than two subdomains meet, although it is well-known that the case of a rectangular subdomains with interfaces parallel to the x-axis yields to a smooth solution.

Numerically, we obtain optimal convergence for the case $p = 3$, but considering the convergence rate, there is no benefit of the degree elevation to degree $p = 4$, which indicates that the solution is not sufficiently smooth. Further numerical investigations let us conjecture that this can have two reasons, one coming from the fact that the interface is not smooth enough to have higher regularity. In this example the interface was built from a B-Spline curve of degree $p = 3$, hence the continuity on the interface is only C^2. This has an influence on the smoothness of the unit normal along the interface and thus on the smoothness of the solution. The other reason is to

have corner singularities in the inner subdomain where interface meets the outer boundary. We note that in this example, the angles were set to be $\pi/2$.

2.4.5 A scalar problem on a two patch domain with a non-matching interface

Let us consider the standard Poisson equation solved on the unit square $\Omega = (0,1)^2$, which is decomposed into two patches presented in Figure 2.13. As the subdomains cannot exactly be represented by the chosen spline spaces for the geometry approximation, the subdomains do not match at the interface, see Figure 2.13. And thus, due to this geometry approximation an additional variational crime is introduced in the weak problem formulation.

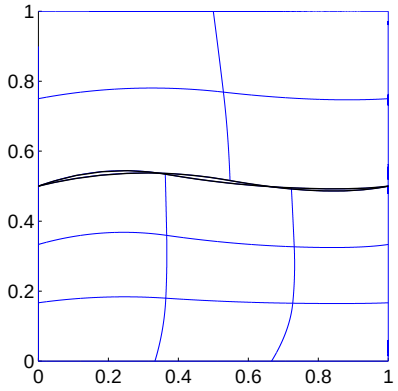

Figure 2.13: Problem of Subsection 2.4.5 - Non-conforming mesh with a non-matching interface.

The internal load and the boundary conditions have been manufactured to have the analytical solution $u(x,y) = \sin(5y)\sin(6x)$. Firstly, to measure the influence of the geometrical approximation on the mortar method accuracy, we consider the same degree pairing and note that in this case no boundary modification is required. This is granted by setting homogeneous Neumann conditions on $\partial\Omega_N = \{0,1\} \times (0,1)$ and Dirichlet conditions on $\partial\Omega \backslash \partial\Omega_N$. In Figure 2.14, we show the numerically obtained error decay in the L^2 norms. We observe for an equal order p pairing a convergence order of $p+1$ for the primal variable, which is the same order as we could theoretically expect with an exact geometry. Note that these optimal L^2 rates are in accordance with the theory of finite element methods, see [76]. We

also compare the primal error of a matching and non-matching mesh situation. As Figure 2.14 shows, no significant quantitative difference can be observed in the asymptotical behavior. Moreover, the results of the bottom right picture of Figure 2.14 show even higher rates for the dual variable than expected from the theory.

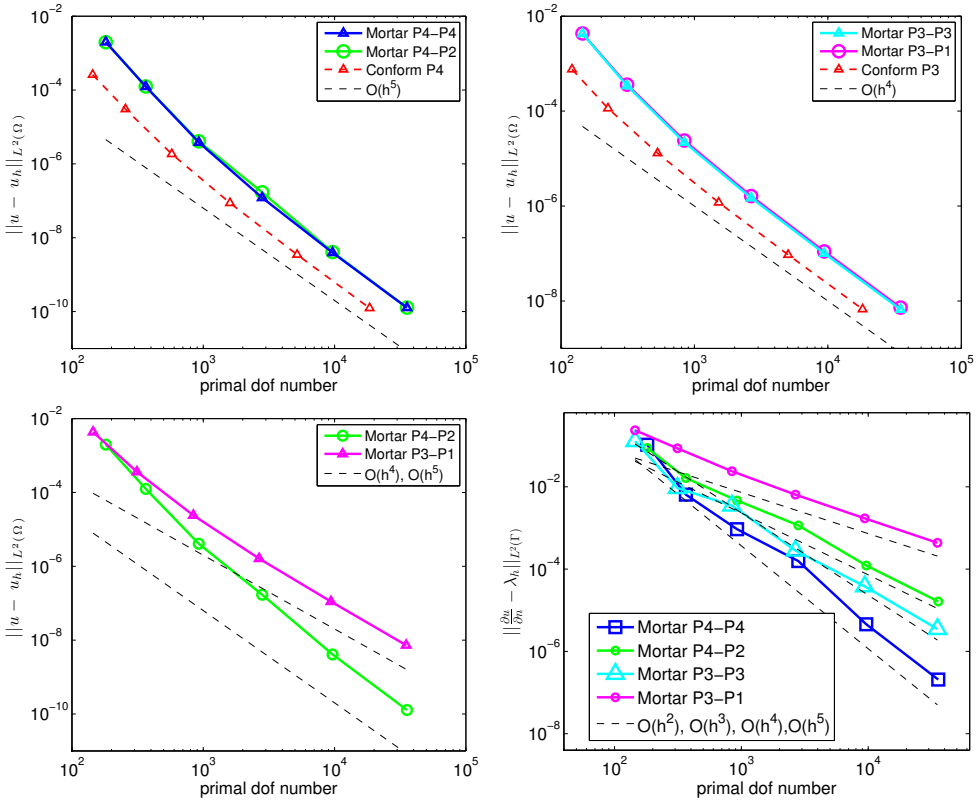

Figure 2.14: Problem of Subsection 2.4.5 - Several L^2 error curves. Top left: primal error for stable pairings of primal degree $p = 4$. Top right: primal error for stable pairings of primal degree $p = 3$. Bottom left: direct comparison of the primal error for pairings $P4 - P2$ and $P3 - P1$. Bottom right: dual error for stable pairings of primal degree $p = 3$ and $p = 4$.

Secondly, we consider different degree pairings in order to see the accuracy of the reduced order mortar method for a problem containing an additional approximation. In the bottom right picture of Figure 2.14, we note that a lower dual degree does not deteriorate the accuracy on the primal variable. From the theoretical point of view, it is obvious that a $p/p-2$ pairing gives a priori results for the Lagrange multiplier which are of the same order as the best approximation of the dual space. However, this is not the case for the primal variable. Theorem 8 indicates that for this case a $\sqrt{h}$ is lost. This is not observed in our situation. This might be a consequence of superconvergence arguments which can possibly recover an extra order of

$\sqrt{h}$ on uniformly refined meshes.

To conclude, this example shows that the influence of the additional geometry error in the mortar method context is quite small.

2.4.6 The influence of the unstable $p/p-1$ pairing

Let us now consider the $p/p-1$ pairing on a simple setting to illustrate the effects of the instability. We solve the Poisson equation on the unit square, decomposed into two patches by the interface $(0,1)\times\{1/2\}$. The internal load and the boundary conditions are applied such that the analytical solution is $u(x,y) = \left(\cos(x) + 16x^2(1-x)^2\right)\exp(y-1/2)$. On the boundary parallel to the interface, we apply Dirichlet conditions. On the remaining part, we compare two different cases: firstly Neumann conditions and secondly Dirichlet conditions (i.e., the problem is a pure Dirichlet problem).

Starting from a coarse initial mesh, we refine uniformly and focus on the Lagrange multiplier. In Figure 2.15, we show numerical results for the pairing $P2-P2$ and $P2-P1$, we note that this latter was observed to be unstable in Section 2.3.1, with an inf-sup constant of order $\mathcal{O}(h)$. Persistent spurious oscillations, induced by the lack of a uniform inf-sup stability, are clearly observed in the $P2-P1$ case. Furthermore, the oscillations are considerably stronger for the pure Dirichlet problem than for the Dirichlet-Neumann problem. We point out that the primal space in case of the pure Dirichlet problem is smaller than in the other case, while for the $P2-P1$ case the dual space is the same in both cases. This additionally reduces the inf-sup constant and yields larger spurious oscillations visible in the right pictures of Figure 2.15. In contrast, for the $P2-P2$ pairing the dual space is changing, indeed for the pure Dirichlet problem a cross point modification as introduced in Section 2.3.3 is applied, which preserves the uniform stability.

2.4.7 A linear elasticity problem

Let us first recall the mechanical equilibrium on a domain Ω as:

$$\begin{aligned} -\operatorname{div}(\underline{\sigma}) &= \boldsymbol{f} && \text{in } \Omega, \\ \boldsymbol{u} &= \boldsymbol{u_D} && \text{on } \partial\Omega_D, \\ \underline{\sigma}\cdot\boldsymbol{n} &= \boldsymbol{g} && \text{on } \partial\Omega_N. \end{aligned}$$

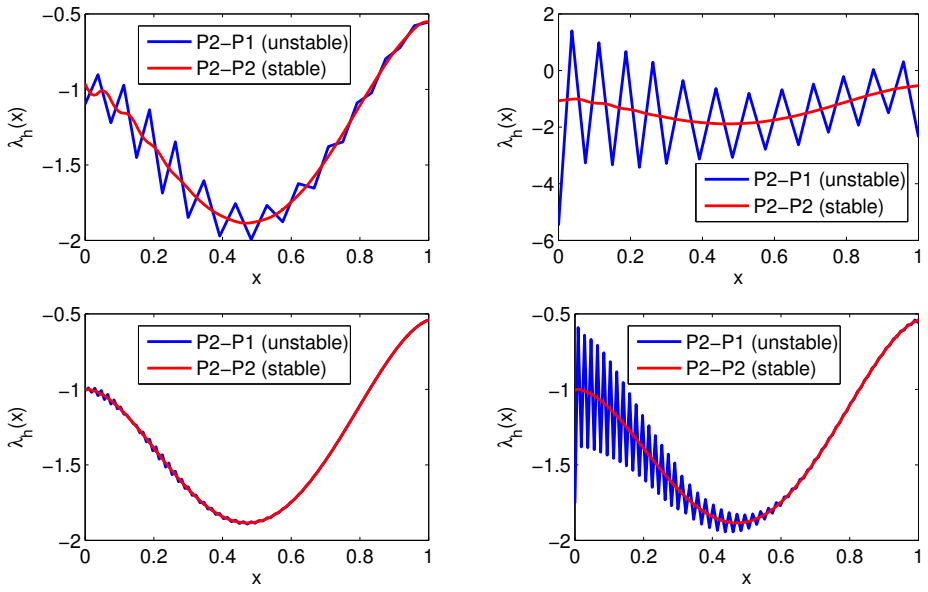

Figure 2.15: Problem of Subsection 2.4.6 - Discrete Lagrange multiplier. Left: Dirichlet-Neumann problem. Right: pure Dirichlet problem. Top: mesh level 3 ($h = 1/16$). Bottom: mesh level 5 ($h = 1/64$).

In a plane linear isotropic elastic context, we have the following relations between the stress tensor $\underline{\underline{\sigma}}$, the strain tensor $\underline{\underline{\varepsilon}}$ and the displacement $\boldsymbol{u}$:

$$\underline{\underline{\sigma}} = \lambda_{\text{Lamé}}\, tr(\underline{\underline{\varepsilon}})\, \underline{\underline{\mathbb{I}}} + 2\, \mu_{\text{Lamé}}\, \underline{\underline{\varepsilon}} \quad \text{and} \quad \underline{\underline{\varepsilon}} = \frac{1}{2}\left(\underline{\underline{\nabla \boldsymbol{u}}} + (\underline{\underline{\nabla \boldsymbol{u}}})^T\right) = \underline{\underline{\nabla^s \boldsymbol{u}}},$$

where $\mathbf{div}$, ∇ and ∇^s stand respectively for the standard divergence, gradient and symmetric gradient operators, $\lambda_{\text{Lamé},k}$ and $\mu_{\text{Lamé},k}$ for the Lamé coefficients, $\boldsymbol{n}$, $\boldsymbol{f}$, $\boldsymbol{u_D}$, $\boldsymbol{g}$ for the unit outward normal to Ω on $\partial\Omega$, the prescribed data values in Ω, on $\partial\Omega_D$ and on $\partial\Omega_N$.

Let us consider the equilibrium of a linear elastic isotropic infinite plate with a circular hole subjected to tension loading in $x = -\infty$ and $x = +\infty$.Considering the load and the boundary condition symmetries, only a quarter of the plate is modeled. This test, which has an analytical solution, [106], is a typical benchmark in isogeometric analysis because the NURBS offer the possibility to exactly represent the geometry. However, it cannot be parametrized smoothly in a one patch setting, so it is worthwhile to consider it within a domain decomposition approach such as the mortar method.

We consider a domain $\Omega = \{(x, y) \in (0, 2)^2 : x^2 + y^2 > 0.04\}$, shown in Figure 2.16, apply the exact pressure on $\partial\Omega_N = \{2\} \times (0.2, 2) \cup (0.2, 2) \times \{2\}$ and the symmetry condition on $\partial\Omega_{D_1} = \{0\} \times (0.2, 2)$ and $\partial\Omega_{D_2} = (0.2, 2) \times \{0\}$.

Let us consider three different parametrizations of this test, see Figure 2.16. Firstly, two geometrically conforming cases which are constituted by 2 and 4 patches, respectively. Only in the four patch situation, we have cross points where the boundary modification of the dual space is required. Secondly, let us consider a slave geometrical conforming case constituted by 3 patches for which the boundary modification is necessary considering the same degree pairing. In each case, the results are compared to the analytical solution. A numerical convergence study is presented in Figure 2.17 for a primal degree $p = 4$ and its corresponding stable reduced degrees.

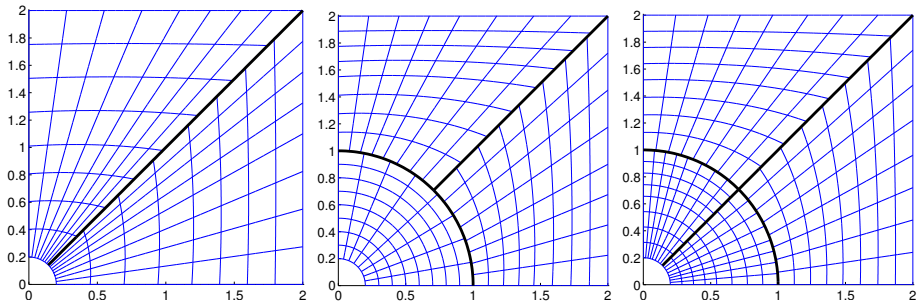

Figure 2.16: Problem of Subsection 2.4.7 - Different parametrizations of the infinite plate with a hole. From left to right: 2, 3 and 4 subdomains.

As it is visible in the left column of Figure 2.17 for the broken V error of the primal variable, the mortar methods remain optimal in all the cases. We note that even if we were expecting from the theory a reduced order regarding the convergence of the primal variable in broken V norm for the pairing $P4 - P2$, we numerically obtain for some parametrization a better order. Additionally as already observed several times, we obtain the best approximation rates for the L^2 error of the dual variable for the different degree pairings.

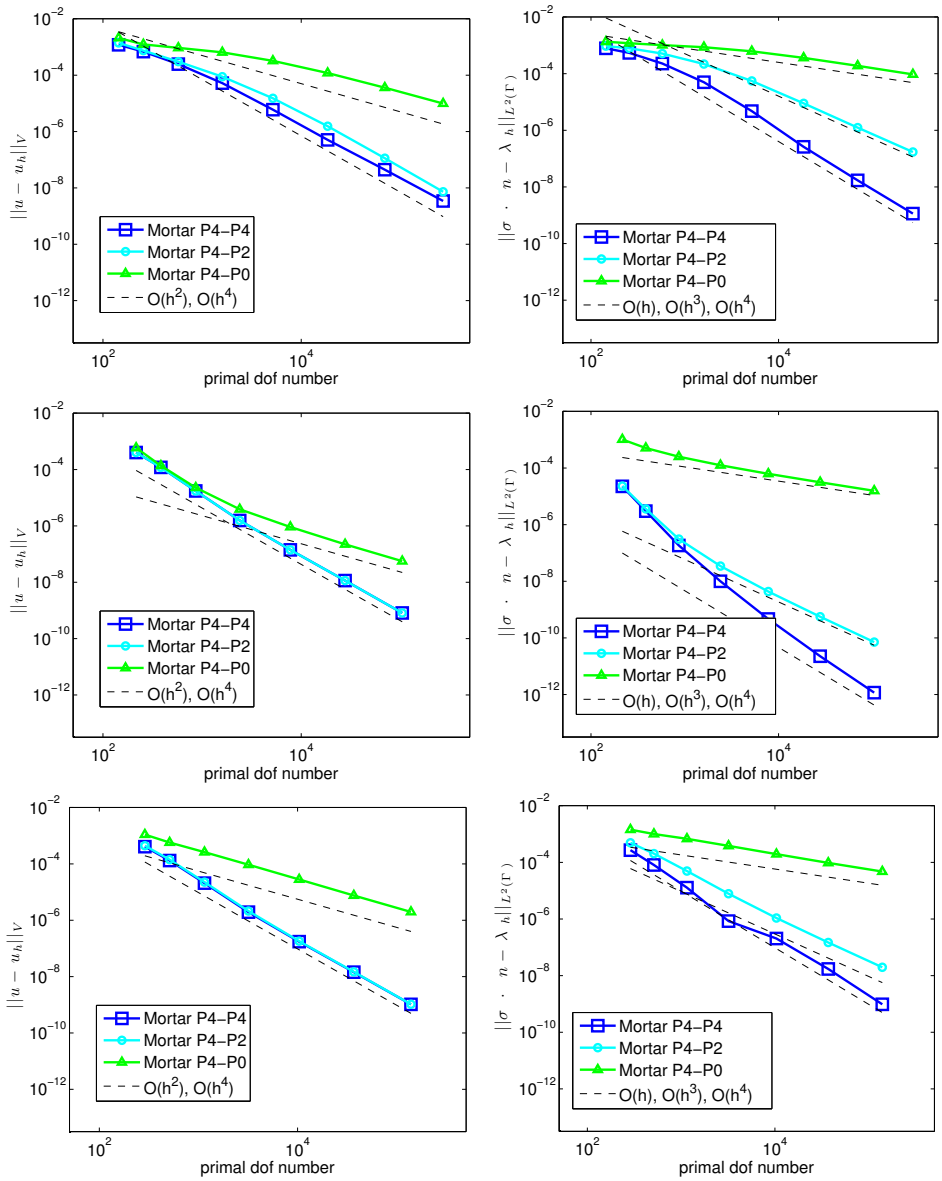

Figure 2.17: Problem of Subsection 2.4.7 - Left: broken V primal error curves. Right: L^2 dual error curves. Respectively from the top to the bottom, for the 2, 3 and 4 patch parametrizations given in Figure 2.16, for several degree pairings.

2.5 Conclusion

In this study an isogeometric mortar formulation was presented and investigated from a mathematical and a practical point of view. For a given primal order p, dual spaces of degree p, $p-1$ and $p-2$ were considered. While the pairing $p/p-1$ was proven unstable, the others satisfied this condition, noting that the stability is achieved for the same degree pairing because of a boundary modification. The proposed mortar methods are such that the

equal order pairing guarantees optimal results, while for the pairing $p/p-2$ the convergence order can be reduced by at most $1/2$. However, we note that a boundary modification always yields additional effort for the implementation and the data structure.

Numerical examples showed that mortar methods can also handle further difficulties arising from geometry approximations and is not perturbed by singularities. Also in several cases the obtained convergence order was superior to the theoretical results.

Chapter 3

Approximation of the mortar integrals

Contents

3.1 Introduction

Mortar methods have been shown to be well-suited for isogeometric analysis. In this chapter, we present the results of some studies on the impact that some approximations can do on isogeometric mortar methods.

The first one regards the use of approximate projections in the mortar formulation. The second one is focusing on the variational crime introduced by approximate quadrature formulae for the evaluation of the coupling integrals. It is a joined work with A. Buffa, B. Wohlmuth and L. Wunderlich which has been published in [18]. The third one is addressing the build of a merged mesh to integrate in an optimal way the mortar integrals. It is a collaboration work with A. Buffa, M. Martinelli, G. Elber and F. Massarwi.

The chapter is organised as follows. First, in Section 3.2, we present the considered projections and their relative modified mortar formulations. Secondly, in Section 3.3, we consider a review of numerical quadrature for mortar integrals as well as additional aspects specific to isogeometric analysis. And finally, in Section 3.4, we present a segmentation process for isogeometric analysis. All the sections are illustrated by numerical results.

3.2 Approximate projection

3.2.1 Approximate mortar formulations

In the bilinear form $b(v,\lambda)$ (and analogously $b(u,\phi)$) we split the mortar integral into two counterparts $\int_{\gamma_l} \lambda\ v^M \mathrm{d}s$ and $\int_{\gamma_l} \lambda\ v^S \mathrm{d}s$, where v^M denotes the trace of v from the master domain $\Omega_{M(l)}$, and v^S the trace of v from the slave domain $\Omega_{S(l)}$. To simplify the notation, let us restrict ourselves to the case of one single interface and drop the index l in the following.

Let us introduce the classical L^2-projection Π into $S^p(\boldsymbol{\Xi})$, i.e., the multiplier space defined as

$$\Pi : \mathbb{R} \to S^p(\boldsymbol{\Xi}), \quad \int_\gamma (\Pi u)\ \phi \,\mathrm{d}s = \int_\gamma u\, \phi \,\mathrm{d}s, \quad \phi \in S^p(\boldsymbol{\Xi}), \tag{3.1}$$

and a lumped L^2-projection $\widetilde{\Pi}$ into $S^p(\boldsymbol{\Xi})$ defined as

$$\widetilde{\Pi} : \mathbb{R} \to S^p(\boldsymbol{\Xi}), \quad (\widetilde{\Pi} u)_j = \frac{\int_\gamma u\, B_j^\phi \,\mathrm{d}s}{\int_\gamma B_j^\phi \,\mathrm{d}s}, \quad \forall\, j = 1, \dots, n_{M_h}. \tag{3.2}$$

This later projection is inducing an error compared to the L^2-projection due to the lumping of the multiplier mass matrix in the projection coefficient computation. We note that this error disappears in the case the multiplier

is taken as a piecewise constant, while it increases rising the multiplier approximation space degree. In the isogeometric analysis context, the error induced by the lumping of a mass matrix is of order 1. Thus, it pollutes in principle, the optimality of the method using polynomial degree higher than 1.

The discrete mortar formulation with the use of the L^2-projection of the displacement in the multiplier space is by construction equivalent to (1.3) in the one interface case. We emphasize that the equivalence remains valid only if suitable integral quadrature rules are used to evaluate the mortar integrals.

While the mortar method with the lumped L^2-projection of the displacement in the multiplier space reads as follows:
in a non-symmetric case, find $(u_h, \lambda_h) \in V_h \times M_h$, such that

$$\begin{aligned} a(u_h, v_h) + \int_\gamma (v_h^S - v_h^M)\ \lambda_h \,\mathrm{d}s = f(v_h), \quad v_h \in V_h, \\ \int_\gamma \widetilde{\Pi}(u_h^S - u_h^M)\ \phi_h \,\mathrm{d}s = 0, \quad \phi_h \in M_h, \end{aligned}$$

in a symmetric case, find $(u_h, \lambda_h) \in V_h \times M_h$, such that

$$\begin{aligned} a(u_h, v_h) + \int_\gamma \widetilde{\Pi}(v_h^S - v_h^M)\ \lambda_h \,\mathrm{d}s = f(v_h), \quad v_h \in V_h, \\ \int_\gamma \widetilde{\Pi}(u_h^S - u_h^M)\ \phi_h \,\mathrm{d}s = 0, \quad \phi_h \in M_h. \end{aligned}$$

In the next section, numerical results show that even though the symmetric formulation has some advantages from the computational point of view, it is leading to non optimal mortar methods. It is not observed with the non-symmetric formulation, as theoretically expected. Indeed by definition of the lumped L^2-projection, it is easy to see that:

$$b(v_h, \lambda_h) = 0, \quad \forall \lambda_h \in M_h \quad \text{if and only if} \quad b(\widetilde{\Pi}(v_h), \lambda_h) = 0, \quad \forall \lambda_h \in M_h.$$

3.2.2 Numerical results

In this subsection, we consider a two-dimensional setting in order to observe the effects of the approximate L^2-projection in the mortar formulation on the optimality of the mortar method.

Let us consider the Poisson problem $-\Delta u = f$ solved on the domain

$\Omega = (0,1) \times (-1,1)$ which is decomposed into two patches by the interface $\gamma = \{(x,y) \in \Omega,\ y = 0\}$, see Figure 3.1. The upper domain is set as the slave domain. The internal load and the boundary conditions are manufactured to have the analytical solution:

$$u(x,y) = \cos(\pi x)\left(\cos\left(\frac{\pi}{2}y\right) + \sin(2\pi y)\right), \text{ see Figure 3.1.}$$

The normal derivative on the interface is given by $\partial u/\partial \mathbf{n}(x) = 2\pi \cos(\pi x)$, see Figure 3.1. Neumann conditions are applied on the left and right boundary parts, i.e., such that no cross point modification is necessary.

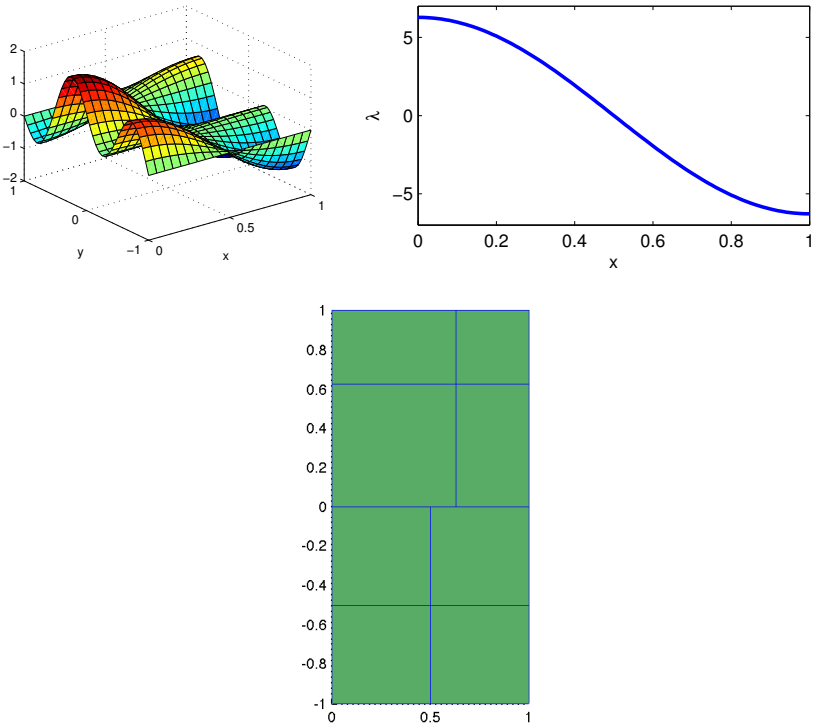

Figure 3.1: Top left: Primal solution on Ω. Top right: Lagrange multiplier along the interface. Bottom: Meshes at mesh refinement level 0.

Regarding the meshes, we consider a family of meshes obtained by uniform refinement of a initial mesh. It is such that at any refinement level, any parts of the slave and master boundary meshes do coincide and such that both meshes have same number of elements to measure only the perturbance due to the approximate projection. On Figure 3.1, the initial mesh situation is visible.

In the following, we provide different numerical error study results. In all cases, the primal L^2 and the dual L^2 errors are computed by a comparison with the analytical solution stated above. With the modified mortar formulations (symmetric and non-symmetric ones), no disturbance compared to the exact case has been observed on the primal variable in L^2 norm and thus for all the tested pairings, i.e., same degree and different degree pairings, see some results in Figure 3.2. On the contrary, some disturbances have been observed on the dual variable. More precisely, as visible in Figure 3.2, the non-symmetric version leads to results similar to the exact integration case while it is not the case for the symmetric version. It means that in this later case the way the lumped L^2-projection is inserted in the mortar formulation is creating a variational crime. This crime can be imputing to the use of approximate trial functions, functions on which the weak formulation is based. We point out that for both modified methods with the pairing $P2-P0$ the results are as the exact case as expected, see Figure 3.3. Indeed, in this special case, all the three formulations are equivalent by definition of the lumped L^2-projection.

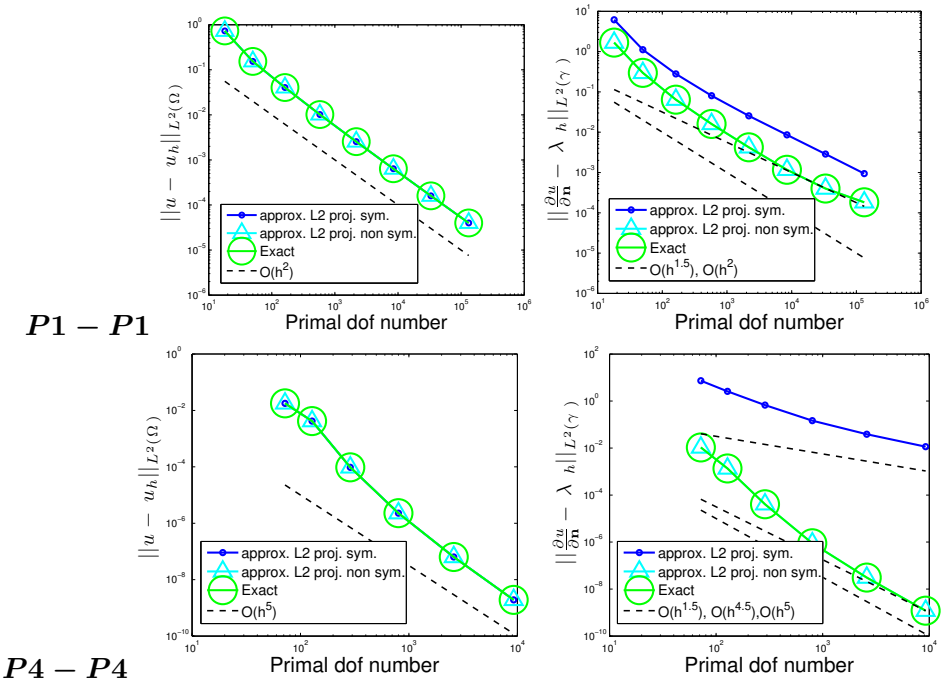

Figure 3.2: L^2 primal (right) and dual (left) error curves: pairing $P1-P1$ (top), $P4-P4$ (bottom) obtained with the symmetric formulation with the lumped L^2-projection (points), with the non-symmetric formulation with the lumped L^2-projection (triangles) and with the exact formulation (circles).

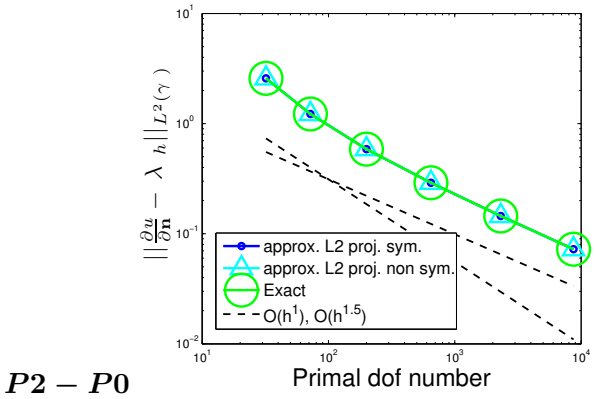

Figure 3.3: L^2 dual error curves for the pairing $P2 - P0$ obtained with the symmetric formulation with the lumped L^2-projection (points), with the non-symmetric formulation with the lumped L^2-projection (triangles) and with the exact formulation (circles).

3.3 Approximate quadrature

3.3.1 Mortar integral evaluation

In a mortar method, we need to evaluate the mortar integrals $\int_\gamma \lambda\, v^M \mathrm{d}s$ and $\int_\gamma \lambda\, v^S \mathrm{d}s$. We define the Lagrange multiplier λ on the mesh of the slave domain $\partial\Omega_S$.

One particular challenge is the evaluation of the first interface integral, i.e., the master-slave mortar integral, due to the product $\lambda\, v^M$ of functions defined on a different mesh. Any quadrature rule based on the slave mesh does not respect the mesh lines of the master mesh and vice versa for a quadrature based on the master mesh.

It is obvious that the use of a suitable quadrature rule based on a merged mesh, i.e., a mesh which respects the reduced smoothness of the master and slave functions at their respective mesh lines, leads to an exact evaluation of the integral. However, the construction of this auxiliary mesh commonly named segmentation process is challenging, especially in the three dimensional case since the shape of the elements varies and is difficult to determine, see, e.g., [86, 95, 96, 53, 42]. Note that in an isogeometric context the merged mesh needs to be constructed in the physical space and then pulled back to the parametric space for each subdomain to ensure the mapping of each quadrature point to effectively lives on the physical boundary. The complexity of constructing such a mesh becomes even more severe in

the case of non-linear and time-dependent problems, where the relative position of the meshes changes in every time or load step which implies to recompute the merged mesh at every step.

Due to this computational complexity, it has been seen very appealing to use a high order quadrature rule either based on the slave mesh or on the master mesh to approximate the master-slave mortar integral, see [48, 108, 37] for some applications in the finite element and the isogeometric analysis contexts. However in the finite element case, early results in [23, 81] showed that this strategy does not necessarily yield optimal methods. More precisely, in the case that only the master mesh is chosen, the best approximation error is affected, while for the case only the slave mesh is chosen it is the consistency error. Numerical results confirmed the lack of optimality with the master integration approach, while with the slave integration approach reasonable results were obtained although not optimal in terms of the Lagrange multiplier norm.

Due to the global smoothness of splines, one could expect the sensitivity with respect to the quadrature rules for isogeometric methods to be less than for finite element methods. In the mortar context, according to the finite element results, it seems interesting to consider a slave integration rule. And, in case of maximal regularity, i.e., $V_{k,h} \subset C^{p_k-1}(\Omega_k)$ one also might expect the quadrature error on a non-matching mesh to be significantly smaller than in the finite element case. These preliminary observations motivate us to study the different cases numerically.

Let us denote the quadrature rule based on the boundary mesh of the slave domain as $\sum\_$, i.e., $\int_\gamma \lambda\, v^M \mathrm{d}s \approx \sum\_ \lambda\, v^M$. We precise that in the examples a Gaussian quadrature rule is used, and we vary the number of Gauss nodes. In all cases, we choose sufficiently many nodes such that the integration on a merged mesh would have been exact. The mortar method with pure slave integration is obtained by evaluating all interface integrals in (1.3) using this quadrature rule, i.e., the discrete system in the one interface case reads as follows: find $(\widetilde{u}_h, \widetilde{\lambda}_h) \in V_h \times M_h$, such that

$$
\begin{aligned}
a(\widetilde{u}_h, v_h) + \sum\nolimits_{\_} (v_h^M - v_h^S)\, \widetilde{\lambda}_h &= f(v_h), \quad v_h \in V_h, \\
\sum\nolimits_{\_} (\widetilde{u}_h^M - \widetilde{u}_h^S)\, \phi_h &= 0, \quad \phi_h \in M_h.
\end{aligned}
$$

The notation $\widetilde{\cdot}$ is used to stress the difference to the discrete solution with exact integration.

In the next section, we present numerical examples which show severe deviations even in the isogeometric case. Hence, even though the global smoothness of the integrated function is increased compared to the finite element case, this integration approach reduces the convergence order drastically.

Moreover, we consider an alternative approach which was proposed in [23, 81] using both integration rules. Additionally denoting $\sum_+$ a quadrature rule based on the boundary mesh of the master domain Ω_M, this approach, resulting in a non-symmetric saddle point problem, reads as follows: find $(\widetilde{u}_h, \widetilde{\lambda}_h) \in V_h \times M_h$, such that

$$\begin{aligned} a(\widetilde{u}_h, v_h) + \sum\nolimits_+ v_h^M \, \widetilde{\lambda}_h - \sum\nolimits_- v_h^S \, \widetilde{\lambda}_h &= f(v_h), \quad v_h \in V_h, \\ \sum\nolimits_- (\widetilde{u}_h^M - \widetilde{u}_h^S) \, \phi_h &= 0, \quad \phi_h \in M_h. \end{aligned}$$

The non-symmetric saddle point problem, which corresponds to a Petrov–Galerkin approach in the primal formulation, was motivated by different requirements for the integration of the primal and dual test functions. Numerical examples showed error values very close to the case of exact integration, but we note that from the theoretical side even the well-posedness of the non-symmetric saddle point problem remains open. In the next section, we present numerical examples which show that also in an isogeometric context, the results are generally close to those from the exact integration case.

3.3.2 Numerical results

In this section, we consider two-dimensional and three-dimensional settings in order to observe the effects of inexact quadrature rules on the optimality of the mortar methods.

Two-dimensional example As a first example, let us consider the same Poisson problem as presented in Subsection 3.2.2.

Regarding the meshes, we consider three different cases, presented in Figure 3.4. In the first two cases, the initial master mesh is a refinement of

the initial slave mesh. The initial slave mesh consists of just one element. In the case $M1$, one uniform refinement step is applied to build the master mesh, in the case $M2$ two uniform refinement steps. Case $M3$ was chosen such that at any refinement level any parts of the slave and master boundary meshes do coincide. The initial interior knots of the slave domain were chosen as $\{\pi/10, 1-\pi/7\}$ in both parametric directions, yielding 9 elements. The initial master mesh consists of four uniform elements.

The cases $M1$ and $M2$ serve as simple tests to investigate the influence of the quadrature error. We note that inverting the role of the master and slave domains is not interesting in these cases as both integration approaches would be able to exactly evaluate the master-slave mortar integral.

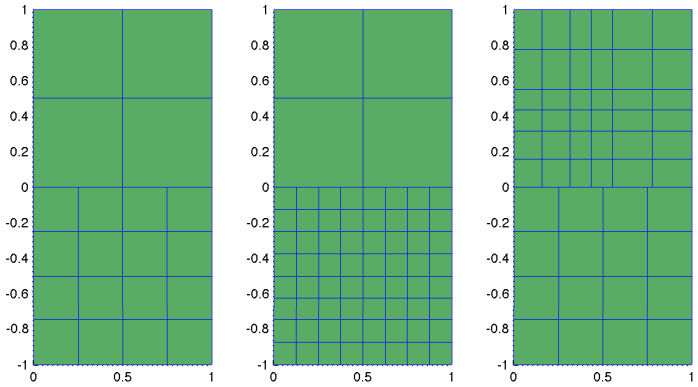

Figure 3.4: Different meshes at mesh refinement level 1. From the left to the right: $M1$ to $M3$.

In the following, we provide different numerical error studies. Starting from the initial mesh, denoted by refinement level 0, we perform uniform refinements for the slave and master domains. We note that the inter-element smoothness of the dual functions can influence the accuracy of the quadrature based on the master mesh, but not the one based on the slave mesh. Therefore for the slave integration approach, the equal order pairing with maximal smoothness is considered, i.e., $M_h = M_h^0 \subset C^{p-1}(\gamma)$, while for the non-symmetric approach we vary the dual degree. In all cases, the primal L^2 and the dual L^2 errors are computed by a comparison with the analytical solution stated in Subsection 3.2.2.

Slave integration approach First, we consider the case $M3$, see Figure 3.4, to measure the impact of the integration error in a general situation. A numerical error study is provided in Figure 3.5 for a different number of additional Gauss points and different spline degrees. For a spline of degree p, we start with $p+1$ Gauss points and investigate the effect of increasing the number of Gauss nodes. It can clearly be seen that the primal and dual solutions are both affected by the inexact quadrature, leading to non-optimal methods. In all cases, the same characteristical behavior can be seen. Up to a certain refinement level, the results with inexact quadrature rules coincide with the ones with no quadrature error. Then, at a certain refinement level, the convergence order is reduced and the error is significantly larger than the exact integration one. The level where this effect starts depends on the considered error norm, the order p and the number of additional Gauss nodes. Moreover, in this situation the higher order splines are more sensitive to the approximate quadrature than the lower order splines.

In almost all cases of Figure 3.5, we observe poor approximation results and a reduced convergence order which is numerically independent of the spline degree. Especially, the rate of the L^2 dual error is very low and in some cases no convergence can be observed anymore.

Secondly, we consider a simple situation to show that even then the impact of the slave integration is noticeable. Let us focus on the cases $M1$ and $M2$, see Figure 3.4, for which the master mesh is a refinement of the slave mesh. See Figure 3.6 for a comparison of results between the cases $M1$ and $M2$ for a spline degree $p = 3$. We note that the low convergence orders of the primal and dual solutions, as remarked above, already appear in this simple context.

Moreover, for a fixed number of slave elements, the error is increasing with the number of master elements. This is expected as there are more points of reduced smoothness which are not taken into account by the quadrature rule. Let us now consider the final numerical convergence rate in more details. In Table 3.1, estimated convergence orders for degree $p = 5$ are given. We notice that the dual L^2 rate breaks down to an order of $1/2$, while the L^2 primal rate lies about $3/2$.

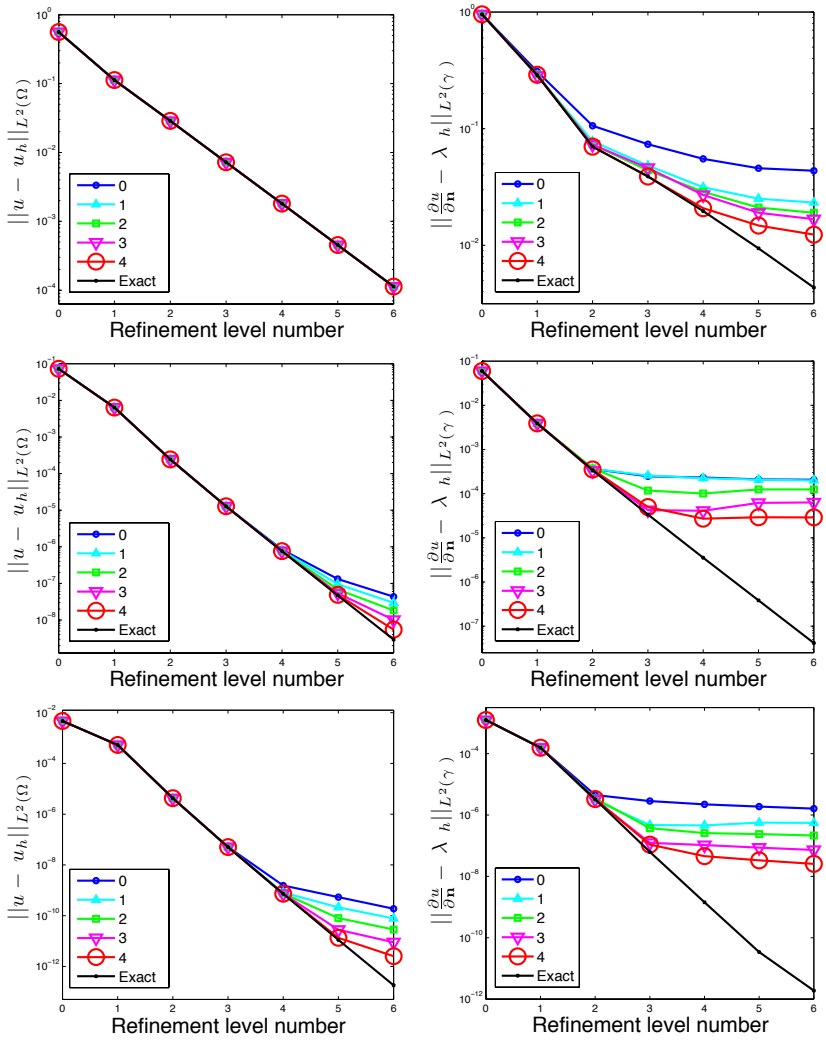

Figure 3.5: 2D results - L^2 primal (left) and dual (right) error curves for the case $M3$: equal order pairings with $p = 1, 3, 5$ (from top to bottom) for the slave integration approach and a different number of additional quadrature points.

add. q.p.	primal error		dual error	
	case $M1$	case $M2$	case $M1$	case $M2$
0	1.63	1.74	0.50	0.50
1	1.63	1.54	0.50	0.50
2	1.63	1.55	0.50	0.50
3	1.63	1.58	0.50	0.50
4	1.63	1.56	0.50	0.50
5	1.63	1.50	0.50	0.50

Table 3.1: 2D results - Last estimated order of convergence of the primal and dual L^2 errors for the cases $M1$ and $M2$: pairing $P5 - P5$ for the slave integration approach and a different number of additional quadrature points.

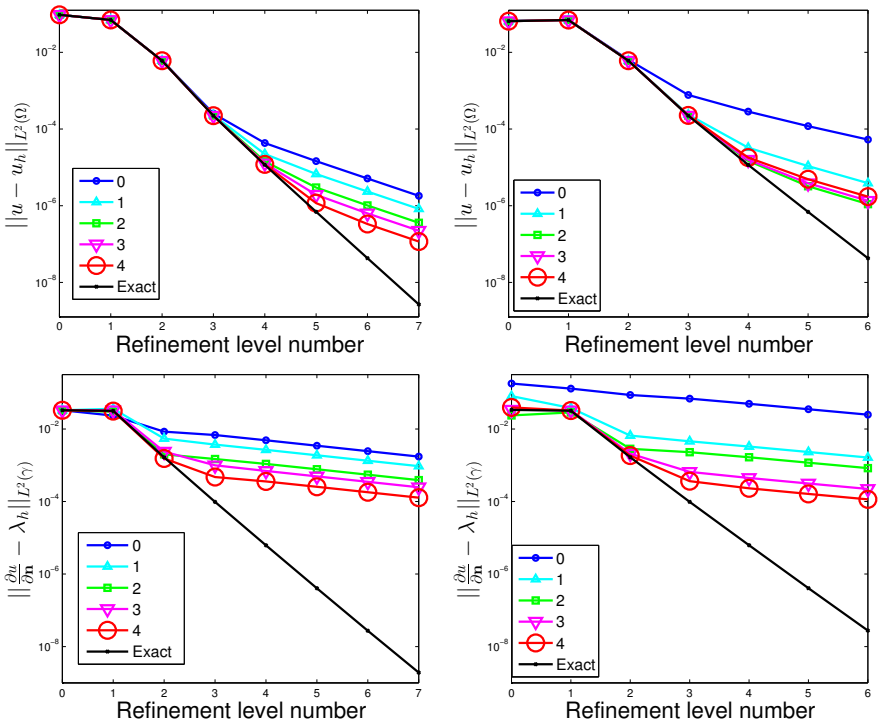

Figure 3.6: 2D results - L^2 primal (top) and dual (bottom) error curves for the cases $M1$ (left) and $M2$ (right): pairing $P3 - P3$ for the slave integration approach and a different number of additional quadrature points.

Thirdly, we have additionally compared the case $M3$ with a similar situation in which the master and slave roles are reverted. The results also show that the integration error is increasing with the increase of the master element number. Thus, in accordance to the practical applications, in a slave integration context it seems worthwhile to choose the slave domain as the finest one.

Moreover, it can be observed that on coarse meshes using the slave integration method it is possible to recover the accuracy of the optimal mortar method simply by increasing the number of quadrature points, see Figure 3.7. However, it has also been shown that the number of necessary quadrature points is drastically increasing with the refinement level. It can easily be seen that the number of Gauss points gets soon impracticably large, see the right picture of Figure 3.7. Furthermore, in several cases, the deviation to the mortar method has been observed to be more severe for high order functions.

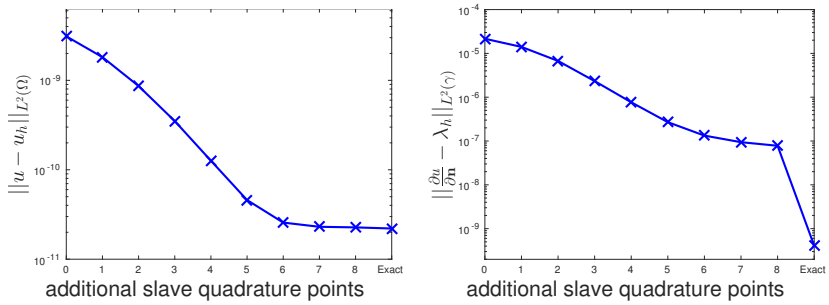

Figure 3.7: 2D results - L^2 primal (left) and dual (right) errors at refinement level number 6 as a function of the number of additional quadrature points for the case $M3$: pairing $P3 - P3$ for the slave integration approach.

Non-symmetric approach The non-symmetric saddle point problem based on the two existing quadrature rules, see Subsection 3.3.1, was introduced to overcome the non-optimality of the pure slave integration approach in a finite element context. Due to the suboptimal results seen in the previous section, it is also interesting to consider it in an isogeometric context.

First, we consider same degree pairings. In almost all tested cases, the results of the non-symmetric approach are comparable to the results of the exact integration case. However, we note that differences could still be seen in some cases. For example, for a degree $p = 1$ in the case $M3$, we obtained a non-optimal method, see in Figure 3.8 the corresponding primal and dual error curves. Note that we do not show any curves in the cases where no disturbance is observed. For example for degree $p = 5$, we observed convergence almost up to machine precision without any remarkable differences compared to the exact integration case.

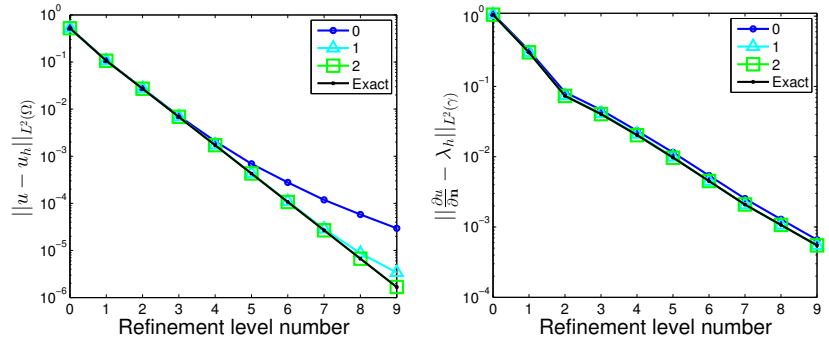

Figure 3.8: 2D results - L^2 primal (left) and dual (right) error curves for the case $M3$: equal order pairing $p = 1$ for the non-symmetric approach and a different number of additional quadrature points.

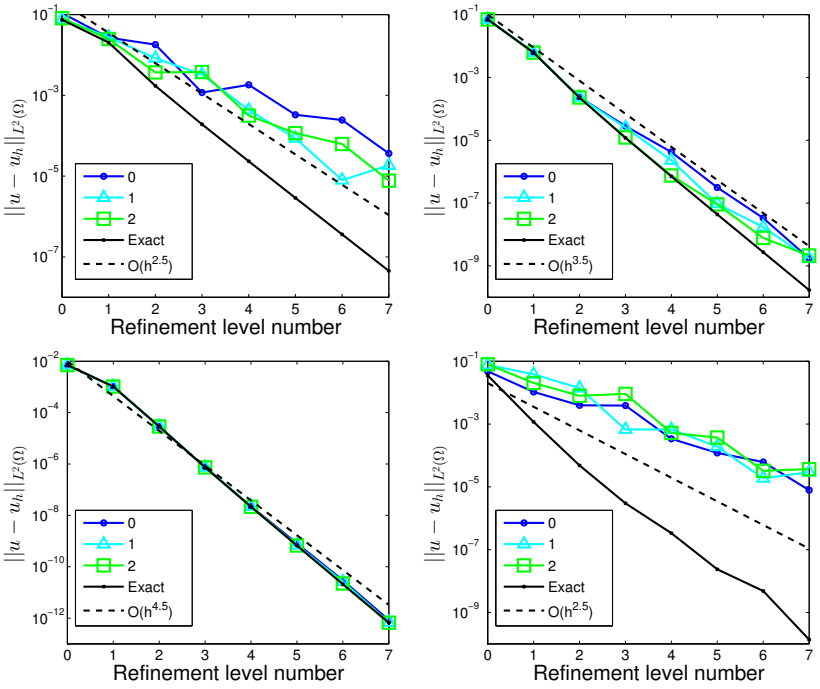

Figure 3.9: 2D results - L^2 primal error curves for the case $M3$: different order pairings for the non-symmetric approach and a different number of additional quadrature points. Top left: $P2-P0$. Top right: $P3-P1$. Bottom left: $P4-P2$. Bottom right: $P4-P0$.

Secondly, we consider dual spaces with lower degrees than the primal ones. Note that in [17] stability for these pairings was only observed if the primal and the dual degrees have the same parity. Similarly to the considered equal order cases, the dual error did not show a significant deviation by the non-symmetric approach. In Figure 3.9, primal error curves are shown for all stable different degree pairings up to a primal degree $p = 4$. We note that theoretically, we expect sub-optimal primal error rates even in the exact integration case, although often improved convergence rates were observed. For a dual degree $p-2k,\ k \in \mathbb{N}^*$, we can expect a convergence of order $\mathcal{O}(h^{p-2k+5/2})$ in the L^2 norm, see the dashed lines in Figure 3.9. For the $P4-P2$ and $P3-P1$ pairings, we observe small differences compared to the exact integration results, but note that the convergence rate is not significantly different from the theoretical expectation. The situation is different for the $P4-P0$ and $P2-P0$ pairings, for which the rate is more disturbed and even below the theoretical expectation. This can be explained by the discontinuity of the dual basis functions which introduces large errors in the integration approximation done with a rule based on the master mesh,

which does not respect these discontinuities.

Three-dimensional example As a second example, we consider a three-dimensional problem with a curved interface. Precisely, we consider the Poisson problem $-\Delta u = f$ on the domain $\Omega = (0,1)^3$, which is divided into two patches by the interface $\gamma = \{(x, y, \rho(x)), (x, y) \in (0,1)^2\}$, with $\rho(x, y) = 1/8\,(1 + x)(1 + y^2) + 1/5$, see Figure 3.10. The bottom subdomain is set as the slave domain. The internal load and the boundary conditions are manufactured to have the analytical solution:

$$u(x, y, z) = \cos(2\pi x)\cos(2\pi y)\sin(2\pi z).$$

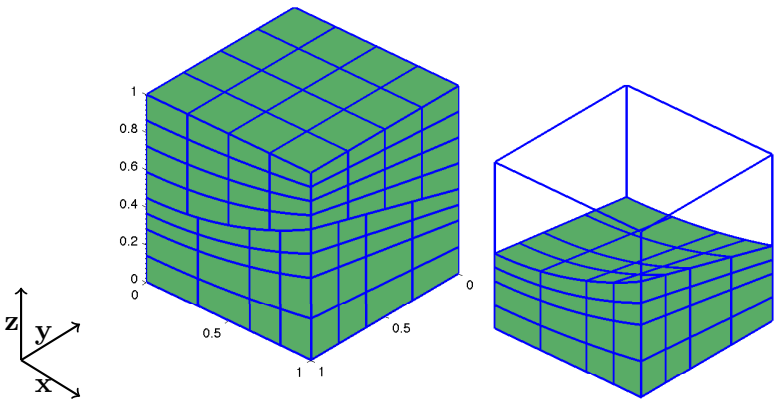

Figure 3.10: Meshes at refinement level 1 (left) and the slave domain (right) illustrating the curved interface.

Note that due to the curved interface, the normal derivative has a complex form, but is still explicitly computable. Neumann conditions are applied such that no cross point modification is necessary. The initial master mesh has 8 uniform elements, while the initial slave mesh has 8 elements given by the breakpoint vector $\{0, \pi/5, 1\}$ in each direction. In the following, we provide some numerical error studies, considering the slave integration approach as well as the non-symmetric approach.

The obtained results are in accordance with the two-dimensional results for both approaches. In Figure 3.11, the deviation for the slave integration approach is shown for the $P4 - P4$ pairing. Although not shown here, we note that the results for the $P2 - P2$ and $P3 - P3$ pairing have a similar

behavior. The non-symmetric approach does not lead to reduced rates considering equal order pairings, i.e., $M_h = M_h^0$, on the refinement levels we considered. As previously, with a lower order dual space, a difference to the exact integration case can be seen. See Figure 3.12 for the disturbance in the primal variable of the $P3 - P1$ and $P4 - P2$ pairings.

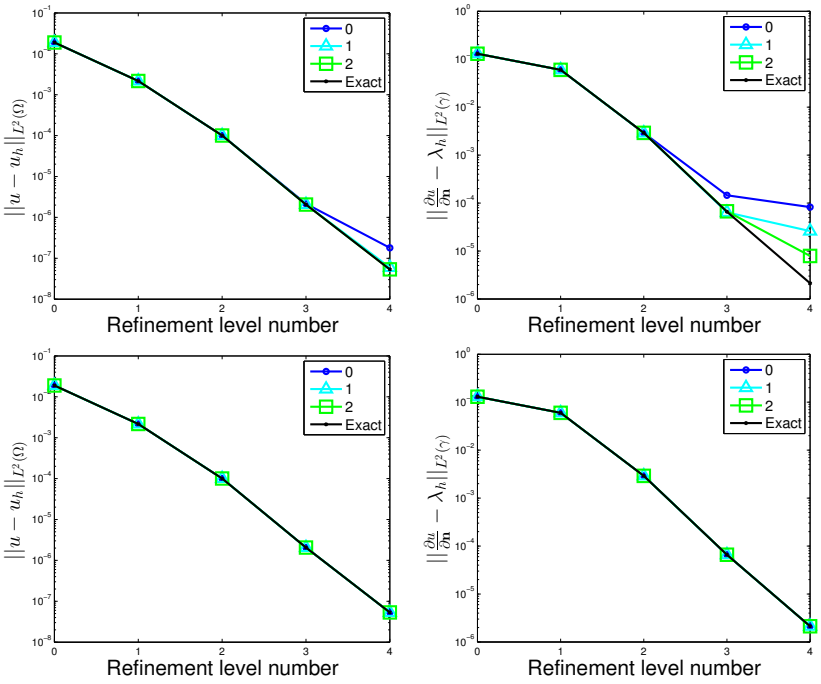

Figure 3.11: 3D results - L^2 primal (left) and dual (right) error curves for the pairing $P4 - P4$, for the slave integration approach (top) and the non-symmetric approach (bottom). Each of the curves being obtained with a different number of additional quadrature points.

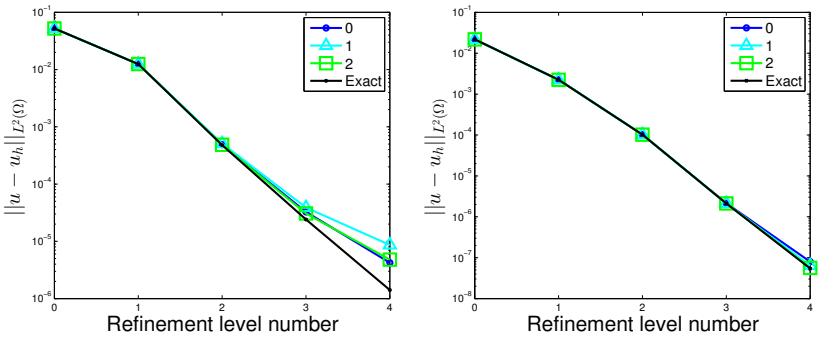

Figure 3.12: 3D results - L^2 primal error curves for the pairings $P3 - P1$ (left) and $P4 - P2$ (right), for the non-symmetric approach and a different number of additional quadrature points.

3.4 Construction of an isogeometric segmentation method

3.4.1 Process details

In this section, we give the details of a segmentation process for isogeometric meshes. We precise that the construction of the merged mesh is done master element by master element.

Let us consider a parametric master element. It is tessellated by a certain amount of points, called tessellation points. They ensure its linear interpolation which is more or less accurate depending on their number. The image of these points have first to be transferred to the slave physical space. Second, they have to be pulled-back in the slave parametric space. To do so, the image of each tessellation point undergo a ray-tracing from the master to the slave boundary using the master normal. I.e., it is moved to the slave boundary along the direction of its master normal, see Figure 3.13 and the Appendix.

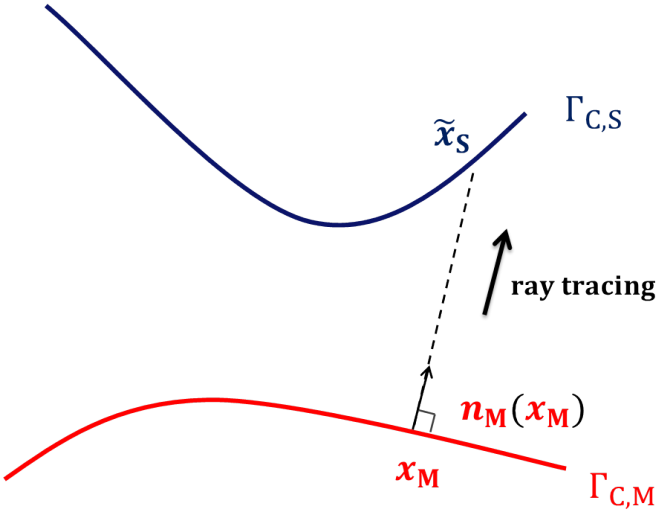

Figure 3.13: A ray-tracing of a master point on the slave.

The ray-tracing operation is unique in the case it exists. We assume its existence in what follows. In a patch gluing context such as the mortar one, in general the master and slave boundaries may differ only a little. Thus, the ray-tracing operation is commonly close to the identity. But as this segmentation process has been thought to be valid for contact problem cases for which in general the boundaries do not match and are fairly apart

one from the other, the method should be able to associate slave to master points in a well-defined way thus the use of a ray-tracing operation.

Then, each resulting point is pulled-back in the slave parametric space using the inverse of the slave mapping. The expression of the inverse of a mapping is not known, but in each point, can be evaluated by the resolution of a non-linear system, see the Appendix. These points define the counterparts of the current master element in the slave parametric space. They are not necessarily aligned, indeed they define a curved element. We note that these points are linearly interpolated, thus the boundary of the resulting element is defined by broken lines. The more tessellation points are considered, the more accurate is the boundary definition of this element.

To finish, the slave knot spans are split into polygons according to the resulting curves, i.e., the master element counterparts. Finally, the resulting polygons are triangularisated. We get a local merged mesh associated to each master element. The global one could be obtained by overlapping the local ones. All of this steps are recalled in Figure 3.14.

Local merged mesh construction

Let us consider a parametric master element. The following steps are applied:

1. Tessellation of the parametric element by a certain amount of points.
2. The image of each tessellation point is ray-traced to the slave boundary using the master normal. We note that the obtained point is uniquely defined.
3. The resulting points are then pulled-back to the slave parametric space. It results in a curved master counterpart element in the slave parametric space described by broken lines.
4. The slave knot spans are split into polygons according to the resulting curves.
5. Triangularisation of the resulting polygons.

Figure 3.14: Synthesis of the local merged mesh construction steps.

The mortar integrals are then evaluated with new quadrature rules built on each of these local merged meshes. The new quadrature points are set in each triangle in the slave parametric space. The slave function evaluation is immediate, while for the master one, one should associate each slave quadrature point to a master one. To do so, the mapping of each

slave quadrature point is projected to the master boundary. We recall that the projection may either not exist or not be unique. While the existence could and is assumed, the uniqueness issue is alleviated by the process. Indeed as a local merged mesh is obtained for each master element, when a quadrature point is projected to the master boundary, we know that the projection should be found in the current master element. Thus assuming an enough fine master mesh ensures the uniqueness of the projection. In Figure 3.15, we give a synthesis of the mortar integral evaluation process.

Mortar integral evaluation

The following steps are applied:

1. Let us loop over the master elements. For each master element, lead the local merged mesh construction, see Figure 3.14.
2. For each local merged mesh, set slave quadrature points, and associate each of them with a master point located on its respective master element.
3. Let us loop over the master elements and read all the data associated to these elements, i.e., the couple slave quadrature points-master points and their underlying values to lead the integral evaluations.

Figure 3.15: Synthesis of the mortar integral evaluation steps.

From the numerical point of view, we note that the quadrature points set in the slave parametric element, once projected back to the master boundary may be out of the current master element. It is necessary for the code to measure the occurrences of this issue. The further the quadrature points are set from the triangle boundaries, the less this problem is encountered. This issue may be alleviated by a compromise between the tessellation parameter finesse, the master mesh element finesse and the necessary quadrature rule order.

In this method, we highlight that a unique normal is considered to transfer points from the slave to the master and vice versa, i.e., the master normal. It allows to maintain a unique normal which is of a high interest in the contact context. In this later context, this normal should be the one taken as contact normal.

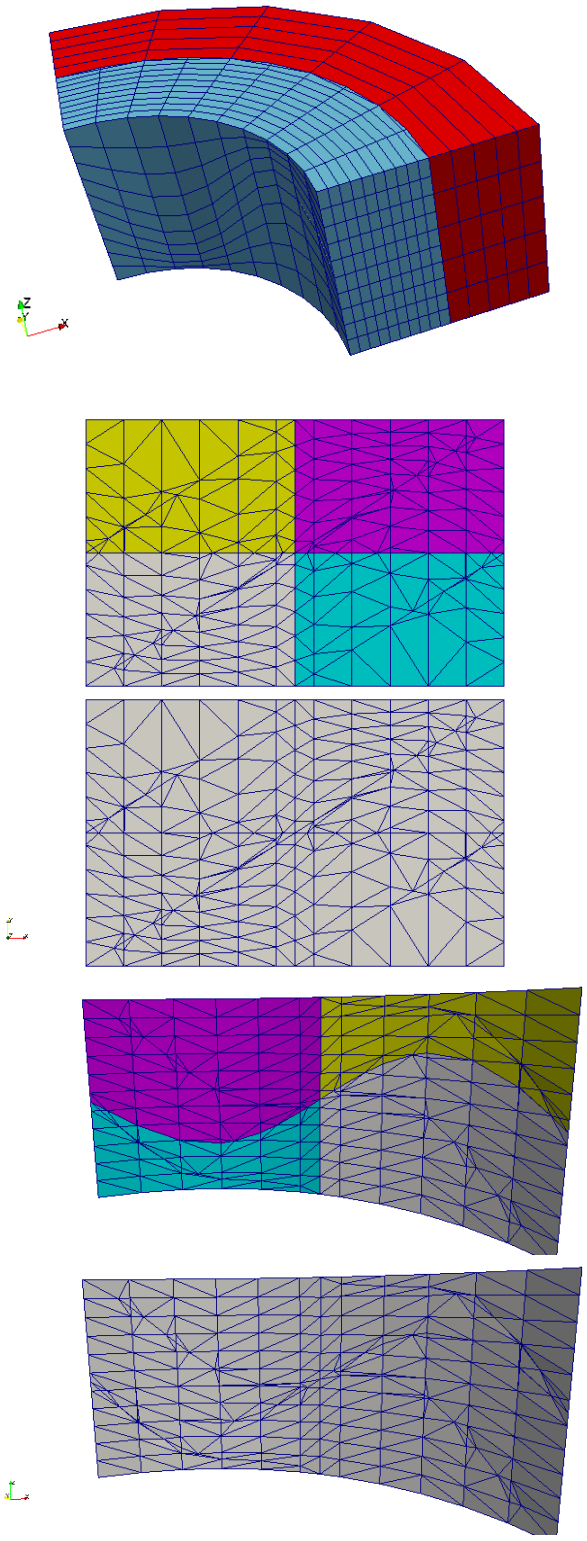

Figure 3.16: From the top to the bottom: the slave (blue) and master (red) subdomains, the slave parametric merged mesh, the master parametric merged mesh, the slave merged mesh and the master merged mesh. Note that the paraview element representation is based on a linear interpolation with a parameter equal to 5.

Building the merged mesh in the slave parametric space, moreover allowing a easier triangularisation process, ensures smoothness of the physical merged mesh that thus lives on the slave boundary. In Figure 3.16, we give an example of merged mesh done with coarse slave and master meshes. The slave mesh has 2 elements per direction while the master mesh is constituted of a unique element.

In the following, let us discuss the common normal choice on some examples. We have chosen the master normal. What would have differed if the slave one had been taken ? In Figure 3.17, the ray-tracing and projection operation inversion is visible. In the first picture of Figure 3.18, we show

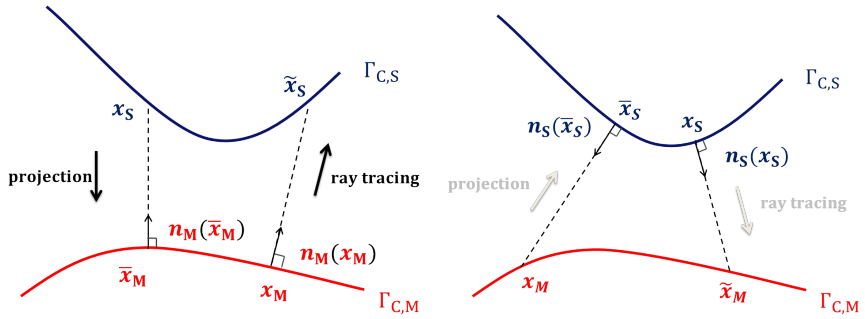

Figure 3.17: Master normal vs slave normal choice as transferred normal in the segmentation process.

an example in which the slave normal choice is not the most efficient one due to non-uniqueness of some projected points. While this issue does not occur in the case the master normal is taken with this boundary configuration, see the second picture of Figure 3.18. We note that in this configuration choosing the master normal is equivalent to keep the slave normal but inverting the master and slave subdomains, see the third picture of Figure 3.18. These later cases allow to point out the importance of a efficient master-slave subdomain choice. Moreover the finesse of the meshes, the shape of the boundaries enters in the choice.

In the fourth picture of Figure 3.18, two general boundaries are considered. Let us consider the case the common normal is the slave one. Thus, in this case, the image of the master tessellation points should be projected to the slave boundary as the slave normal is the transferred normal. The uniqueness of this operation is not ensured. We note that in the case it is, it results in a merged mesh built with the slave normal, normal that should be

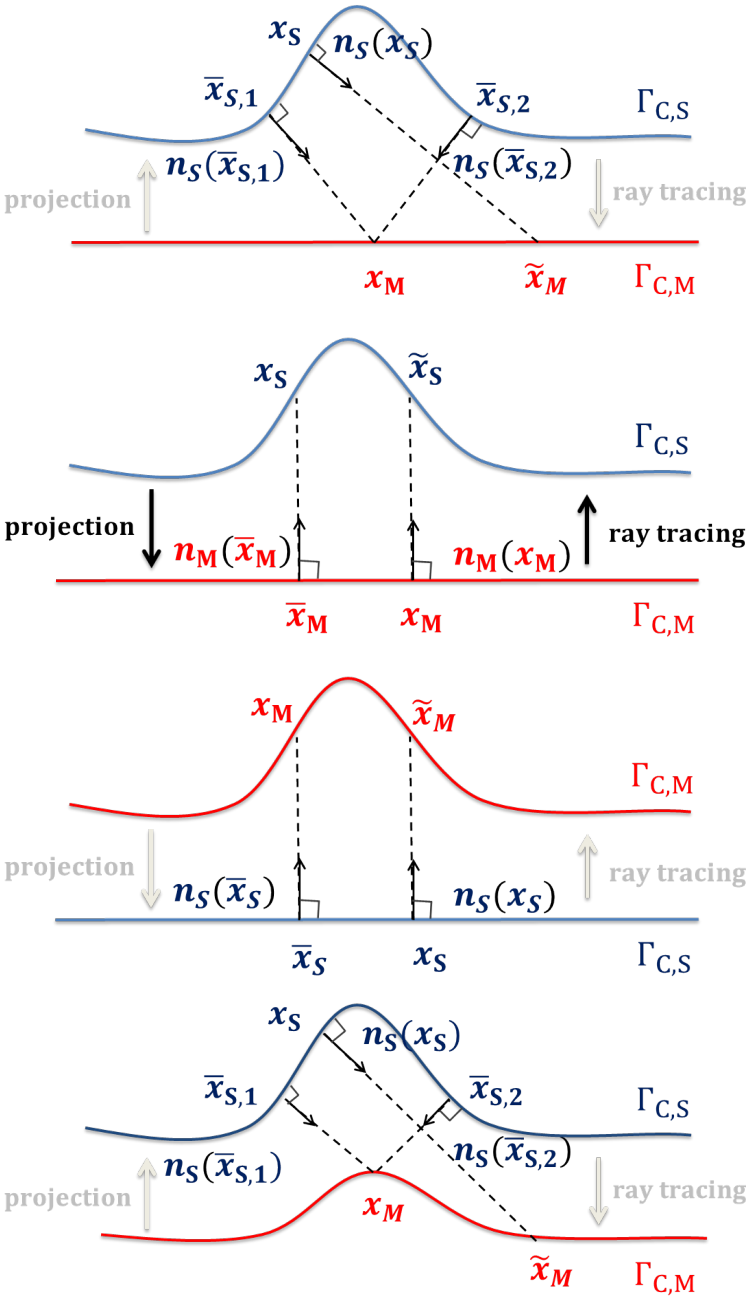

Figure 3.18: Projection and ray-tracing examples with slave normal choice.

used later on as contact normal if a contact problem context is considered. Otherwise, there is anything ensuring a well-definition of the merged mesh, as anything ensures a finite projection point number. Even though this issue does not appear in all the cases, we point out that it is not encountered when the master normal is chosen.

3.4.2 Preliminary results

In this section, we present two preliminary example results. We note that for both cases, the ray-tracing and projection operations are the identity.

Two-dimensional results We present hereafter numerical results for a one dimensional interface for which the relation between the two mapping is not known. The considered test is the infinite plate with a hole presented in Chapter 2, Subsection 2.4.7 on the geometrical parametrization visible in Figure 3.19. No triangularisation process is necessary due to the one dimen-

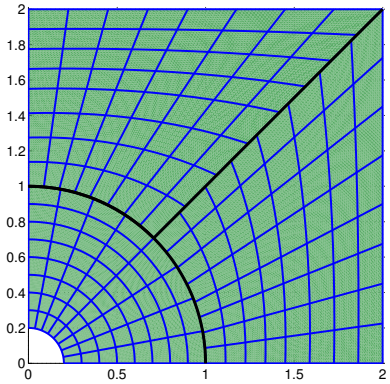

Figure 3.19: A slightly different parametrization of the infinite plate with a hole with 3 subdomains.

sional interface simplification. Error studies have been done in comparison to the analytical solution, see Chapter 2, Subsection 2.4.7. In Figure 3.20, the optimality of some mortar methods is visible for the V primal and L^2 dual errors. This test allows to validate, in a simple way, first contents of the proposed segmentation process.

Three-dimensional results Let us now consider a Poisson equation $-\Delta u = f$ in the three dimensional context solved on a domain Ω decomposed into two subdomains, presented in the top picture of Figure 3.16. The internal load and the boundary conditions have been manufactured

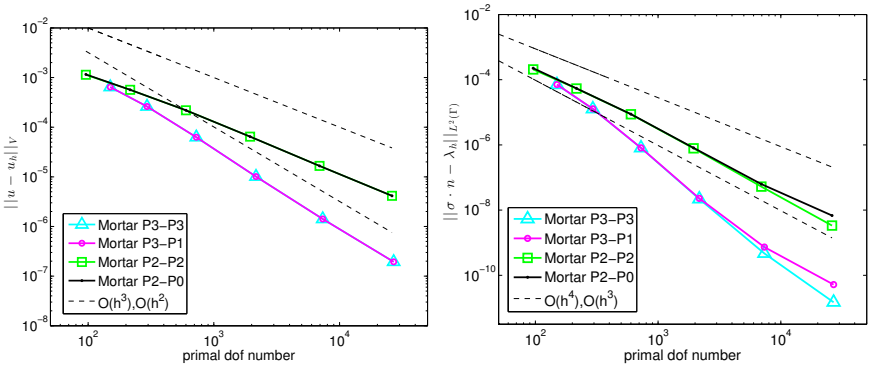

Figure 3.20: V primal (left) and L^2 dual (right) error curves for several degree pairings.

to have the analytical solution $u(x, y, z) = \exp(x)\sin(y)$, see the right picture of Figure 3.21. Dirichlet conditions are applied on the subdomain boundaries which are not juxtaposed with their common interfaces to avoid any cross point issues. The Dirichlet conditions are imposed weakly by the L^2-projection of the solution on the respective boundary trace spaces. While on the remaining boundaries, homogeneous Neumann conditions are imposed. We note that the geometries are for this test not parametrized by NURBS parametrizations. They are instead analytically parametrized in cylinder coordinates. It allows to build this mesh situation case such that the boundary meshes are not conform at all, see Figure 3.16. Moreover, the solution approximation space is thus a push-forward of a spline space (thus the possibility to use linear splines). We led some error studies compared to the analytical solution on a uniformly refined mesh family, starting from a mesh containing $2 \times 2 \times 2$ slave elements and $1 \times 1 \times 1$ master element as refinement level 0, see Figure 3.16.

The results are optimal in the considered cases, see, e.g., in Table 3.2 some V primal orders of convergence. Thus more tests should be performed also testing situations where the projection and ray-tracing operations are not trivial.

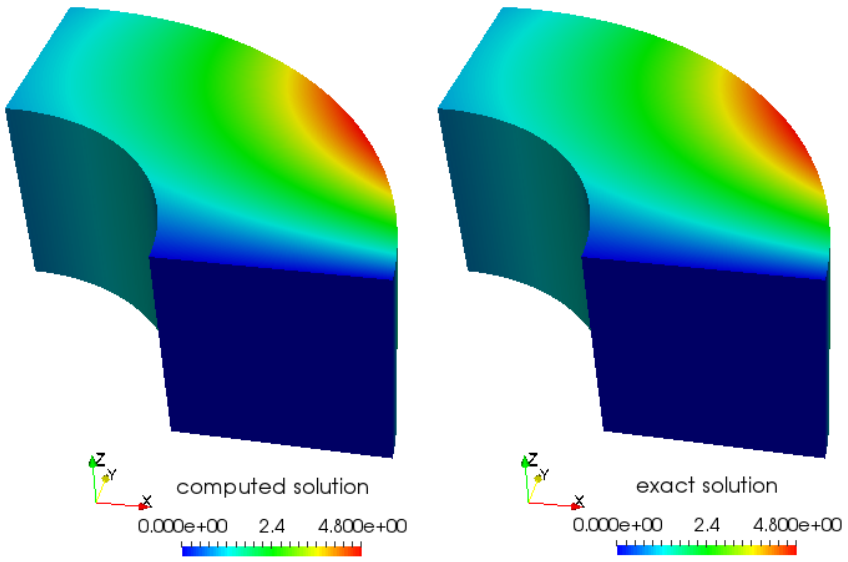

Figure 3.21: Computed solution (left) with spline spaces of degree $p = 2$ and refinement level 4 and the analytical solution (right).

	$P1 - P1$		$P2 - P2$		$P3 - P3$	
level	error value	slope	error value	slope	error value	slope
0	1.3085e+00		5.0465e-01		8.1740e-02	
1	5.5531e-01	1.24	4.3646e-02	3.53	7.4277e-02	0.14
2	1.0281e-01	2.43	2.9535e-02	0.56	7.1237e-03	3.38
3	2.5146e-02	2.03	2.5996e-03	3.51	4.0647e-04	4.13
4	6.1447e-03	2.03	3.0231e-04	3.10	2.0250e-05	4.33

Table 3.2: $||u - u_h||_V$ and its estimated order of convergence.

3.5 Conclusion

In this chapter, the impact of different approximations on the mortar methods has been studied numerically. The former one, the use of an approximate projection, here defined as a lumped L^2-projection, leads to optimal results in the case the projection is not applied to the trial functions.

The second one is a study on the possibility to approximate the mortar integrals by efficient numerical quadrature rules. A precise evaluation of the mortar integrals is generally of a high computational complexity since

it requires the construction of a merged mesh. While it would be desirable to use a quadrature rule based on the slave mesh, numerical examples show that it induces large deviations to the mortar method. Especially the convergence rate of the Lagrange multiplier is reduced to at most $1/2$, independently of the spline degree. While the method improves by increasing the number of quadrature points, the amount of points necessary to obtain nearly optimal results is not predictable. To overcome these difficulties, we have considered a non-symmetric saddle point problem based on both master and slave integration rules, which was previously introduced in the finite element context. Numerical examples demonstrate that for most cases the reached accuracy is close to the optimal one.

The third one regards the construction of an isogeometric segmentation method. Its assets rely on the following aspects:

- the use of a unique normal (the master one) to transfer points from the master to the slave (a ray-tracing operation) and vice-versa (a projection operation).
- a master element-wise process which ensures a well-definition of the projection points by avoiding their non-uniqueness that tends to occur in presence of surface flipping.
- the local triangularisation process led in the slave parametric space, i.e., in a plane which is easier to do.
- the fact the merged mesh lives on the slave surface which allows to maintain the spline smoothness of the surface on which either the gluing is performed or the contact conditions are imposed.

Although, the well-definition of the merged mesh and thus the robustness of the segmentation process is conditioned by master mesh and tessellation point finesse assumptions.

These studies are of interest in the construction of variationally consistent contact methods.

Chapter 4

Isogeometric methods for contact between an elastic body and a rigid ground

Contents

4.1 Introduction

In this chapter, we propose isogeometric numerical methods for the simulation of the contact between an elastic body and a rigid ground. In what

follows, we refer to this problem as rigid-deformable contact. The proposed methods are based on an augmented Lagrangian formulation and the choices of Lagrange multipliers analysed in Chapter 2.

First of all, let us recall that the semi-discrete weak augmented Lagrangian formulation, see (1.11), relative to the considered contact problem, see (1.5), is: find $(\boldsymbol{u_h},\, \lambda_h) \in V_{D,h} \times M_h$ such that

$$\begin{cases} a(\boldsymbol{u_h},\, \boldsymbol{v_h}) \,+\, \displaystyle\int_{\Gamma_{C,S}} <\lambda_h \,+\, \varepsilon\,(g_N)_h>_- [\boldsymbol{v_h}]\,\mathrm{d}s = f(\boldsymbol{v_h}), & \forall \boldsymbol{v_h} \text{ in } V_{0,h}, \\ \displaystyle\int_{\Gamma_{C,S}} \frac{1}{\varepsilon} <\lambda_h \,+\, \varepsilon\,(g_N)_h>_- \phi_h \;\mathrm{d}s - \int_{\Gamma_{C,S}} \frac{1}{\varepsilon}\,\lambda_h\,\phi_h \;\mathrm{d}s \;=\; 0, & \forall \phi_h \text{ in } M_h, \end{cases}$$

where the brackets $<\cdot>_-$ and the discrete gap $(g_N)_h$ are suitably defined in what follows. In this chapter, in Section 4.2, we first discuss our definition for these two latter entities (i.e., $<\cdot>_-$ and $(g_N)_h$) that are mainly driven by the results of the previous chapters. Then, in Sections 4.3 and 4.4, we discuss some numerical aspects and show advantages and drawbacks of our different choices on a series of numerical results.

4.2 Contact problem discretization

The discrete counterpart of the Macauley bracket (see (1.7)) consists in splitting $\Gamma_{C,S}$ into two complementary parts, namely the active region of contact denoted *ACT* and the inactive region of contact denoted *INA*. The semi-discrete augmented Lagrangian formulation, Equation (1.11), can then be written as: find $(\boldsymbol{u_h},\, \lambda_h) \in V_{D,h} \times M_h$ such that

$$\begin{cases} a(\boldsymbol{u_h},\, \boldsymbol{v_h}) \,+\, \displaystyle\int_{ACT} (\lambda_h \,+\, \varepsilon\,(g_N)_h)\,[\boldsymbol{v_h}]\,\mathrm{d}s = f(\boldsymbol{v_h}), & \forall \boldsymbol{v_h} \text{ in } V_{0,h}, \\ \displaystyle\int_{ACT} \frac{1}{\varepsilon}\,(\lambda_h \,+\, \varepsilon\,(g_N)_h)\,\phi_h \;\mathrm{d}s - \int_{\Gamma_{C,S}} \frac{1}{\varepsilon}\,\lambda_h\,\phi_h \;\mathrm{d}s \;=\; 0, & \forall \phi_h \text{ in } M_h, \end{cases}$$

which is equivalent to: find $(\boldsymbol{u_h},\, \lambda_h) \in V_{D,h} \times M_h$ such that

$$\begin{cases} a(\boldsymbol{u_h},\, \boldsymbol{v_h}) \,+\, \displaystyle\int_{ACT} \varepsilon\,(g_N)_h\,[\boldsymbol{v_h}]\,\mathrm{d}s + \int_{ACT} \lambda_h\,[\boldsymbol{v_h}]\,\mathrm{d}s = f(\boldsymbol{v_h}), & \forall \boldsymbol{v_h} \text{ in } V_{0,h}, \\ \displaystyle\int_{ACT} (g_N)_h\,\phi_h \;\mathrm{d}s - \int_{INA} \frac{1}{\varepsilon}\,\lambda_h\,\phi_h \;\mathrm{d}s \;=\; 0, & \forall \phi_h \text{ in } M_h. \end{cases} \tag{4.1}$$

In this section, we discuss multiplier space choices along with the definition of $(g_N)_h$.

4.2.1 Discrete multiplier spaces

An augmented Lagrangian formulation is a mixed method, and thus the discrete Lagrange multiplier space M_h defined on $\Gamma_{C,S}$ has to be selected carefully to ensure the mixed method to be well posed, see, e.g., [13]. In the proposed contact methods, the primal variable is a vector in $\mathbb{R}^{d_u}$ while the multiplier is taken as a scalar, i.e., in $\mathbb{R}$.

In the rigid-deformable frictionless contact context, imposing the active contact condition is similar to impose a displacement value only in the direction of the normal of contact. Thus, as it is done by the use of a Lagrange multiplier, the underlying inf-sup condition is close to the one relative to the mortar context. In that spirit, in the following, we give different multiplier space choices constructed in accordance with the mortar results, see Chapter 2. All our choices are indeed spline spaces built on the boundary mesh of the slave domain. There are enumerated hereafter.

The first choice M_h^0 is a spline space of degree p_S, i.e., of the same degree of the slave geometry and displacement approximation spaces. Note that in the presence of any cross point, a suitable modification of the dual space has to be applied. It ensures not to have a dual space bigger than the normal trace of the primal one which obviously would not fulfill an inf-sup stability condition.

An alternative choice M_h^2 is a degree $(p_S - 2)$ spline space for which the definition requires the trace space of $\mathbf{F}_S$ to be a subset of $C^1(\Gamma_{C,S})$. According to the mortar results, one expects in some cases a method with a reduced convergence order of $1/2$.

More generally, any spline space M_h^{2k} of degree $(p_S - 2k)$ with $k \in \mathbb{N}, k > 1$ could be chosen if we assume enough smoothness on the trace space of $\mathbf{F}_S$. As already pointed out in the case of the mortar method, choosing k larger than 1 would destroy the accuracy on the approximation.

A summary of these choice is given in Figure 4.1. We have numerically validated that for contact problem these choices lead to optimal numerical results, while a theoretical study of the optimality of the proposed methods was not the scope of this work.

For $V_{S,h}$ a push-forward of a NURBS space of degree p_S and :

- M_h a push-forward of a spline space of degree p_S,
- M_h a push-forward of a spline space of degree $p_S - 2$,
- and more generally, for a push-forward of a spline space of degree $p_S - 2k$ ($k \in \mathbb{N}$ and $k > 1$),

one can expect quantitative and qualitative results with the proposed contact methods. In the sense that some pairings will bring optimal results while others will lead to a slight lost in the convergence order.

Figure 4.1: Summary of the multiplier space choices.

As it is well-known that the convergence speed of the method is limited by the low regularity of the contact problem solution, it is worthwhile up to a certain limit to increase in approximation space degrees. Indeed for the smoothest cases, we do not except a convergence order greater than $\frac{3}{2}$ in V norm for the primal variable and $H^{-\frac{1}{2}}(\Gamma_{C,S})$ norm for the dual one, see, e.g., [89]. Thus, the different degree pairing choices are all of interest as they may operate within this accuracy for $p_S \geq 2$.

4.2.2 Concept of discrete gap

The variable of interest in an augmented Lagrangian formulation is $(\lambda + \varepsilon\, g_N)$, denoted $(\lambda_h + \varepsilon\, (g_N)_h)$ in a discrete context.

The gap is function of the slave approximation space, the initial subdomain distance and the contact normal. Even in the special case the primal approximation space is a spline space, the gap may not be one due to the initial subdomain distance and contact normal influences. In the sake of generality, the variable gap has to be projected in a spline space to be smoothly approximated. Indeed, it is natural to discretise it as an element of the multiplier space. This discretization is obtained by a projection on that space. One of the two projections presented in Chapter 3, i.e., the classical L^2-projection (Equation 3.1) and a lumped L^2-projection (Equation 3.2) are considered in what follows. Thus, from now on we use the notation $(\Pi g_N)_h$ for the spline gap defined as the approximation of the gap in the multiplier space where $(\Pi\cdot)$ is one of the two projections mentioned above.

4.2.3 Discrete active region of contact

The discrete active region of contact can be determined in different ways and also approximated on the mesh or not. In the following, we present two different ways to define it, namely an element approach and a control point approach. In what we call element approach we try to define it quite precisely.

Element approach The element approach consists in defining *ACT* as $\Gamma_{C,S}^{\text{ACT}}$, i.e., the region of $\Gamma_{C,S}$ on which the spline $(\lambda_h + \varepsilon(\Pi g_N)_h)$ is negative, respectively *INA* as $\Gamma_{C,S}^{\text{INA}}$ its complementary on $\Gamma_{C,S}$.

First of all, let us consider an exact determination which consists in finding the zero(s) of a spline. Once they have been found, splitting $\Gamma_{C,S}$ into two exact parts that may be discontinuous: $\Gamma_{C,S}^{\text{ACT}}$ and $\Gamma_{C,S}^{\text{INA}}$, by introducing the zero(s) in the boundary slave mesh. We note that these points are introduced just for integration purpose and thus not in the mesh on which the approximation spaces are defined. It ensures that none of them is changed. All the integrations can be led on both exact areas thanks to underlying quadrature rules defined on the new elements resulting from the splitting of existing ones. The high smoothness of splines provide efficient algorithms to find the zero(s), see, e.g., [92, 80].

A more naive and surely less expensive approach consists in finding the elements in which the change(s) of sign occurs() and splitting the elements in two sets: the active ones, i.e., those on which the spline has a negative value, and the inactive ones, i.e., those on which it has a positive value. Those which contain the change(s) of sign are considered as active ones. It leads thus to an over-estimation of the active region of contact but has the advantage to avoid any other quadrature rule definition.

A synthesis of these two element approach methods is given in the two-dimensional case in Figure 4.2. We have numerically proved that the exact determination of the zero(s) ensure the robustness of the proposed contact methods. While, as expected, the second approach is hardly stable and thus the iteration to find the contact region oscillates in several simple situations.

Remark 18. *In the case $(\lambda + \varepsilon(\Pi g_N))$ is approximated with piecewise constants, both element approaches presented above determine the active region in an exact way.*

We point out that in the rigid-deformable contact context all the functions to integrate are defined on a unique mesh. Thus there is no issue to integrate these functions. The only issue encountered in an element approach regards the definition of the two distinct areas the functions should be integrated on, i.e., *ACT* and *INA*. $ACT = \Gamma_{C,S}^{\text{ACT}}$ is either defined exactly as a set of existing mesh elements and new ones, or defined in excess as a set of existing mesh elements. $INA = \Gamma_{C,S}^{\text{INA}}$ is its complementary on $\Gamma_{C,S}$.

Remark 19. *We also refer to [67]. It is a work in the two-dimensional case which focuses on a strategy of adaptive refinement to determine quite exactly in an element approach spirit the active region of contact.*

In the three-dimensional case, the exact determination approach is very difficult to design due to the need to furthermore parametrize in an efficient way the curve which is the zero of the considered spline.

Control point approach The control point approach consists in defining the active region of contact as the support of active functions. A function associated to a control point is determined active if its relative control point value is negative. We note that this approach consists in a stronger imposition of the sign condition than the previous one. More precisely, due the convex-hull property of the splines, checking the conditions at the control points guarantees a stronger condition enforcement on the spline.

Two kinds of control points are distinguished:

- CP_{λ}^{ACT} : the active ones, for which $(\lambda_h + \varepsilon\,(\Pi g_N)_h)_i < 0$, with $i = 1, \ldots, n_{M_h}$
- CP_{λ}^{INA}. : the inactive ones, the others.

All the integration are evaluated with the existing quadrature points, any other definition is necessary. Each active function is integrated on its whole support.

Let us consider as example the spline $(\lambda_h + \varepsilon(\Pi g_N)_h)$

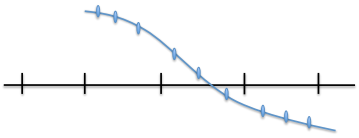

Element approach 1 - a search of the exact active region
Given $\mathbf{O_j}$ an element of $\Gamma_{C,S}$

- determine if a change of sign is occurring on $\mathbf{O_j}$.

On each element where a change of sign had been detected

- search the zero of the polynomial within the element,
- place the correct Gauss formulae on both sides.

Carry the related integrations on $\Gamma_{C,S}^{\text{ACT}}$ and $\Gamma_{C,S}^{\text{INA}}$ using the new quadrature points at the transition elements.

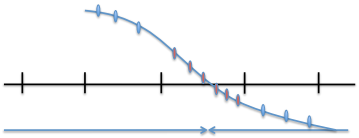

In red, the new quadrature points introduced to lead exactly the integrations on both areas.

Element approach 2 - a general over-estimation of $\Gamma_{C,S}^{\text{ACT}}$
Given $\mathbf{O_j}$ an element of $\Gamma_{C,S}$

- evaluate $(\lambda_h + \varepsilon(\Pi g_N)_h)$ at its quadrature points,
- add the current element to the set of elements which constitute $\Gamma_{C,S}^{\text{ACT}}$ if one of these values is negative, else to $\Gamma_{C,S}^{\text{INA}}$.

Carry the related integrations on $\Gamma_{C,S}^{\text{ACT}}$ and $\Gamma_{C,S}^{\text{INA}}$ using the existing quadrature points.

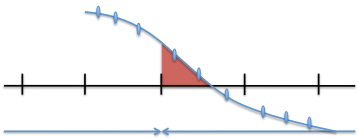

The error committed in this example by the over-estimation of $\Gamma_{C,S}^{\text{ACT}}$ is visible in red.

Figure 4.2: Synthesis of the two considered element approaches in the two-dimensional case.

The augmented Lagrangian formulation, Equation (4.1), is written in a control point approach as: find $(\boldsymbol{u_h},\, \lambda_h) \in V_{D,h} \times M_h$ such that

$$\begin{cases} a(\boldsymbol{u_h},\, \boldsymbol{v_h}) + \displaystyle\int_{\Gamma_{C,S}} \varepsilon \Big(\sum_{k \in CP_\lambda^{ACT}} (\Pi g_N)_k \, B_k^\lambda \Big) \, [\boldsymbol{v_h}] \, \mathrm{d}s + \int_{\Gamma_{C,S}} \Big(\sum_{k \in CP_\lambda^{ACT}} \lambda_k \, B_k^\lambda \Big) \, [\boldsymbol{v_h}] \, \mathrm{d}s \\ = f(\boldsymbol{v_h}) \quad \forall \boldsymbol{v_h} \text{ in } V_{0,h}, \\ \displaystyle\int_{\Gamma_{C,S}} \Big(\sum_{k \in CP_\lambda^{ACT}} (\Pi g_N)_k \, B_k^\lambda \Big) \, \phi_h \, \mathrm{d}s - \int_{\Gamma_{C,S}} \frac{1}{\varepsilon} \Big(\sum_{k \in CP_\lambda^{INA}} \lambda_k \, B_k^\lambda \Big) \, \phi_h \;\; \mathrm{d}s \;=\; 0 \quad \forall \phi_h \text{ in } M_h. \end{cases}$$

4.3 Resolution strategies

In this section, we give the numerical procedure to solve the contact problem written in an augmented Lagrangian formulation as well as we detail its matrix system counterparts.

The iterative algorithm is given in Figure 4.3.

Active set strategy on an augmented Lagrangian formulation

(i) Initialise *ACT* and *INA*

(ii) Compute

$$\begin{bmatrix} K + K_\varepsilon & B \\ B^* & B_\lambda \end{bmatrix} \quad \begin{bmatrix} U \\ \Lambda \end{bmatrix} = \begin{bmatrix} F + F_\varepsilon \\ G \end{bmatrix}$$

(iii) Check convergence, i.e., *ACT* and INA stable

(iv) Update *ACT* and *INA* and go to (ii) until convergence is reached.

with U the displacement vector, Λ the multiplier vector,
K the stiffness matrix, F the primal right-hand side,
G the multiplier right-hand side,
K_ε the stiffness matrix contact counterpart,
B^* and B the mixed bilinear form matrices,
B_λ the multiplier mass matrix.

Figure 4.3: Active set strategy on an augmented Lagrangian formulation.

Below, in the element approach *ACT* stands for $\Gamma_{C,S}^{\text{ACT}}$, respectively *INA* for $\Gamma_{C,S}^{\text{INA}}$, while in a control point approach *ACT* stands for CP_λ^{ACT}, respectively *INA* for CP_λ^{INA}. The matrix system counterparts of the augmented Lagrangian formulation, Equation (4.1), referred as formulation 1 are:

- for the active contact terms

$$
\begin{aligned}
K_{\varepsilon ij} = \quad & \varepsilon \sum_k \frac{\int_{\Gamma_{C,S}} (\boldsymbol{B_j^S} \cdot \boldsymbol{n_M})\ B_k^\lambda \,\mathrm{d}s}{\int_{\Gamma_{C,S}} B_k^\lambda \,\mathrm{d}s} \int_{\mathrm{ACT}} B_k^\lambda\ (\boldsymbol{B_i^S} \cdot \boldsymbol{n_M}) \quad \mathrm{d}s, \\
F_{\varepsilon i} = \quad & -\varepsilon \sum_k \frac{\int_{\Gamma_{C,S}} g\ B_k^\lambda \,\mathrm{d}s}{\int_{\Gamma_{C,S}} B_k^\lambda \,\mathrm{d}s} \int_{\mathrm{ACT}} B_k^\lambda\ (\boldsymbol{B_i^S} \cdot \boldsymbol{n_M}) \quad \mathrm{d}s, \\
B_{ij} = \quad & \int_{\mathrm{ACT}} B_j^\lambda\ (\boldsymbol{B_i^S} \cdot \boldsymbol{n_M}) \quad \mathrm{d}s, \\
B_{ij}^* = \quad & \sum_k \frac{\int_{\Gamma_{C,S}} (\boldsymbol{B_j^S} \cdot \boldsymbol{n_M})\ B_k^\lambda \,\mathrm{d}s}{\int_{\Gamma_{C,S}} B_k^\lambda \,\mathrm{d}s} \int_{\mathrm{ACT}} B_k^\lambda\ B_i^\lambda \quad \mathrm{d}s, \\
G_i = \quad & \sum_k \frac{\int_{\Gamma_{C,S}} g\ B_k^\lambda \,\mathrm{d}s}{\int_{\Gamma_{C,S}} B_k^\lambda \,\mathrm{d}s} \int_{\mathrm{ACT}} B_k^\lambda\ B_i^\lambda \quad \mathrm{d}s,
\end{aligned}
$$

- for the inactive contact terms

$$
B_{\lambda ij} = \int_{\mathrm{INA}} \frac{1}{\varepsilon}\ B_j^\lambda \quad B_i^\lambda \quad \mathrm{d}s.
$$

The underlying matrix formulation is not symmetric with both approaches. In an element approach case, the non-symmetry property just arises from the fact that B^* is not the transposition of B. In a control point approach case, the lack of symmetry also concerns the matrix K_ε and B_λ. Although, we note that the stiffness matrix contact counterparts do not destroy the sparsity pattern of the matrix as its symmetry property in the case a lumped L^2-projection is used thanks to its definition. We note that these two properties are not ensured at all with the classical L^2-projection. Indeed, in the general contact problem case, i.e., in the large displacement-deformation context, the use of a full mass matrix can lead to a tremendous computational cost increase. From now on, for computational reasons we use the gap projection as the lumped L^2-projection defined in Equation (3.2). Moreover, we have numerically observed that thanks to the way this projection is inserted in the methods, it does not affect their accuracy as it was similarly observed in the mortar context in Chapter 3.

In the following, we discuss some modifications to the formulation to possibly obtain a symmetric problem to solve.

First, in that purpose, we can think of modifying the trial functions. Indeed, it is possible to think to take into account the active trial functions for both, displacement and multiplier approximation functions. In this way, we consider the projected displacement trial functions instead of the displacement trial functions. Although, it is already known from mortar method results, see Chapter 3, that it leads to a severe lack of optimality due to the generation of important variational crimes.

Secondly, it is possible to evaluate the active counterpart relative to the mixed bilinear form with as trial function the multiplier ones (i.e., the B^* terms) as its peer, i.e., the active counterpart relative to the mixed bilinear form with as trial function the displacement ones (i.e., the B terms). It was proved in Chapter 3 in the mortar context that it does not affect the optimality of the method. This formulation is referred as formulation 2 in the following. We give below only the details of the matrix terms varying from the formulation 1, i.e., :

for the active contact terms

$$\begin{aligned} B^*_{ij} = & \int_{\text{ACT}} (\boldsymbol{B_j^S} \cdot \boldsymbol{n_M})\, B_i^\lambda \,\mathrm{d}s \;=\; B_{ji}, \\ G_i = & \int_{\text{ACT}} g\, B_i^\lambda \,\mathrm{d}s. \end{aligned}$$

We note that in a control point approach case, it does not lead to a complete symmetric system matrix. The lack of symmetry is coming from the trial multiplier-multiplier function counterparts, i.e., B_λ.

Thirdly, starting from the formulation 2 and evaluating B_λ as $(\int_{\text{ACT}} \frac{1}{\varepsilon}\, \phi_h \;\mathrm{d}s)$ leads to a complete symmetric problem. This formulation, referred as formulation 3 in the following, has been proposed in [39]. This latter modification corresponds indeed to impose the inactive contact condition in a strong way as the spline basis functions are positive. We give below only the details of the matrix terms varying from the formulation 1, i.e., :

- for the active contact terms

$$\begin{aligned} B^*_{ij} = & \int_{\text{ACT}} (\boldsymbol{B_j^S} \cdot \boldsymbol{n_M})\, B_i^\lambda \,\mathrm{d}s \;=\; B_{ji}, \\ G_i = & \int_{\text{ACT}} g\, B_i^\lambda \,\mathrm{d}s, \end{aligned}$$

- for the inactive contact terms

$$B_{\lambda ii} = \int_{\text{INA}} \frac{1}{\varepsilon} B_i^{\lambda} \quad \mathrm{d}s.$$

Remark 20. *In the case the considered pairing is $P2 - P0$, we note that the three formulations are equivalent as for piecewise constants the considered lumped L^2-projection is exact. Although, even in this case, the two active region approaches lead to a slight different solution, as the integrations are not exactly done on the same region.*

We highlight that under the small displacement-deformation assumptions, the use of a control point approach allows to compute the matrices once. Then, at each step to assemble them suitably in the global matrix as the integrals to approximate never change while getting the solution. On the contrary, the use of an element approach requires to evaluate the integrals at each resolution step.

4.4 Numerical results

In this section, we present some numerical study results. First, we consider a low order contact problem on which we focus on some element approach aspects. Secondly, we consider a contact test with the highest possible regularity on which we moreover focus on some control point approach aspects. A comparison with finite element results is done. Finally, the classical Hertz problem in the two-dimensional case is considered. We note that in the different tests, we set the elastic material properties to $E = 1$ and $\nu = 0.3$.

4.4.1 Contact between an elastic square and a rigid ground

We considered the contact problem between a square and a rigid plane, see the top left picture of Figure 4.4. A homogeneous Dirichlet condition is imposed on the top surface of the slave domain, i.e., this surface is clamped. While a Neumann condition $l = \begin{bmatrix} 0.05 \\ -0.1 \end{bmatrix}$, i.e., a pressure is applied on its left surface. This boundary condition is set such that only a part of the potential contact area is active, see Figure 4.4. We precise that the potential slave contact area is its bottom boundary, i.e., the one of

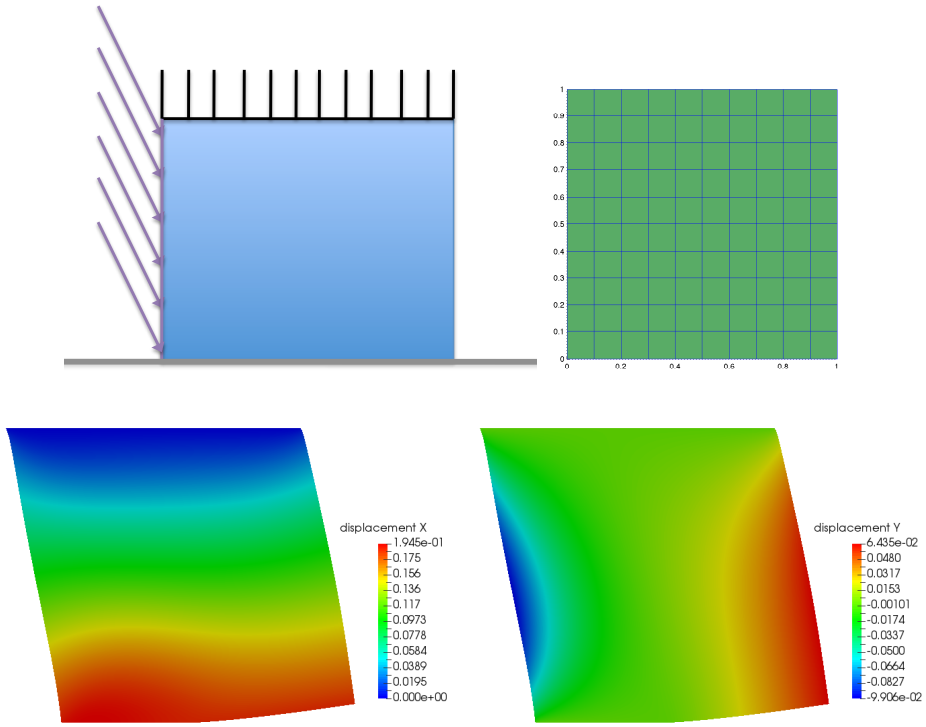

Figure 4.4: Test of Subsection 4.4.1 - Top left: Contact between a square and a rigid plane setting. Top right: the square mesh refinement level 1. Bottom: displacement solution for the pairing $P2-P2$ refinement level 3 obtained with the method F1EA1* (left: u_x, right: u_y).

equation y = 0. Thus the initial gap is here equal to zero.

This test has no analytical solution, although it is known that the regularity of the solution is about 1 in V primal norm and $H^{-\frac{1}{2}}$ dual norm. This problem is solved using the element approaches introduced in Section 4.2. More precisely, we consider the element approaches 1 and 2 in the particular case we use no projection in the augmented Lagrangian contact formulation. It is as considering the formulation 1 introduced in Section 4.2 with 1 as projection coefficient for all k, $(k = 1, \ldots, n_{M_h})$. These methods are respectively referred as F1EA1* and F1EA2*, please note the use of the star due to the specific assumptions done. We strongly highlight that it is possible and mathematically correct only considering same degree pairings as the geometry approximation space is a spline space, the initial gap equal to zero and the contact normal equal to one of the cartesian grid. This formulation restriction allows us to measure the necessity of an exact zero

search to integrate exactly in the two distinct areas in a context polluted by any other approximation.

We led some error studies to compare these two methods on a uniformly refined mesh family, starting from a mesh containing 5×5 elements as refinement level 0. As reference solution, a numerical solution obtained with the method F1EA1* is taken: it is done on a mesh which contains 320×320 elements and with geometry, displacement and multiplier approximation spaces of degree 4.

In Figure 4.5, we give the V primal, L^2 primal and L^2 multiplier errors for the same degree pairings for $p = 1$ to $p = 4$. As expected, the optimality of the method F1EA1* has always been observed, see Figure 4.5, as well as the fact it converges without any status oscillation by definition of the method, see Table 4.1. In the cases F1EA2* converges in a unique way, the method leads to optimal results see Figure 4.5, although the convergence is not warranted by the method. Different element status oscillation cases have been observed. In the second picture of Figure 4.5, it is visible that for the refinement level 4 the method F1EA2* is oscillating between two solutions. They are such that they differ of only one active element. One solution is more accurate than the other one regarding the expecting numerical method capability, as one is on the method convergence curve of desired order. We note that even though more complex oscillation status cases have not been observed for this test, they exist. Furthermore, we note that the finest is the mesh the more occurrences of status oscillation have been observed, see Table 4.1.

Finding efficient exact zero detection methods such as the F1EA1 methods is thus of high interest. Even though the high spline smoothness is bringing efficient root tools, we point out the difficulty of the task. Especially from the computational point of view, as these methods are usually based on adaptive refinement strategies, such as octree one, see, e.g., [67, 118].

Furthermore, for the element approach 2, we also consider the use of different degree pairings for which the active region definition contains no approximation, i.e., for a multiplier degree $p = 0$. It requires the use of a

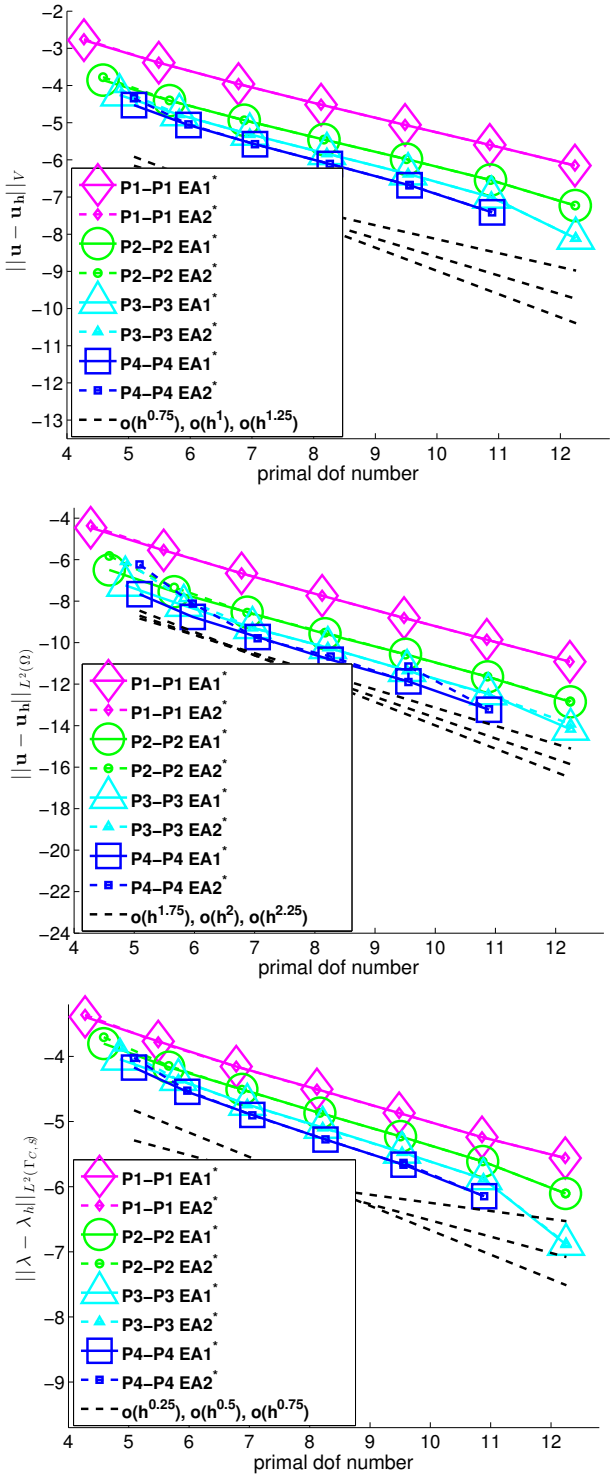

Figure 4.5: Test of Subsection 4.4.1 - From the top to the bottom: V primal, L^2 primal and L^2 multiplier error curves for same degree pairings obtained with the methods F1EA1* and F1EA2* (small markers and dashed lines).

	$P1-P1$		$P2-P2$		$P3-P3$		$P4-P4$	
ref. level	EA1*	EA2*	EA1*	EA2*	EA1*	EA2*	EA1*	EA2*
2	6	7	7	7	6	7	7	7
3	8	8	7	8	7	9	7	8
4	8	9	10	9	7	11	9	$\mathbf{7^{\Sigma}}$
5	8	10	9	9	8	11	9	9
6	10	11	9	$\mathbf{8^{\Sigma}}$	10	$\mathbf{11^{\Sigma}}$	9	11

Table 4.1: Test of Subsection 4.4.1 - Iteration number for the rigid-deformable contact methods F1EA1* and F1EA2* with same degree pairings. Note that Σ stands for simple status oscillation occurrence, i.e., when the method hesitates on the status of two consecutive elements.

projection in the formulation, i.e., to consider the formulation 1 as exactly defined in Section 4.2. This method is denoted F1EA2. In Figure 4.6, we plot the L^2 primal and L^2 dual error curves for the pairings $P2-P0$ and $P4-P0$. The results are optimal and more robust. Moreover we observe that taking a reduced dual degree is not necessary diminishing the accuracy on the primal variable, as also observed in the mortar context in Chapter 2.

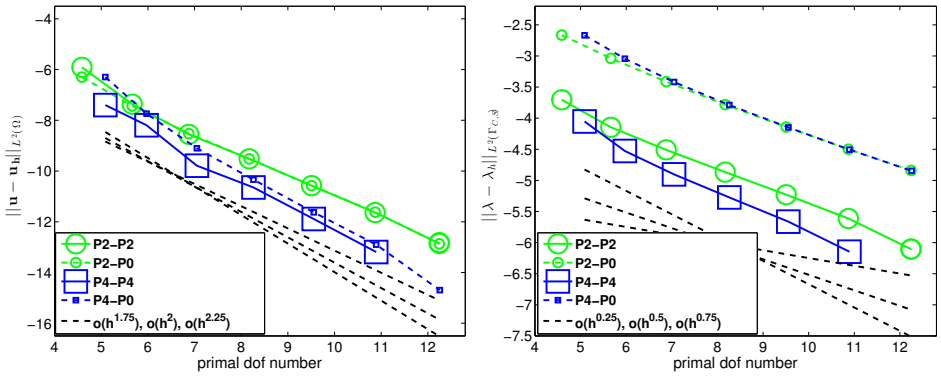

Figure 4.6: Test of Subsection 4.4.1 - L^2 primal (left) and L^2 multiplier (right) error curves for stable pairings with a multiplier degree $p = 0$ in comparison to their respective same degree pairings obtained with the method F1EA2.

4.4.2 High regularity contact problem between an elastic rectangle and a rigid ground

We considered the contact problem between a rectangle and a rigid plane, see the top left picture of Figure 4.7. A Dirichlet condition is imposed on the top surface of the slave domain. It is such that the horizontal component is equal to zero while the vertical one is a spline of degree 2. See on the top right picture of Figure 4.7 the repartition of this vertical component along the slave top surface. We precise that the potential slave contact area

is its bottom boundary, i.e., the one of equation y = 0. Thus the initial gap is here equal to zero. This boundary condition setting is such that only a part of the potential contact area is active, see Figure 4.8, and such that the regularity of the solution is about $\frac{3}{2}$ in V primal norm and $H^{-\frac{1}{2}}$ dual norm, i.e., it is a contact test of high regularity. We note that this test has no analytical solution.

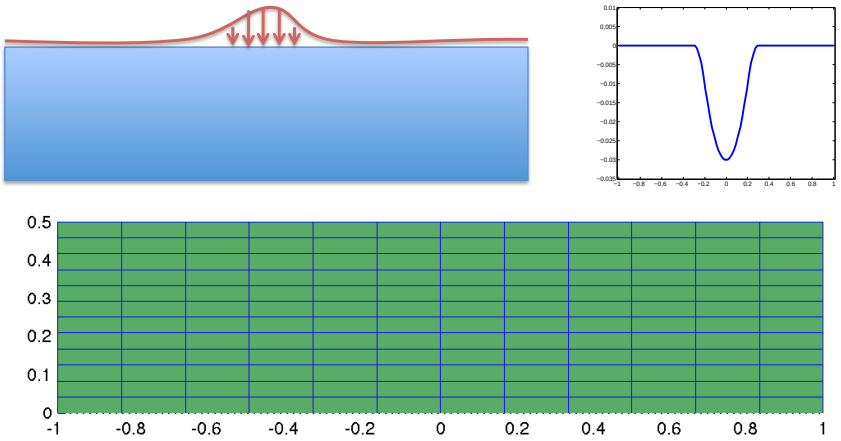

Figure 4.7: Test of Subsection 4.4.2 - Top: On the left picture, the contact test setting. On the right picture, the vertical component of the applied Dirichlet condition. Bottom: the mesh refinement level 0.

This problem is solved using both, the element and the control point approaches introduced in Section 4.2. More precisely, for this test we also consider the method F1EA1* being in a setting its use is possible. Moreover, we consider the control point approach F1CP, i.e., the weak contact formulation 1 with a control point approach to define the active contact region. We led some error studies to compare these methods on a uniformly refined mesh family, starting from a mesh containing 12×12 elements as refinement level 0 visible in the third picture of Figure 4.7. As reference solution, a numerical solution obtained with the method F1EA1* is taken: it is done on a mesh which contains 384×384 elements and with geometry, displacement and multiplier approximation spaces of degree 4.

The optimality and the robustness of the method F1EA1* have always been observed, see, e.g., Figure 4.9. In this figure, we plot the V primal and

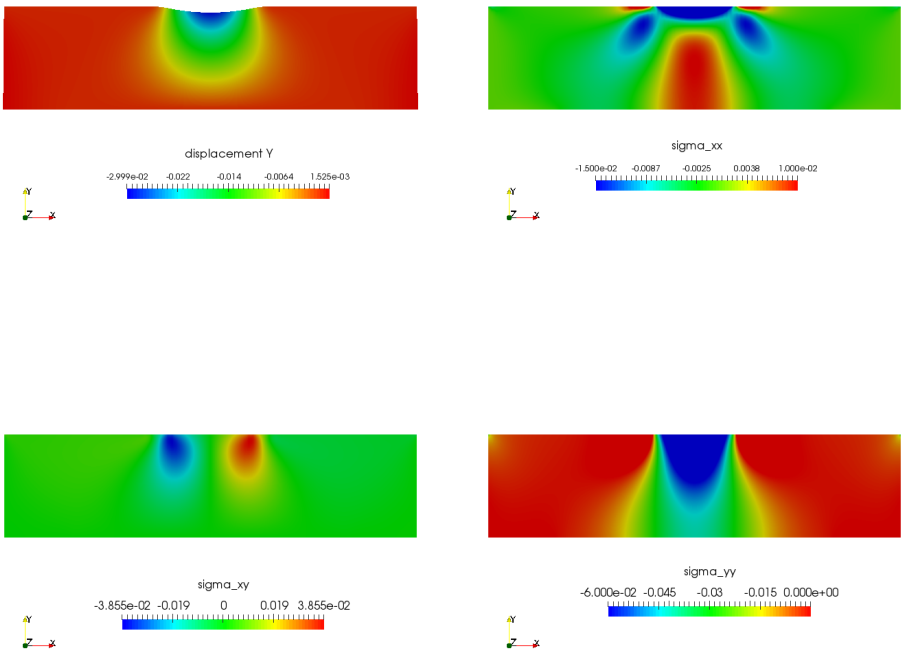

Figure 4.8: Test of Subsection 4.4.2 - Displacement and stress solution repartition for the pairing $P2 - P0$ refinement level 3 obtained with the method F1CP. Top: u_y (left) and σ_{xx}(right). Bottom: σ_{xy} (left) and $\sigma_{yy}(right)$.

L^2 dual error for the same degree pairings $P2 - P2$ and $P3 - P3$. Regarding the method F1CP, the optimality is observed in the case it converges. We remark that in the context of Figure 4.9, convergence has been always reached.

Moreover checking that optimal convergence order can be reached even in the highest contact regularity context with the considered methods, we compare the results of high regularity spline basis to finite element ones. We point out that the finite element basis used is not the classical Lagrange polynomial one, but rather the basis obtained from degree elevation of splines defined on a specific mesh. It is built such that the number of unknowns in the FE and IGA contexts are quite similar in order to compare fairly the two method efficiencies. We note that for $p = 1$, it coincides with the Lagrange basis. For a pairing of degree p, the mesh step on which the FE space is defined by degree elevation of splines is equal to $\frac{h}{p}$, h being the

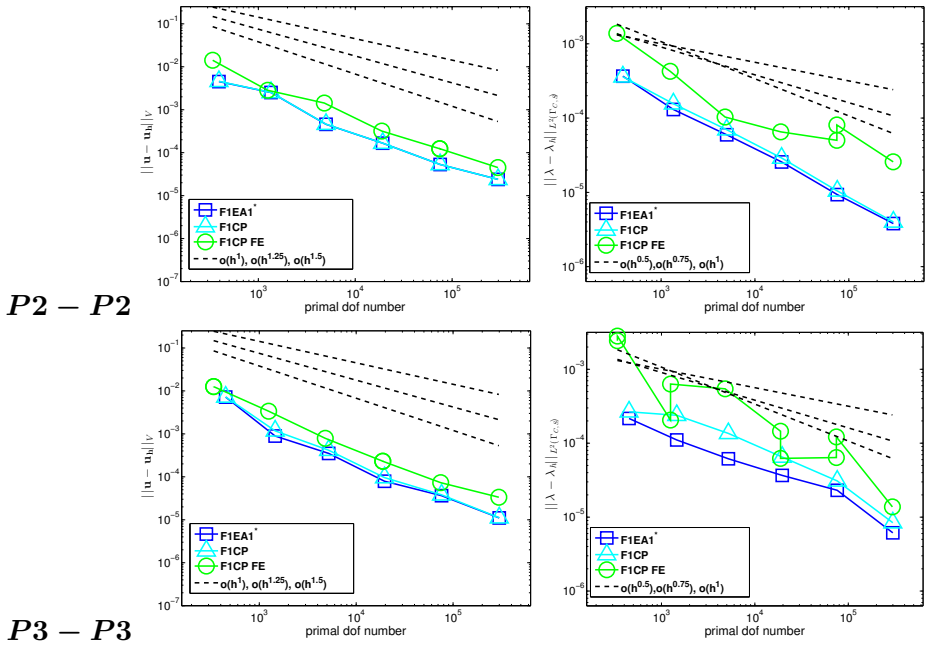

Figure 4.9: Test of Subsection 4.4.2 - V primal (left) and L^2 multiplier (right) error curves for the pairings $P2-P2$ (top) and $P3-P3$ (bottom) obtained with the methods F1EA1* for high regularity splines (squares) and F1CP for high regularity splines (triangles) and finite element basis (circles).

mesh step on which the spline space is defined. We note that this later space is the IGA one.

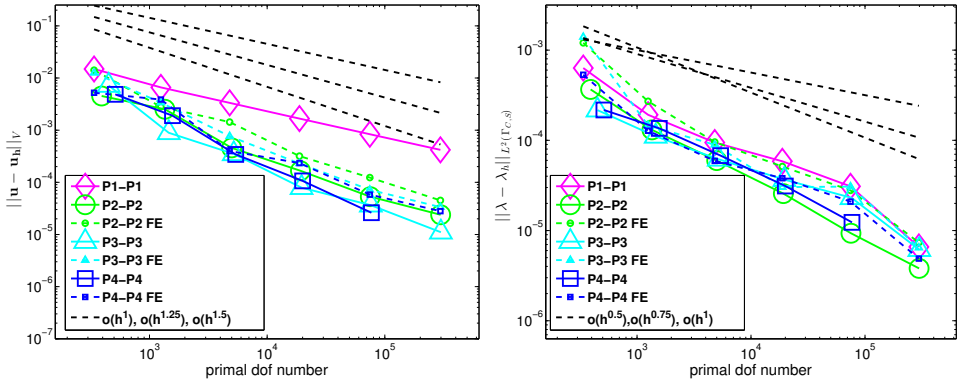

Figure 4.10: Test of Subsection 4.4.2 - V primal (left) and L^2 multiplier (right) error curves for same degree pairings obtained with the method F1EA1* for high regularity splines and finite element basis (small markers and dashed lines).

We compare finite element method and isogeometric analysis with the method F1EA1*. In Figure 4.10, we give some error results for same degree pairings for $p = 1$ to $p = 4$. Optimal results can be observed. We obtained

as theoretically expected reduced slope values for the pairing $P1 - P1$ in comparison to the other pairing results. Furthermore, it is visible that isogeometric analysis results are slightly more accurate than the finite element ones. The comparison FEM-IGA is also done with the method F1CP. The method is optimal in the cases it converges, see, e.g., Figure 4.9. Although, we note that for control point approach methods, FEM has been observed to be less robust than IGA.

4.4.3 Hertz problem in the two-dimensional case

Let us consider the classical Hertz problem in the two dimensional case, i.e., the frictionless contact of a disk with a rigid plane, see [63, 79]. The load, boundary conditions and geometry setting are presented in the first picture of Figure 4.11.

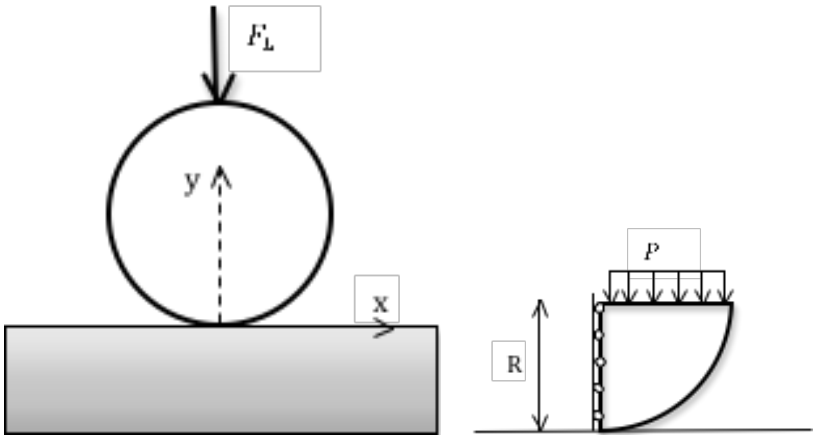

$$p(x) = \frac{2\,F_L}{\pi a^2}\sqrt{(a^2 - x^2)} = p_0\sqrt{(1 - \frac{x^2}{a^2})}$$

$$P = \frac{F_L\,R}{2} \qquad p_0 = \frac{2\,F_L}{\pi a^2} \qquad a = \sqrt{\frac{4\,R\,F_L}{\pi E^*}} \qquad E^* = \frac{E}{1-\nu^2}$$

In the numerical test, we have taken: $F_L = 0.007$ and $R = 0.7$.

Figure 4.11: Test of Subsection 4.4.3 - Two-dimensional case Hertz problem - Setting, modelling setting and analytical solution.

The problem is completely symmetric, i.e., from the geometry, load and boundary condition points of view. It allows to approach numerically it by the study of the contact between one quarter of a disk and the rigid plane. This quarter of disk is subjected to a Neumann condition, i.e., a pressure on its top boundary, with a horizontal component equal to zero, and a vertical

one negative and equal to the repartition of the load applied on the disk. It is subjected to a horizontal homogeneous Dirichlet condition on its left boundary to impose the geometrical symmetry conditions.

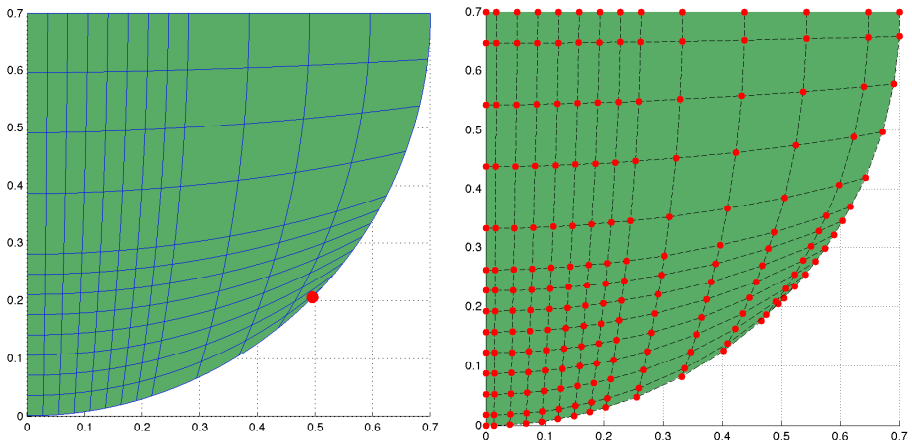

Figure 4.12: Test of Subsection 4.4.3 - Mesh and control net of the considered geometry at refinement level 0.

The potential slave contact area is a part of its circular boundary. We note it is not the all circular boundary due to the quarter disk geometrical parametrization used. The initial gap is here not equal to zero. The solution has the highest possible regularity, i.e., about $\frac{3}{2}$ in V primal norm and $H^{-\frac{1}{2}}$ dual norm, and it is such that only a small part of the potential area of contact is active.

This mapping leads to the presence of a geometrical singularity point while refining, see it in red in the left picture of Figure 4.12. We recall that it has been proved that isogeometric analysis is able to handle some severe mesh distortion cases, see [77]. We led some error studies to compare the efficiency of different methods on a uniformly refined mesh family, starting from the mesh visible in Figure 4.12 as refinement level 0. This mesh contains $(8+4)\times(8+4)$ elements. It has been chosen to set more elements in the area foreseen as active one in order to save some degrees of freedom while refining due to the classical NURBS tensor structure.

On this problem, we test the element approach 2 and the control point approach for the three formulations proposed in Section 4.2, i.e., we are considering six different numerical methods. They are referred respectively as F1EA2, F2EA2, F3EA2, F1CP, F2CP and F3CP. For the control point approaches, we consider same as different degree pairings, while for the

element approaches, we consider the pairings $P2 - P0$ and $P4 - P0$ for which the determination of the active region of contact contained no approximation.

For the multiplier, the analytical solution is known, see [63, 79], while for the displacement we need to choose a reference solution. It is typical in an analytical solution lack case to set as reference solution a numerical one obtained with high degree approximation spaces and on a fine mesh. For this test, we have done two different error studies with as analytical solutions:

- one obtained with the method F2CP on a mesh containing $(256 + 128) \times (256 + 128)$ elements and with geometry, displacement and multiplier approximation spaces of degree 4,
- and one obtained with the method F1EA2 on a mesh containing $(256 + 128) \times (256 + 128)$ elements, with geometry and displacement approximation spaces of degree 4 and multiplier approximation space of degree 0.

The reason of this double analytical choice will be discuss in the latter.

First, let us consider the multiplier variable. In the different error study cases, i.e., with the analytical solution, but also with the two reference solutions for same and different degree pairings, optimality is reached when convergence occurs.

In Figures 4.13 and 4.14, some L^2 multiplier error evolutions are given. In Figure 4.14, we plot the L^2 multiplier error curve for the pairing $P2 - P2$ obtained with the method F1CP on the considered uniformly refined mesh family and for others meshes in order to describe more precisely the error evolution. The optimality of the method is visible as a stair error evolution. This behaviour is typical to contact problem due to the discrete definition of the active contact region. Indeed, anything is ensuring that for any general refinements, the active region of contact is better caught. We note that some status oscillation cases are observed. Two different solutions can be obtained in these cases, one leads to a point on the proper order error curve and one with a higher error value, see the peaks in Figure 4.14.

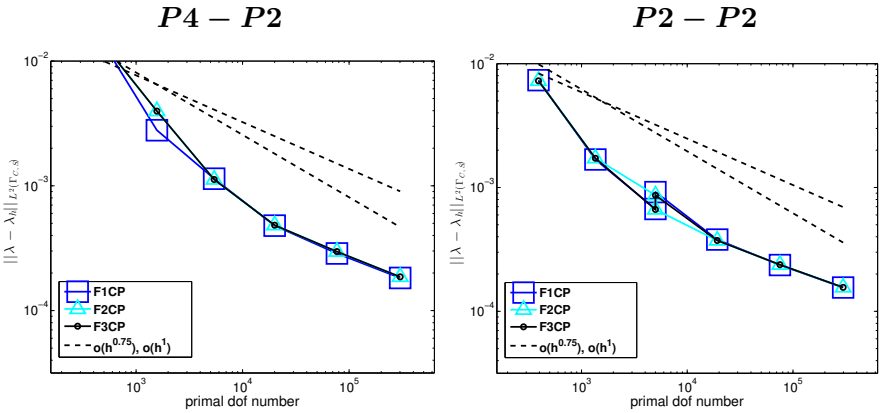

Figure 4.13: Test of Subsection 4.4.3 - L^2 multiplier error curves for the pairing $P4 - P2$ (left) and $P2 - P2$ (right) obtained with the control point approaches and computed in comparison to the analytical solution.

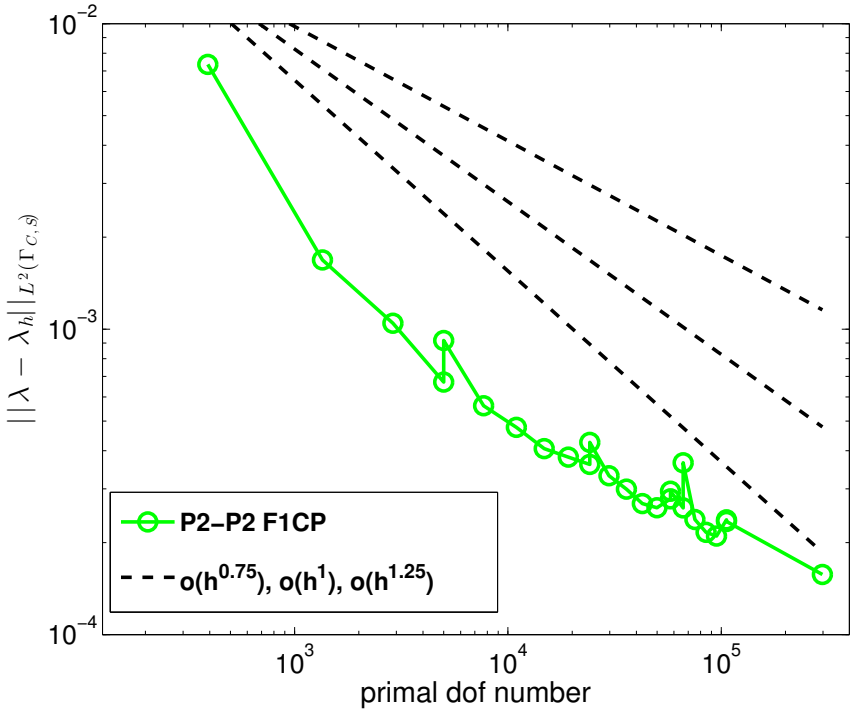

Figure 4.14: Test of Subsection 4.4.3 - L^2 multiplier error curves for the pairing $P2 - P2$ obtained with the method F1CP and computed in comparison to the analytical solution.

Let us now consider the primal error evolution. In Figures 4.15 and 4.16, we show some primal error results computed with the two reference solutions mentioned above. We precise that these solutions have been chosen as they are obtained at the finest considered refinement level. They are also a good compromise between high primal approximation space order and low multiplier error once computed by comparison with the analytical solution.

In Figure 4.15, we give some results for the pairing $P2 - P0$. It is visible that for a fixed approach the three formulations lead to the same solution, as expected. Generally, the results show that a control point approach always leads to an optimal method in the case it converges, see the left pictures of Figures 4.15 and 4.16. Regarding the element approaches, it is slightly different. Indeed, they lead to an optimal approach in the case the error is computed in comparison to the second analytical solution. While in the case it is computed in comparison to the first analytical one, the error is optimal up to a certain refinement level for which it is reaching a threshold value, see the left pictures of Figures 4.15 and 4.16.

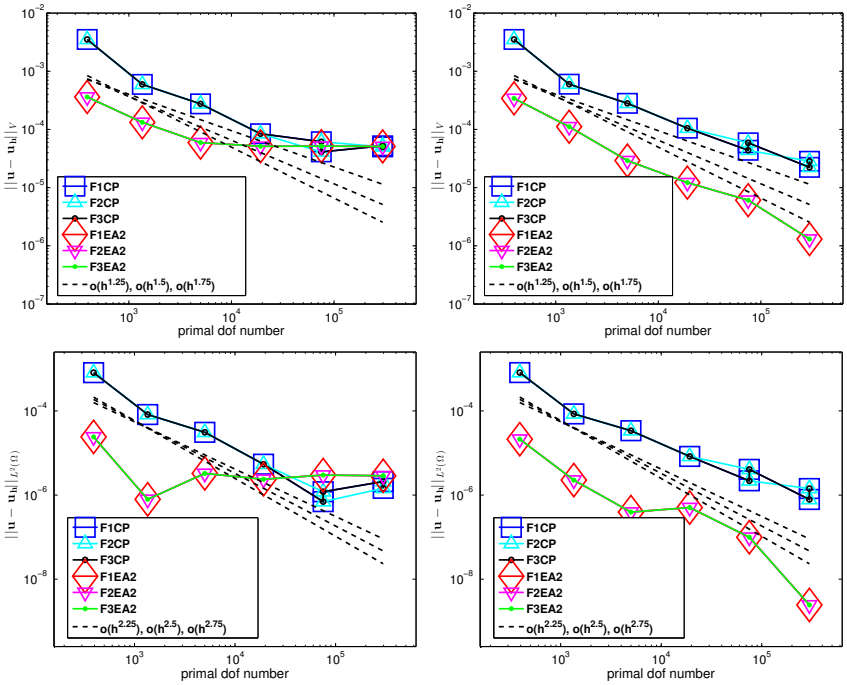

Figure 4.15: Test of Subsection 4.4.3 - V and L^2 primal error curves for the pairing $P2 - P0$ obtained with the six considered methods and computed in comparison to the first (left) and second (right) reference solution.

It means that the second analytical solution is more accurate on the primal variable than the first one. We recall that both analytical solutions are computed with a primal approximation space of degree 4 while the dual approximation space degree is 4 for the first solution and 0 for the second one. Thus the fact that the second analytical solution is more accurate on the primal variable than the first one is either due to the discrete active region definition (element or control point approaches) or to the approximation done by the use of a lumped L^2-projection.

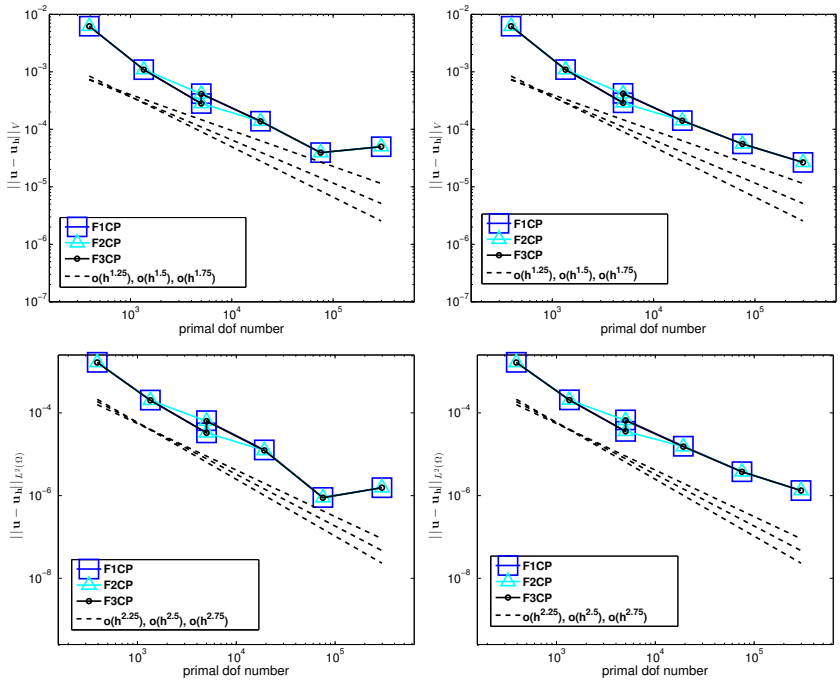

Figure 4.16: Test of Subsection 4.4.3 - V and L^2 primal error curves for the pairing $P2-P2$ obtained with the control point approaches and computed in comparison to the first (left) and second (right) reference solution.

In Figure 4.18, we show qualitative multiplier solutions obtained with both reference solutions in comparison to the analytical one. Moreover, in Figure 4.17, we show the repartition of the primal and multiplier errors obtained with the first reference solution by comparison to the second one. The main error counterparts are, as expected, localised in the contact transition active-inactive area.

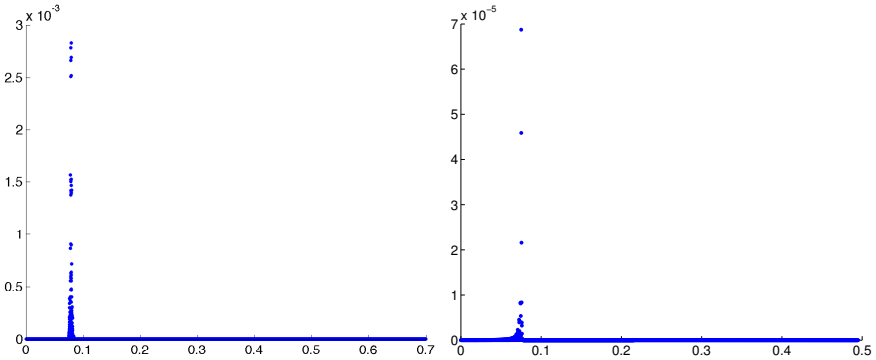

Figure 4.17: Test of Subsection 4.4.3 - V primal (left) and L^2 dual (right) error repartition between the two reference solutions.

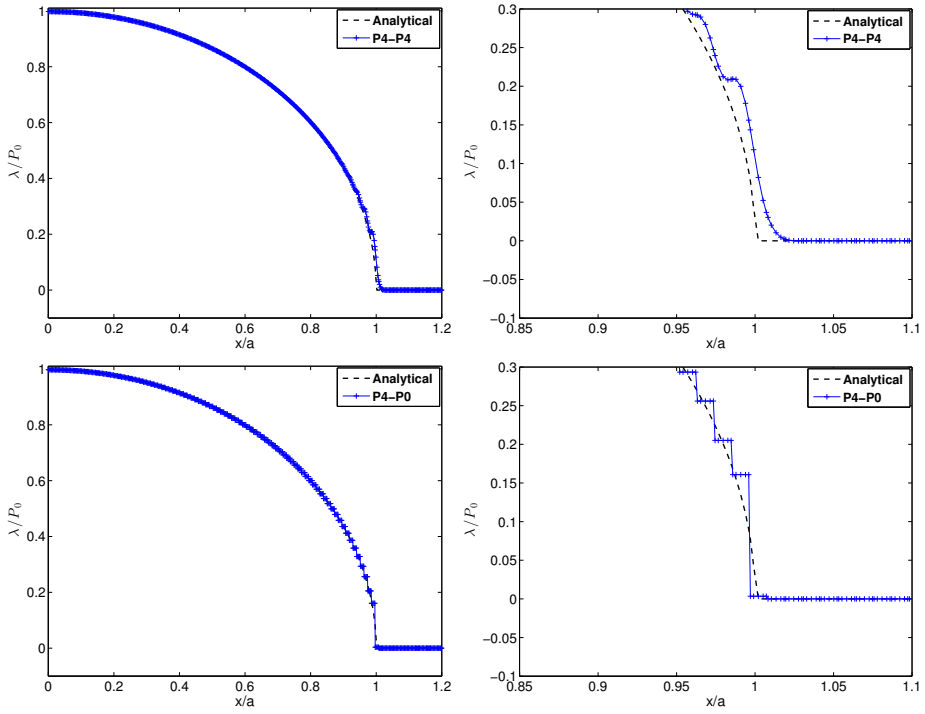

Figure 4.18: Test of Subsection 4.4.3 - First reference (top) and second reference (bottom) multiplier solution in comparison to the analytical one. The right pictures are zoom of the left ones in the transition active-inactive area.

4.5 Conclusion

In this chapter, numerical methods have been proposed for rigid-deformable contact. Even though it may appear as a simple contact problem case, as the approximation functions are defined on a unique mesh, different issues arise.

The proposed methods are mixed methods based on an augmented Lagrangian formulation. Thus a multiplier space has to be defined. Thanks to a relative similarity with the mortar context, same parity degree pairings have been used. And we have shown, they lead to optimal numerical methods.

The use of different degree pairings but also in a general context the gap definition itself require the use of a projection to project the gap in the multiplier space. We have shown that the use of a lumped L^2-projection has several advantages and do not affect the method optimality.

The most sensitive aspect to define is the discrete active region. The concept of element and control point approaches have been introduced. The

element approaches, in the ideal case, are suffering from a high numerical cost while in the approximate case, from a lack of robustness. The control point approaches are less suffering from this lack.

Chapter 5

Isogeometric methods for contact between two deformable bodies

Contents

5.1 Introduction

In this chapter, we propose isogeometric numerical methods for the simulation of the contact between two deformable bodies. In what follows,

we refer to this problem as deformable-deformable contact. The proposed methods are variationally consistent and based on the mortar methods defined in Chapters 2 and 3. Usually these kinds of methods are suffering from the pricey need of a segmentation process to manage their underlying integration issue. Those introduced in this chapter are designed to alleviate this process.

Leveraging by the high regularity of splines and the results presented in Chapters 2 and 3, we propose a Lagrange multiplier formulation solved via an active set strategy. We note that the methods could be cautiously extended to augmented Lagrangian formulations.

Let us recall that the semi-discrete weak Lagrange multiplier formulation, see (1.10), relative to the considered contact problem, see (1.5), is: find $(\boldsymbol{u_h},\, \lambda_h) \in V_{D,h} \times M_h^-$ such that

$$\begin{cases} a(\boldsymbol{u_h},\, \boldsymbol{v_h}) + b(\boldsymbol{v_h}, \lambda_h) = f(\boldsymbol{v_h}), & \forall \boldsymbol{v_h} \in V_{0,h}, \\ b(\boldsymbol{u_h},\, \lambda_h - \phi_h) \leq -g(\lambda_h - \phi_h), & \forall \phi_h \in M_h^-. \end{cases}$$

The outline of the chapter is the following. First, in Section 5.2, we complete the discrete definition of our methods. Then in Section 5.3, we detail the numerical strategies used to set the contact constraints. Finally, in Section 5.4, we illustrate the numerical properties of our methods.

5.2 Contact problem discretization

In this section, we set the remaining counterparts of the semi-discrete Lagrange multiplier formulation introduced in Equation (1.10).

5.2.1 Discrete multiplier spaces

The discrete Lagrange multiplier space M_h defined on $\Gamma_{C,S}$ has to be selected carefully to ensure the mixed method to be well posed, see, e.g., [13]. The deformable-deformable unilateral frictionless contact problem can be seen as a directional gluing problem between slave and master subdomains on the active region of contact. Thus some similarities exist with the mortar methods introduced in Chapters 2 and 3. In a mortar context, all the unknown components are glued, while in the frictionless contact context the gluing concerns only the direction of the normal of

contact. In the proposed methods, the primal variable is a vector in $\mathbb{R}^{d_u}$ while the multiplier is a scalar, i.e., in $\mathbb{R}$.

The different multiplier spaces are similar to those defined in Chapter 4, Section 4.2. We refer to this section for more details and herein just recall a synthesis about them in Figure 5.1.

For $V_{S,h}$ a push-forward of a NURBS space of degree p_S and :

- M_h a push-forward of a spline space of degree p_S,
- M_h a push-forward of a spline space of degree $p_S - 2$,
- and more generally, for a push-forward of a spline space of degree $p_S - 2k$ ($k \in \mathbb{N}$ and $k > 1$),

one can expect quantitative and qualitative results with the proposed contact methods. In the sense that some pairings will bring optimal results while others will lead to a slight lost in the convergence order.

Figure 5.1: Summary of the multiplier space choices.

5.2.2 Discrete active region of contact

It remains to define M_h^-, i.e., to give a discrete definition to the constraint dual cone which is related to the definition of the active/inactive discrete contact area. For this purpose, let us introduce the three different spaces:

$$
\begin{aligned}
M_{h,E}^- &= \{\phi_h \in M_h, \quad \phi_h \leq 0\}, \\
M_{h,W}^- &= \{\phi_h \in M_h, \quad \int_{\Gamma_{C,S}} \phi_h \; B_j \, \mathrm{ds} \leq 0, \quad \forall j \; = 1, \, ..., \, n_{M_h}\}, \\
M_{h,P}^- &= \{\phi_h \; = \sum_k \; \alpha_k \, B_k, \quad \alpha_k \leq 0, \quad \forall k \; = 1, \, ..., \, n_{M_h}\},
\end{aligned}
$$

referred respectively as the exact check, a weak check and a control point check of the constraints. The first choice requires a zero spline detection algorithm, and leads to define the active region as an area delimited by the zero(s) of a spline. It is similar to the element approach methods proposed in Chapter 4. While the two other choices consist in control value checks, and lead to define the active region as the support of the relative functions. In both cases, the number of coefficients to check is equal to the multiplier space dimension. They can thus be considered as a control point approach method as proposed in Chapter 4. The relative position of the three space

choices compared to the continuous dual cone is visible in Figure 5.2. In the presented methods, for numerical convenience reasons we consider the third choice, i.e., from now on the discrete dual cone is $M_{h,P}^{-}$.

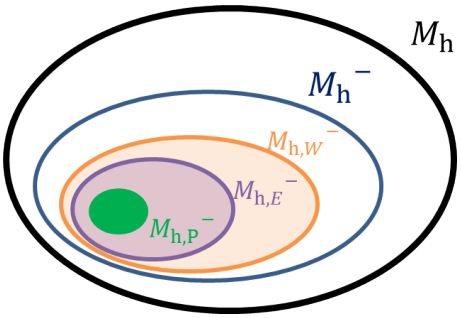

Figure 5.2: Relative positions of the introduced discrete dual cones in comparison to the continuous one.

5.3 Numerical strategies to set the contact constraints

In this section, we present the details of the active set strategy considered to solve our discrete deformable-deformable contact problem. We refer, e.g., to [57, 59] for other active set strategy applications.

5.3.1 Active set resolution strategy

In the proposed contact methods, the discrete dual cone involves a value check of each multiplier control variable. In an active set resolution strategy, one should define sets of active/inactive control variables in a unique space, here taken as the multiplier space. In a Lagrange multiplier formulation, the variables of interest are the multiplier λ and the gap g_N which involve three different approximation spaces. In order to determine the status of each multiplier control point, the gap should be projected in the multiplier space. This is done by the use of a lumped L^2-projection $\widetilde{\Pi}$, defined in Equation (3.2). This projection is known to induce a consistency error, thus we should manipulate it cautiously (see Chapter 3). In the way the projection is herein introduced in the methods, it turns out that this consistency error (which is in principle of order 1) does not affect the accuracy of our methods. We note that it was similarly observed for the methods defined in Chapters 3 and 4.

Once having the multiplier and gap approximated in the multiplier space, we define a status for each multiplier control point. Precisely, a control point is active either if its multiplier value is negative, i.e., there is a compression in that point, or if its gap value is negative, i.e., there is interpenetration in that point. Otherwise it is inactive. We recall for a sake of completion the set of all possible status cases in Figure 5.3. We note that due to the way the constraints are imposed by the numerical strategies, the cases (d), (e), (g) and (h) do not appear in the resolution process.

$\lambda_j < 0,$			$\lambda_j > 0,$			$\lambda_j = 0,$		
$(\widetilde{\Pi} g_N)_j = 0$	**Actif**	(a)	$(\widetilde{\Pi} g_N)_j = 0$	**Inactif**	(b)	$(\widetilde{\Pi} g_N)_j = 0$	**Inactif**	(c)
$(\widetilde{\Pi} g_N)_j > 0$	**Actif**	(d)	$(\widetilde{\Pi} g_N)_j > 0$	**Inactif**	(e)	$(\widetilde{\Pi} g_N)_j > 0$	**Inactif**	(f)
$(\widetilde{\Pi} g_N)_j < 0$	**Actif**	(g)	$(\widetilde{\Pi} g_N)_j < 0$	**Actif**	(h)	$(\widetilde{\Pi} g_N)_j < 0$	**Actif**	(i)

Figure 5.3: List of all the 9 possible control point status in a Lagrange multiplier formulation.

The active region of contact denoted ACT is defined as the support of the active multiplier control variables. We note that the set of active multiplier control variables is denoted CP_λ^{ACT} while the set of inactive ones CP_λ^{INA}. The discrete formulation of the considered contact problem, see (1.10), solved in an active set strategy is then written as: find $(\boldsymbol{u_h}, \lambda_h) \in V_{D,h} \times M_{h,P}^-$ such that

$$\begin{cases} a(\boldsymbol{u_h}, \boldsymbol{v_h}) + \displaystyle\int_{ACT} \lambda_h \, [\boldsymbol{v_h}] \; \mathrm{d}s = f(\boldsymbol{v_h}), & \forall \boldsymbol{v_h} \text{ in } V_{0,h}, \\ \displaystyle\int_{ACT} \phi_h \, [\boldsymbol{u_h}] \; \mathrm{d}s = -\int_{ACT} \phi_h \; g \; \mathrm{d}s, & \forall \phi_h \text{ in } M_{h,P}^-. \end{cases} \tag{5.1}$$

The constraints are checked on the multiplier control values $\lambda_j \, (j = 1, \ldots, n_{M_h})$ and the discrete gap control values $(\widetilde{\Pi} g_N)_j \, (j = 1, \ldots, n_{M_h})$. In Chapter 3, it has been shown that imposing weakly the L^2-projection of the gap equal to zero is equivalent to impose weakly the lumped L^2-projection of the gap equal to zero. So, once can check the constraints using the lumped L^2-projection of the gap while imposing weakly the gap equal to zero.

Active set strategy

(i) Initialise CP_λ^{ACT} and CP_λ^{INA}

(ii) Compute

$$\begin{bmatrix} K & B_{(\cdot,CP_\lambda^{ACT})} \\ B^*_{(CP_\lambda^{ACT},\cdot)} & 0_{(CP_\lambda^{ACT},CP_\lambda^{ACT})} \end{bmatrix} \begin{bmatrix} U \\ \Lambda_{(CP_\lambda^{ACT})} \end{bmatrix} = \begin{bmatrix} F \\ G_{(CP_\lambda^{ACT})} \end{bmatrix}$$

(iii) Check convergence, i.e.,: CP_λ^{ACT} and CP_λ^{INA} stable

(iv) Update CP_λ^{ACT} and CP_λ^{INA} and go to (ii) until convergence is reached

with U the displacement vector, Λ the multiplier vector,
K the stiffness matrix, F the primal right hand side,
G the multiplier right hand side,
B and B^* the matrices associated to the mixed bilinear form.
B and B^* are split into a slave B^S, resp. B^{*S}, and a master B^M, resp. B^{*M}, counterparts as $B = \begin{bmatrix} B^S \\ B^M \end{bmatrix}$, resp. $B^* = \begin{bmatrix} B^{*S} \\ B^{*M} \end{bmatrix}$, with

$$\begin{aligned}
B^S_{ij} &= \int_{ACT} B^\lambda_j(\boldsymbol{x^S})\, \boldsymbol{n_M}(\overline{\boldsymbol{x}}^{\boldsymbol{M}}) \cdot \boldsymbol{B^S_i}(\boldsymbol{x^S})\ \mathrm{d}s, \\
B^{*S}_{ij} &= \int_{ACT} B^\lambda_i(\boldsymbol{x^S})\, \boldsymbol{n_M}(\overline{\boldsymbol{x}}^{\boldsymbol{M}}) \cdot \boldsymbol{B^S_j}(\boldsymbol{x^S})\ \mathrm{d}s, \\
B^M_{ij} &= -\int_{ACT} B^\lambda_j(\boldsymbol{x^S})\, \boldsymbol{n_M}(\overline{\boldsymbol{x}}^{\boldsymbol{M}}) \cdot \boldsymbol{B^M_i}(\overline{\boldsymbol{x}}^{\boldsymbol{M}})\, \mathrm{d}s, \\
B^{*M}_{ij} &= -\int_{ACT} B^\lambda_i(\boldsymbol{x^S})\, \boldsymbol{n_M}(\overline{\boldsymbol{x}}^{\boldsymbol{M}}) \cdot \boldsymbol{B^M_j}(\overline{\boldsymbol{x}}^{\boldsymbol{M}})\, \mathrm{d}s.
\end{aligned}$$

Figure 5.4: Details of the active set strategy algorithm.

In Figure 5.4, we give the active set strategy implemented to solve the problem (5.1) and its matrix formulation. As it is visible, a distinction between B and B^* is done as B^* is not always B^T. We highlight that under the small displacement-deformation assumptions, the use of a control point approach allows to compute the matrices once. Then, at each step to assemble in the global matrix only the necessary blocks as the integrals to approximate never change while getting the solution. In the proposed methods, the symmetry of the global matrix is depending on the integral evaluation method.

5.3.2 Integral evaluation strategy

As for mortar methods, an issue arises from the mixed bilinear form integral evaluations due to the fact one of them contains a product of functions which are defined on different meshes. The straightforward way to evaluate this integral consists in the use of a quadrature rule based on a merged mesh. However, as it has already been commented, the construction of this auxiliary mesh is from a computational point of view

complex, see, e.g., [86, 95, 96, 53, 42]. And we highlight that for general contact problems, this auxiliary mesh should be built at each geometry update. To alleviate it, it has been seen very appealing to use a high order quadrature rule based on an existing mesh. From the finite element literature, see, e.g., [23, 81] as well as the isogeometric mortar results, see Chapter 3, a convenient integration approach is retained. The proposed contact methods are based on this later one.

In the following, we introduce with more details our considered integration approach and we will compare it with an approach referred as slave integration approach, see, e.g., [48, 108, 37]. We recall that for a slave point $\boldsymbol{x}^{\boldsymbol{S}}$, we define its projected point(s) $\overline{\boldsymbol{x}}^{\boldsymbol{M}}$ on the master, see Chapter 1 and the Appendix. Similarly, considering a master point $\boldsymbol{x}^{\boldsymbol{M}}$, we associate it to a slave point we denote $\tilde{\boldsymbol{x}}^{\boldsymbol{S}}$. The way it is obtained is discussed later on. Let us denote a quadrature rule based on the boundary mesh of the slave domain as $\sum_S$ and respectively $\sum_M$ a quadrature rule based on the boundary mesh of the master domain. We note that both methods introduce an error in the discrete solution as they do not consist in exact integration approaches.

The slave integration approach consists in an evaluation of all the integrals with the slave integration rule, i.e,

$$\int_{ACT} B_j^\lambda(\boldsymbol{x}^{\boldsymbol{S}})\ \boldsymbol{n_M}(\overline{\boldsymbol{x}}^{\boldsymbol{M}}) \cdot \boldsymbol{B_i^S}(\boldsymbol{x}^{\boldsymbol{S}})\ \mathrm{d}s = \sum\nolimits_S{}^{ACT} B_j^\lambda(\boldsymbol{x}^{\boldsymbol{S}})\ \boldsymbol{n_M}(\overline{\boldsymbol{x}}^{\boldsymbol{M}}) \cdot \boldsymbol{B_i^S}(\boldsymbol{x}^{\boldsymbol{S}}),$$

$$\int_{ACT} B_j^\lambda(\boldsymbol{x}^{\boldsymbol{S}})\ \boldsymbol{n_M}(\overline{\boldsymbol{x}}^{\boldsymbol{M}}) \cdot \boldsymbol{B_i^M}(\overline{\boldsymbol{x}}^{\boldsymbol{M}})\ \mathrm{d}s = \sum\nolimits_S{}^{ACT} B_j^\lambda(\boldsymbol{x}^{\boldsymbol{S}})\ \boldsymbol{n_M}(\overline{\boldsymbol{x}}^{\boldsymbol{M}}) \cdot \boldsymbol{B_i^M}(\overline{\boldsymbol{x}}^{\boldsymbol{M}}),$$

$$\int_{ACT} B_i^\lambda(\boldsymbol{x}^{\boldsymbol{S}})\ \boldsymbol{n_M}(\overline{\boldsymbol{x}}^{\boldsymbol{M}}) \cdot \boldsymbol{B_j^S}(\boldsymbol{x}^{\boldsymbol{S}})\ \mathrm{d}s = \sum\nolimits_S{}^{ACT} B_i^\lambda(\boldsymbol{x}^{\boldsymbol{S}})\ \boldsymbol{n_M}(\overline{\boldsymbol{x}}^{\boldsymbol{M}}) \cdot \boldsymbol{B_j^S}(\boldsymbol{x}^{\boldsymbol{S}}),$$

$$\int_{ACT} B_i^\lambda(\boldsymbol{x}^{\boldsymbol{S}})\ \boldsymbol{n_M}(\overline{\boldsymbol{x}}^{\boldsymbol{M}}) \cdot \boldsymbol{B_j^M}(\overline{\boldsymbol{x}}^{\boldsymbol{M}})\ \mathrm{d}s = \sum\nolimits_S{}^{ACT} B_i^\lambda(\boldsymbol{x}^{\boldsymbol{S}})\ \boldsymbol{n_M}(\overline{\boldsymbol{x}}^{\boldsymbol{M}}) \cdot \boldsymbol{B_j^M}(\overline{\boldsymbol{x}}^{\boldsymbol{M}}),$$

which leads to a symmetric global matrix.

While the mixed integration approach consists in an evaluation of each encountered integral with the quadrature rule able to catch the reduce line of smoothness of the trial functions. It ensures at least a proper approximation of these later functions on which the properties of the variational formulation is based. The integrals are evaluated as:

$$\int_{ACT} B_j^{\lambda}(\boldsymbol{x^S})\ \boldsymbol{n_M}(\overline{\boldsymbol{x}}^{\boldsymbol{M}}) \cdot \boldsymbol{B_i^S}(\boldsymbol{x^S})\ \mathrm{d}s = \sum\nolimits_S^{ACT} B_j^{\lambda}(\boldsymbol{x^S})\ \boldsymbol{n_M}(\overline{\boldsymbol{x}}^{\boldsymbol{M}}) \cdot \boldsymbol{B_i^S}(\boldsymbol{x^S}),$$

$$\int_{ACT} B_j^{\lambda}(\boldsymbol{x^S})\ \boldsymbol{n_M}(\overline{\boldsymbol{x}}^{\boldsymbol{M}}) \cdot \boldsymbol{B_i^M}(\overline{\boldsymbol{x}}^{\boldsymbol{M}})\ \mathrm{d}s = \sum\nolimits_M^{ACT} B_j^{\lambda}(\tilde{\boldsymbol{x}}^{\boldsymbol{S}})\ \boldsymbol{n_M}(\boldsymbol{x}^{\boldsymbol{M}}) \cdot \boldsymbol{B_i^M}(\boldsymbol{x}^{\boldsymbol{M}}),$$

$$\int_{ACT} B_i^{\lambda}(\boldsymbol{x^S})\ \boldsymbol{n_M}(\overline{\boldsymbol{x}}^{\boldsymbol{M}}) \cdot \boldsymbol{B_j^S}(\boldsymbol{x^S})\ \mathrm{d}s = \sum\nolimits_S^{ACT} B_i^{\lambda}(\boldsymbol{x^S})\ \boldsymbol{n_M}(\overline{\boldsymbol{x}}^{\boldsymbol{M}}) \cdot \boldsymbol{B_j^S}(\boldsymbol{x^S}),$$

$$\int_{ACT} B_i^{\lambda}(\boldsymbol{x^S})\ \boldsymbol{n_M}(\overline{\boldsymbol{x}}^{\boldsymbol{M}}) \cdot \boldsymbol{B_j^M}(\overline{\boldsymbol{x}}^{\boldsymbol{M}})\ \mathrm{d}s = \sum\nolimits_S^{ACT} B_i^{\lambda}(\boldsymbol{x^S})\ \boldsymbol{n_M}(\overline{\boldsymbol{x}}^{\boldsymbol{M}}) \cdot \boldsymbol{B_j^M}(\overline{\boldsymbol{x}}^{\boldsymbol{M}}),$$

which leads to a non-symmetric global matrix. The saddle point problem related to this method is not anymore a symmetric one and it corresponds to a Petrov-Galerkin approach in the primal formulation. From the theoretical point of view, even the well posedness of this problem is an open question.

As already observed in the mortar context in Chapter 3, methods involving the mixed integration approach remain optimal while lack of optimality is observed for those involving the slave integration one.

The need of the master quadrature rule in the mixed integration approach requires that given a master point we associate it to a slave point. In order to maintain a unique normal of contact, i.e., the master normal, this point is not projected on the slave domain but it is subjecting to a ray-tracing to the slave domain, see Figure 5.5 and the Appendix. I.e., taking a master point it is moved to the slave boundary along the direction of its master normal. Our ray-tracing problem has a unique solution for each master point in the case it exists thanks to the smoothness of splines.

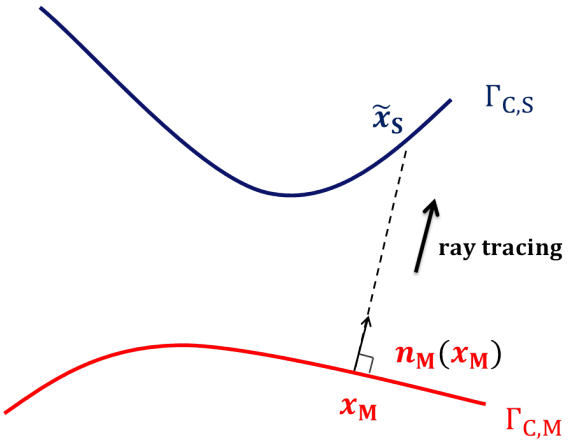

Figure 5.5: Ray-tracing of a master point on the slave.

In the small displacement-deformation context, we assume that both mappings are quite similar in the neighbourhood of the active contact area. It is warranting a good definition of the projection and ray-tracing problems for each slave point, resp. master point, in the crucial parts of the potential area of contact. Although the high smoothness of splines helps a lot, we note that in the general cases, one will face to cases of non-uniqueness of projected point (taking a slave point), as to cases of non-existence of projected point (taking a slave point) or ray-traced point (taking a master point). Theses issues are not covered by this work. We highlight that in the general context, initial shape assumptions on the geometry as regularity on the mapping may not be enough to avoid them as the geometries are changing at each resolution step.

5.4 Numerical results

In this section, we discuss numerical results obtained with methods involving both integration approaches. We precise that in the examples, we use a Gaussian quadrature rule. The quadrature point number taken is the one we would have used with a quadrature rule defined on the merged mesh to integrate same degree pairings, and thus a little higher than necessary to integrate different degree pairings. We start to study a contact test on which we check the transmission of a constant pressure. Then, we consider a high regularity test setting with full and partial contact. Finally, we consider a more general test with a curved boundary.

5.4.1 A patch test: transmission of a constant pressure

As contact patch test, we considered the classical problem of the transmission of a constant pressure introduced in [103] and used in the same setting as in [44]. We focus on the contact between two squares in 2D, see the first picture of Figure 5.6. The upper subdomain is chosen as the slave, while the other one as the master. Both subdomains have the same material properties with $E = 1$ and $\nu = 0.3$.

A vertical homogeneous Dirichlet condition is applied on the bottom surface of the master body. A horizontal homogeneous Dirichlet condition is applied on the left surface of the master and slave bodies. A Neumann condition, i.e, a pressure is applied on the top surface of the slave body.

This latter is such that the horizontal component is equal to zero while the vertical component is a negative constant equal to -0.00125, see the first picture of Figure 5.6. The potential slave contact area is its bottom boundary, i.e., the one of equation $y = 0$ while the potential master contact area is its top boundary, i.e., the one of equation $y = 0$. Thus the initial gap is here equal to zero. These boundary conditions are such that all the potential area of contact is active, and we expect a constant stress state as analytical solution.

The problem is solved using the methods previously introduced with either the slave integration or the mixed integration approaches on different mesh configurations. Conforming and non-conforming meshes are considered, and we note that in the case the meshes are conforming both integration approaches are equivalent. In the non-conforming case, the meshes are chosen such that they are sharing no line at any refinement step and such that they have the same number of elements, see, e.g., the right picture in Figure 5.6. We highlight that for deformable-deformable contact problems a good description of the solution in both subdomains is of interest, which justifies the use of quite similar slave and master mesh sizes.

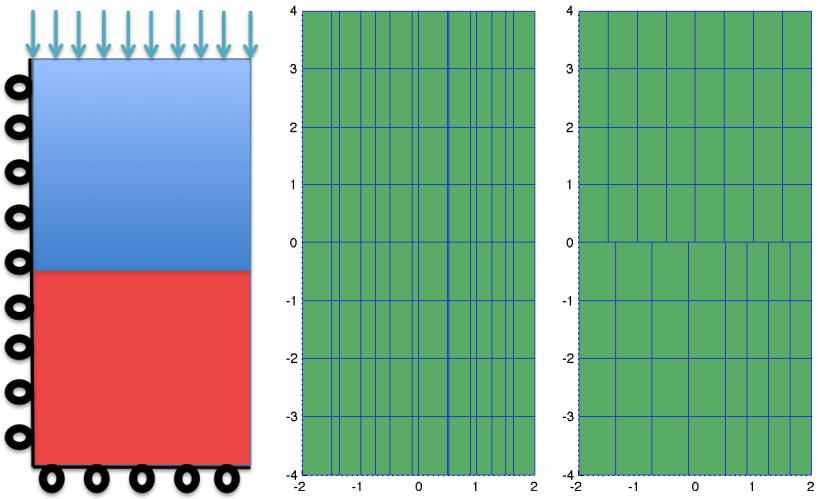

Figure 5.6: Test of Subsection 5.4.1 - Patch test setting (left). Conforming (middle) and non-conforming (right) mesh configurations at refinement level 1.

In Figures 5.7 and 5.8, we show the repartition of the stress σ_{yy} for two different mesh cases. On the active region of contact, σ_{yy} corresponds to the contact normal stress. The results show that the slave integration approach, as it is already known, is not passing the patch test, see [47].

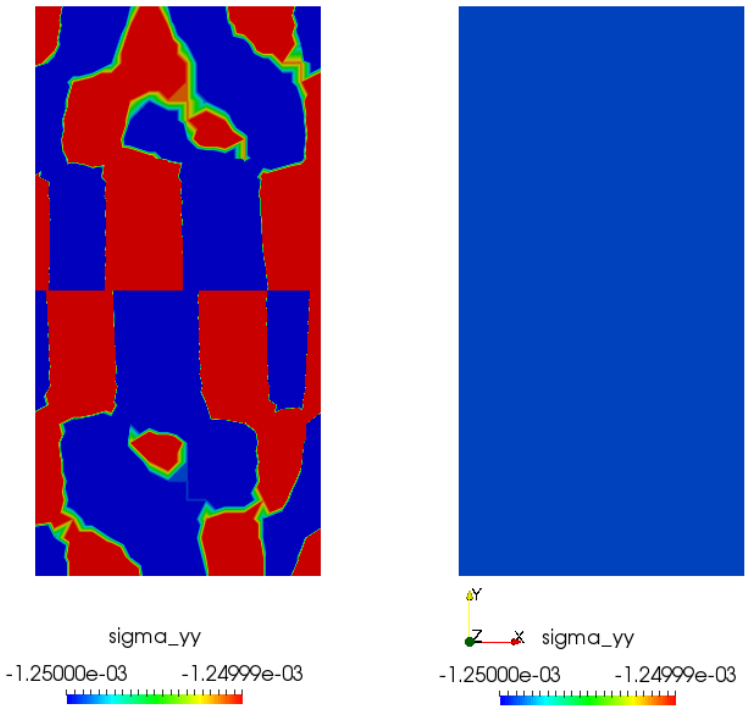

Figure 5.7: Test of Subsection 5.4.1 - Repartition of σ_{yy} for non-conforming meshes with 4×4 elements (refinement level 0) for each subdomain and the geometry, displacement and multiplier approximation spaces are of degree 2. On the left, obtained with the slave integration approach while on the right with the mixed integration approach.

Refining and increasing the number of quadrature points to compensate the approximate quadrature rule allow to improve the approximation of the solution, although some spurious oscillations still remain in the stress repartition, see Figures 5.7 and 5.8. On the contrary, the proposed methods with the mixed integration approach are passing the patch test to the machine precision and this also for coarse mesh cases.

Moreover we have led an error study to measure precisely the deviation induced by the approximate quadrature rule in each approach. This error study has been done on a family of meshes uniformly refined starting from a initial configuration, see the refinement level 1 in Figure 5.6 for the non-conforming (right picture) and conforming (middle picture) mesh cases. As reference solution, a numerical solution obtained with fine conforming meshes is taken: each mesh contains 255×64 elements and the geometry, displacement and multiplier approximation spaces are of degree 4. Note that the multiplier error is computed compared to the analytical

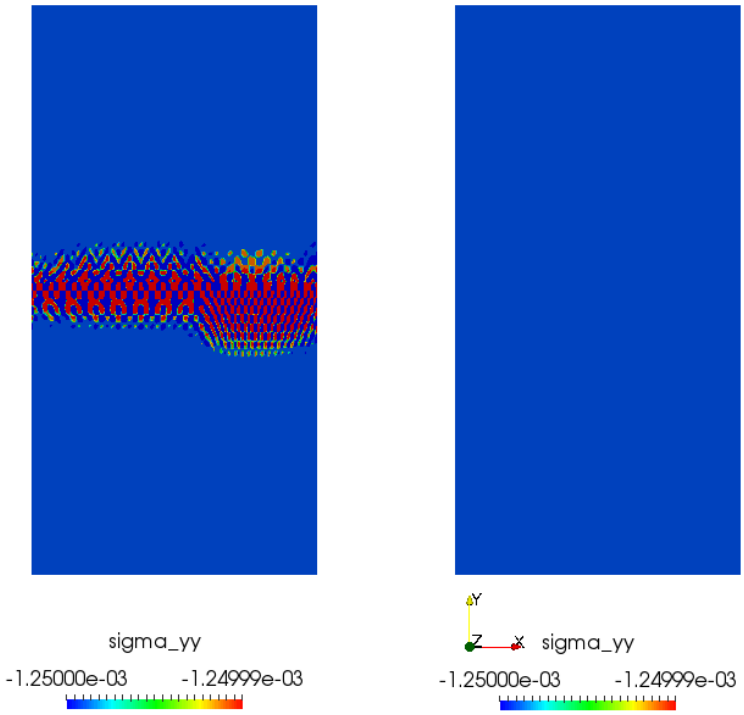

Figure 5.8: Test of Subsection 5.4.1 - Repartition of σ_{yy} for non-conforming meshes with 64×64 elements (refinement level 4) for each subdomain and the geometry, displacement and multiplier approximation spaces are of degree 2. On the left, obtained with the slave integration approach while on the right with the mixed integration approach.

solution.

In Figure 5.9, we plot some V primal and L^2 multiplier errors for the pairings $P3 - P3$ and $P3 - P1$. As it is clearly visible, we have observed that the proposed methods with the mixed integration approach are able to catch even for coarse meshes the patch test solution to the machine precision, while the methods with the slave integration approach are not. Although, we precise that the V primal error relative to the slave integration approach has the optimal order expected from the theory due to the low regularity of the contact problem, while we note that the L^2 multiplier error has a even lower order. It emphasises that the multiplier is more affected than the primal variable by the integral approximation done with the slave integration approach, as already seen in the mortar context, see Chapter 3.

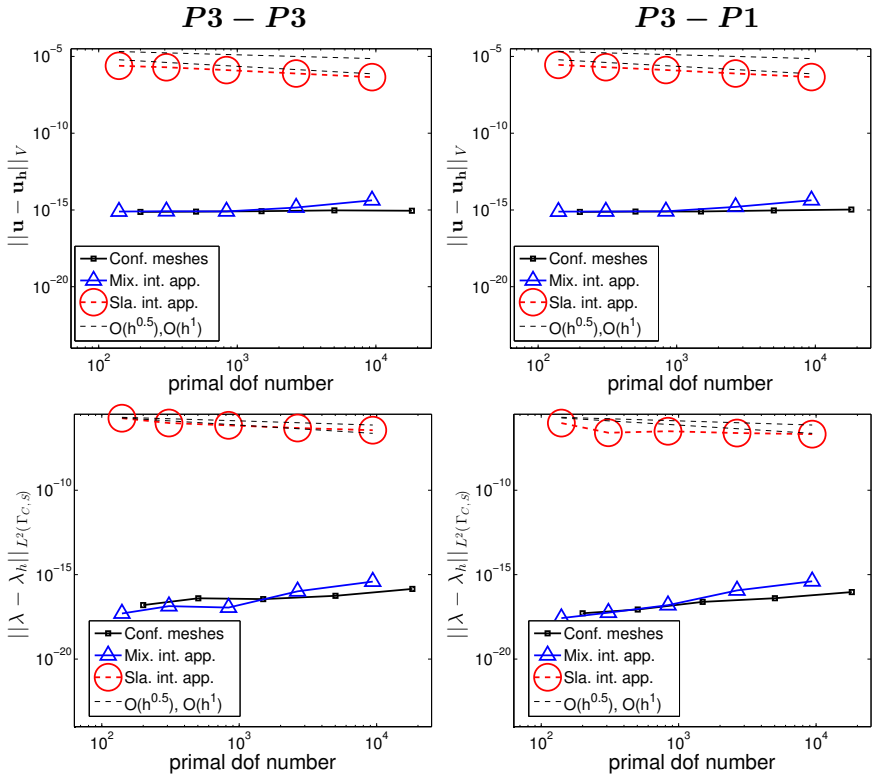

Figure 5.9: Test of Subsection 5.4.1 - V primal (top) and L^2 dual (bottom) error curves for the pairings $P3 - P3$ (left) and $P3 - P1$ (right). Obtained with the slave integration approach (circles), the mixed integration approach (triangles) and an exact integration approach, i.e., defined on conforming meshes (squares).

5.4.2 Simple contact problem: full versus partial active contact area

We considered two different settings of a contact problem with the highest possible regularity, i.e., about $\frac{3}{2}$ in V primal norm and in $H^{-\frac{1}{2}}$ dual norm, see, e.g., [89]. The first one has been tailored to be a full contact problem, i.e., to have for active region of contact all the potential one, while the second one only a part. Two rectangles with same material properties may enter in contact with $E = 1$ and $\nu = 0.3$, see the first picture of Figure 5.10. The upper subdomain is chosen as the slave, the other one as the master. A homogeneous Dirichlet condition is applied on the bottom surface of the master domain, i.e., this surface is clamped. A Dirichlet condition is applied on the top surface of the slave domain. This latter is such that the horizontal component is equal to zero while the vertical component is negative. More precisely, it is a B-Spline function of degree $p = 2$ with maximum value at the point ($x = 0$, $y = 0$). On the second line of

Figure 5.10 in the left picture, it is plotted for the first test and in the right for the second one. The potential slave contact area is its bottom boundary, i.e., the one of equation $y = 0$ while the potential master contact area is its top boundary, i.e., the one of equation $y = 0$. Thus the initial gap is here equal to zero. The problems are solved using the methods introduced above with either the slave integration or the mixed integration approach on different mesh configurations. We led error studies to understand the deviation induced by the approximate quadrature rules.

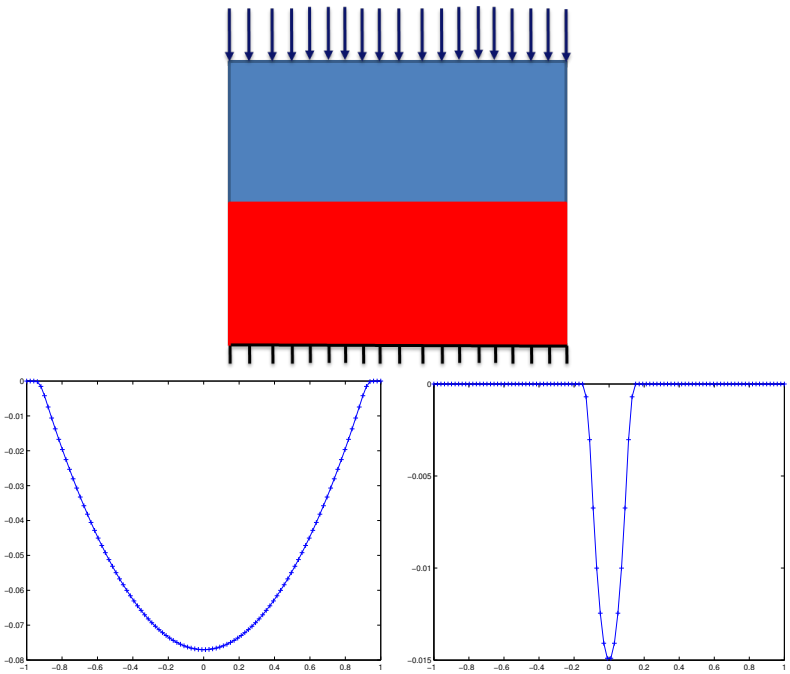

Figure 5.10: Test of Subsection 5.4.2 - Test setting (top). Vertical component of the Dirichlet condition applied on the top slave surface for the full contact (left) and partial one (right).

Full contact Regarding the full contact test, we have done two different error studies. They are based on two mesh family cases referred as mesh cases 1 and 2, visible in Figure 5.11. In the mesh case 1, the slave and master meshes have the same number of elements. While in the mesh case 2, the master mesh is finer than the slave mesh. As reference solution, a numerical solution obtained with fine conforming meshes is taken: it contains 255×32 (mesh case 1) and 255×64 (mesh case 2) elements for each domain and the geometry, displacement and multiplier approximation spaces are of degree 4.

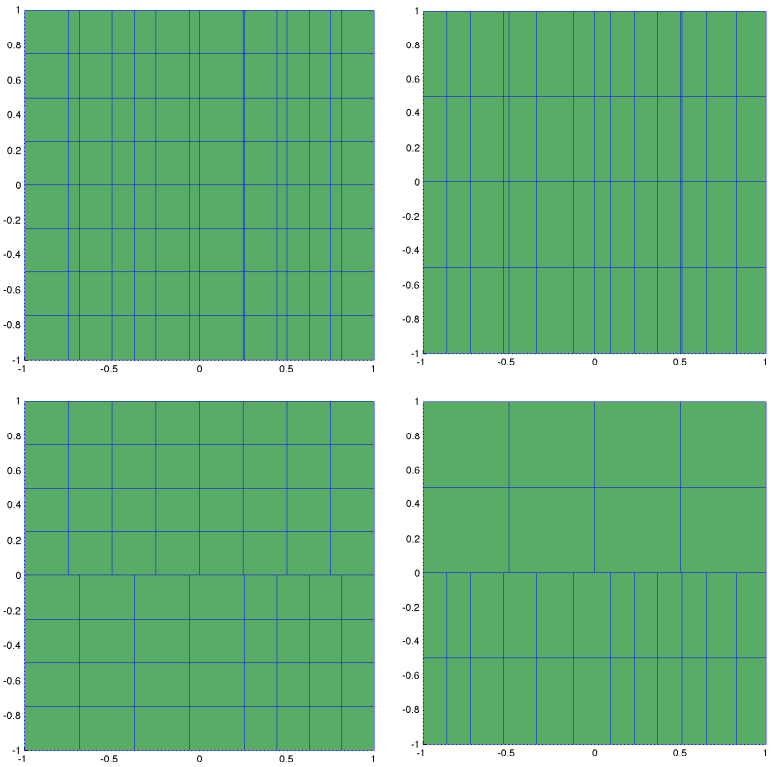

Figure 5.11: Test of Subsection 5.4.2 - Conforming (top) and non-conforming (bottom) mesh configurations at refinement level 2. Left: mesh case 1. Right: mesh case 2.

For this test, no impact on the primal variable is observed in V and L^2 norms with both integration approaches while some are observed on the multiplier. In Figure 5.12, we plot the L^2 multiplier error for same degree pairings for $p = 1$ to $p = 3$ and in Figure 5.13 for the different degree pairings $P2 - P0$ and $P3 - P1$. In the case same degree pairings are used, the multiplier is not affected by the approximate quadrature rules when the mixed integration approach is involved while it is when the slave approach is involved, see Figure 5.12. We note that increasing the spline space degree allows to observe this disturbance at a finer refinement level. For the different degree pairing, on the considered refinement levels, no impact on the multiplier is observed with both integration approaches. We note that even in the second mesh case for which more reduced lines of smoothness are missed by the slave integration approach.

Partial contact Regarding the partial contact, as reference solution, a numerical solution obtained with fine conforming meshes is taken: it contains 511×128 elements for each subdomain and the geometry, displacement

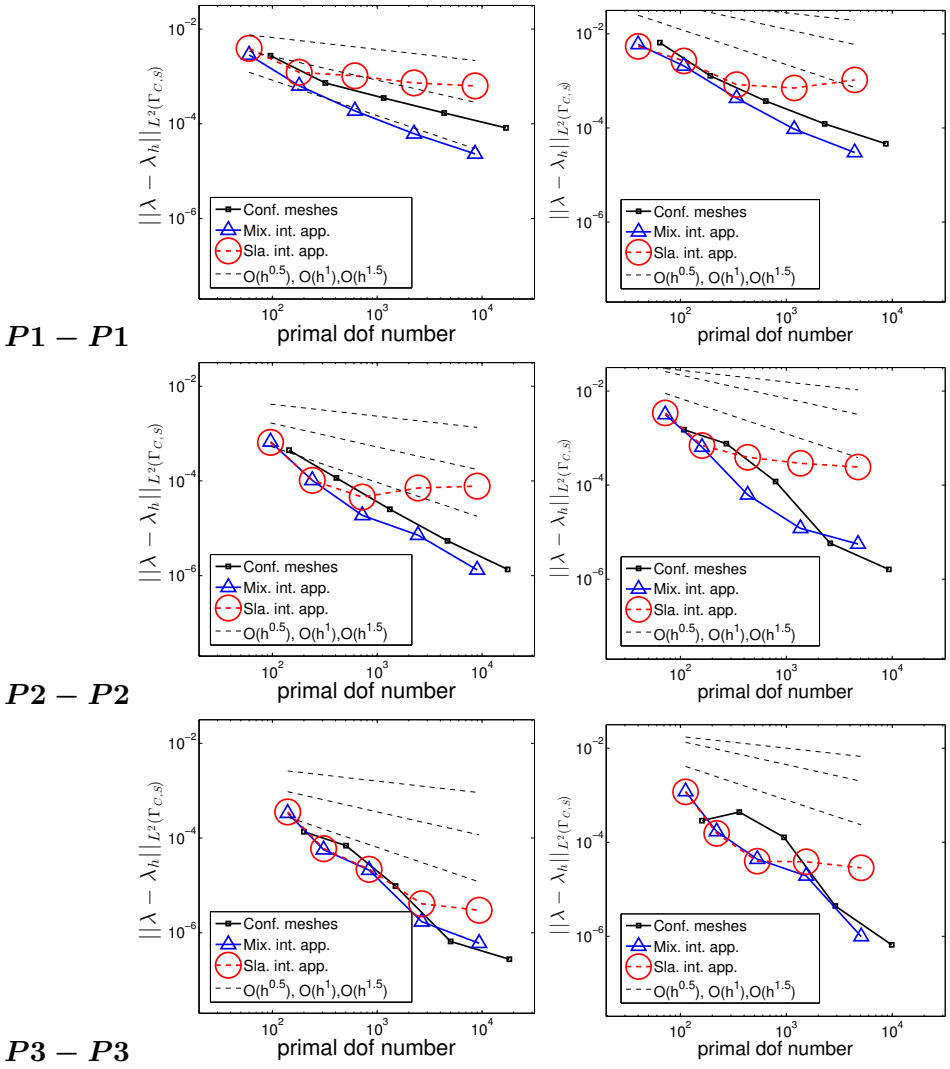

Figure 5.12: Test of Subsection 5.4.2 - Full contact - L^2 dual error curves. Top to bottom: different pairing results: $P1-P1$, $P2-P2$, $P3-P3$. Left: mesh case 1. Right: mesh case 2. Obtained with the slave integration approach (circles), the mixed integration approach (triangles) and an exact integration approach, i.e., defined on conforming meshes (squares).

and multiplier approximation spaces are of degree 4. The refinement level 2 is visible in the left picture of Figure 5.11.

For this test also, no deviation from the exact integration case is observed in V and L^2 norms with both integration approaches while some are observed on the multiplier. In Figure 5.14, we give the V primal and L^2 multiplier errors for the pairings $P1-P1$ and $P2-P0$. It is clearly visible that the primal variable is not perturbed by both of the approximate integration rules, leading to methods of order 1 in V primal norm for the $P1-P1$ pairing and 1.5 for the $P2-P0$ pairing. Regarding the multiplier,

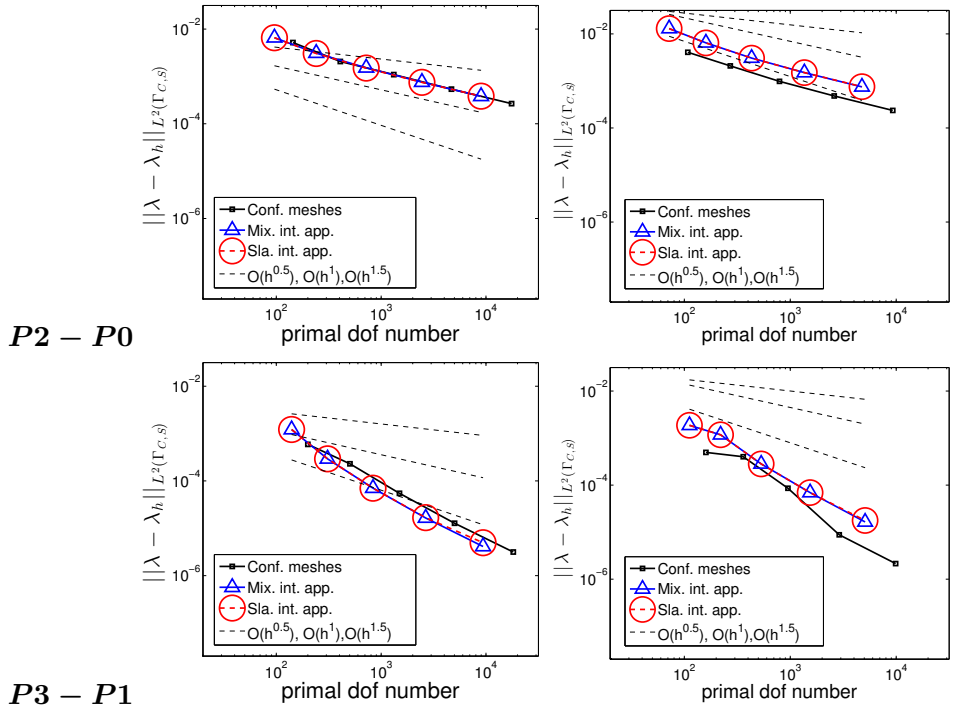

Figure 5.13: Test of Subsection 5.4.2 - Full contact - L^2 dual error curves for the pairing $P2 - P0$ (top) and $P3 - P1$ (bottom). Left: mesh case 1. Right: mesh case 2. Obtained with the slave integration approach (circles), the mixed integration approach (triangles) and an exact integration approach, i.e., defined on conforming meshes (squares).

some differences are observed. While the mixed integration approach leads to optimal results, the slave integration approach not always, see Figure 5.14.

We note that for this second test, as the active region of contact is more limited than in the first test, the impact of an approximate integration approach on the solution is less measurable on the mesh step range we consider.

Moreover some steps are visible in the evolution of the multiplier errors, typical to contact problem error evolution. We note that it could be due to the fact the reference is a computed solution and thus contained some approximations, especially in a key part, i.e., the active region of contact. It allows us to point out a drawback of the methods relative to the use of splines. It regards the active region of contact definition, defined as the support of all the active functions. A function is determined active according to the sign check of the projected gap and multiplier values. Even though the control point values are still not equal to zero, the multiplier

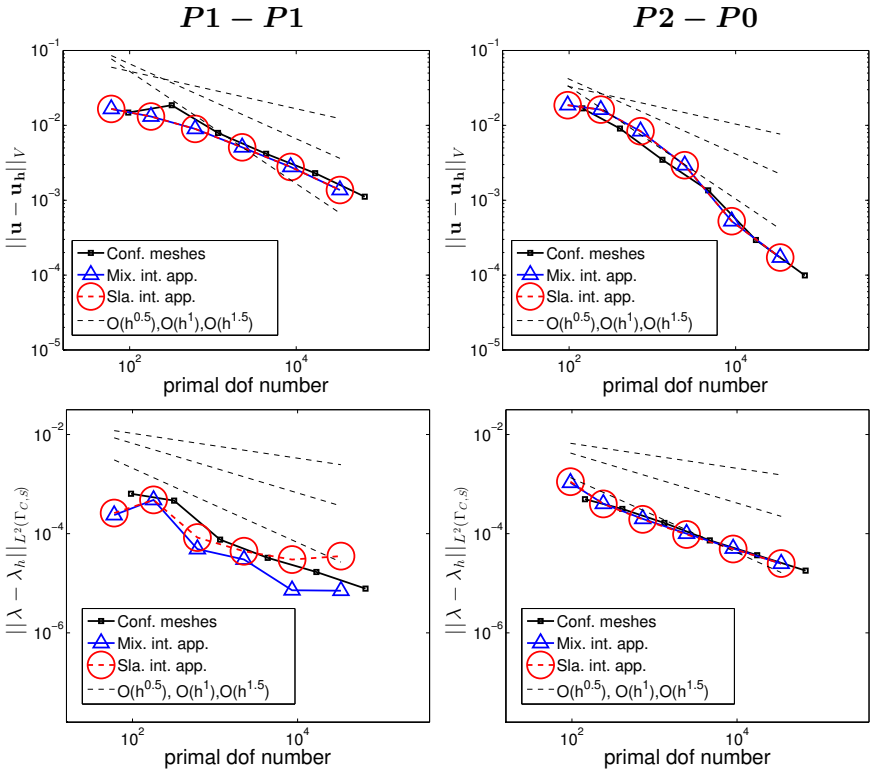

Figure 5.14: Test of Subsection 5.4.2 - Partial contact - V primal (top) and L^2 multiplier (bottom) error curves for the pairings $P1 - P1$ (left) and $P2 - P0$ (right). Obtained with the slave integration approach (circles), the mixed integration approach (triangles) and an exact integration approach, i.e., defined on conforming meshes (squares).

and the gap, being approximated by spline spaces could be. Thus, there is no insurance that the algorithm stops for the highest quality contact solution approximation. Unfortunately there is no possibility of improving it without destroying the necessary concordance between the check and the imposition of the constraints related to the discrete dual cone definition.

5.4.3 A more general contact problem

As more general test, we consider the contact between two elastic bodies with one which has a circular boundary as it is visible in Figure 5.15. The two meshes do not match, see the right picture of Figure 5.15, as in a general contact problem. We note that we consider meshes which are more refined close to the potential area of contact to improve the accuracy on the effective region of contact. Indeed, we try to limit the add of some unnecessary degrees of freedom while refining due to the tensor product structure of classical NURBS. The upper subdomain is chosen as the slave, while the other one as the master. Both subdomains have the same material

properties with $E = 1$ and $\nu = 0.3$. A homogeneous Dirichlet condition is applied on the bottom surface of the master body, i.e., this surface is clamped. A Dirichlet condition, i.e., a displacement is imposed on the top surface of the slave body. This latter is such that the horizontal component is equal to zero while the vertical component is negative (constant value equal to -0.05). The potential slave contact area is its bottom boundary, i.e., the circular one. The potential master contact area is its top boundary, i.e., the one of equation $y = 0$. The initial gap is here not equal to zero. We note that the boundary conditions are such that only a part of the potential area of contact is active, see Figure 5.15 and a solution in Figure 5.16, although we do not have the analytical solution.

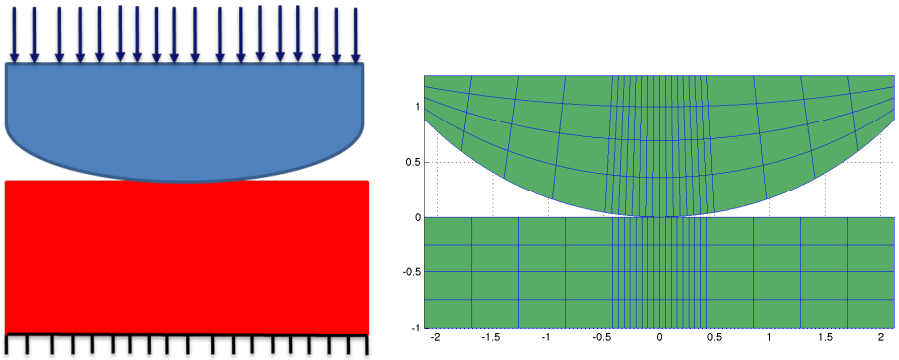

Figure 5.15: Test of Subsection 5.4.3 - Problem setting (left) and mesh configuration at refinement level 1 (right).

The problem is solved using the presented methods with both integration approaches on different mesh configurations. We led an error study. As reference solution, a numerical solution obtained with a mixed integration approach with fine meshes is taken: the mesh contains 384×64 elements for each subdomain and the geometry, displacement and multiplier approximation spaces are of degree 4. We point out that for this test, the reference solution could not be obtained within a reasonable computational cost for conforming meshes.

In Figure 5.17, we plot the V and L^2 primal and L^2 multiplier error curves for the pairings $P3 - P3$ and $P3 - P1$. As it is visible, the V primal error evolution remains of optimal order with the methods involving the mixed integration approach while some perturbations start to be visible

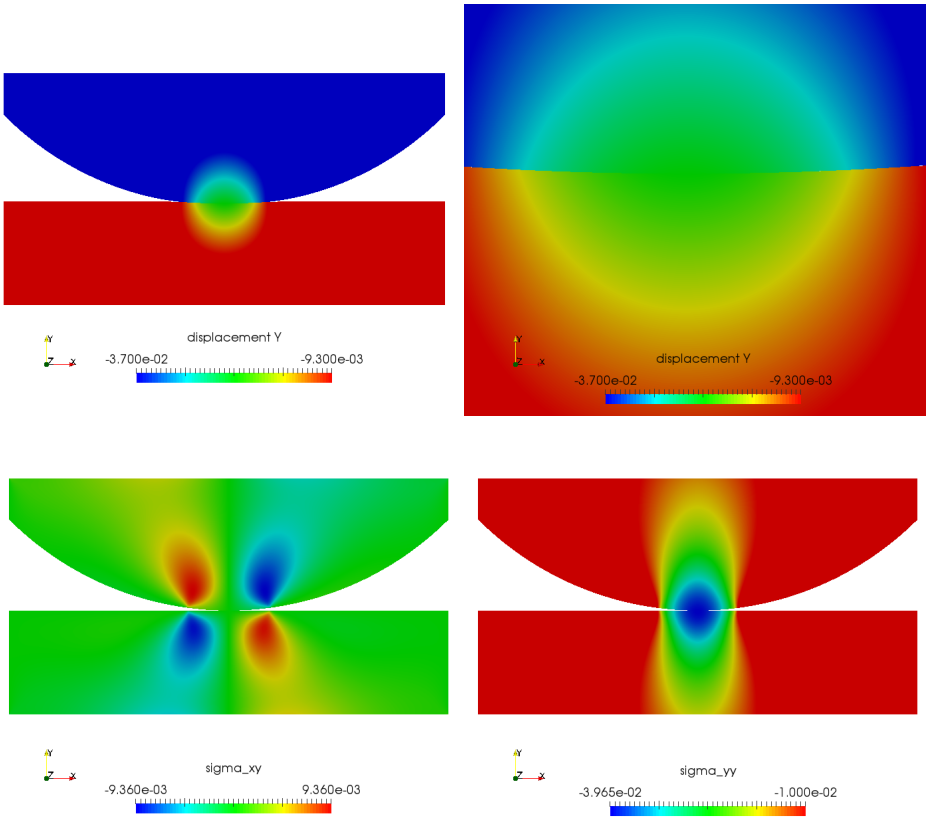

Figure 5.16: Test of Subsection 5.4.3 - Top: vertical displacement (the right picture is a zoom of the left one). Bottom: two stress repartitions (left: σ_{xy}, right: σ_{yy}).

on fine mesh cases with the slave integration approach. Regarding the L^2 primal error, it is of optimal order with the methods using the mixed integration approach while it is not the case at all for those using the slave integration approach. For this test, a serious lost of optimality arrives also for coarse meshes. Regarding the dual error, with both integration approaches the results are optimal up to a certain refinement level. Indeed, for the slave integration, after a certain level, it is not anymore optimal. We highlight that thus as not usually observed, for this test, the primal variable is first affected by the quadrature approximation done with the slave integration approach, although this disturbance is caught later in V primal norm than in L^2.

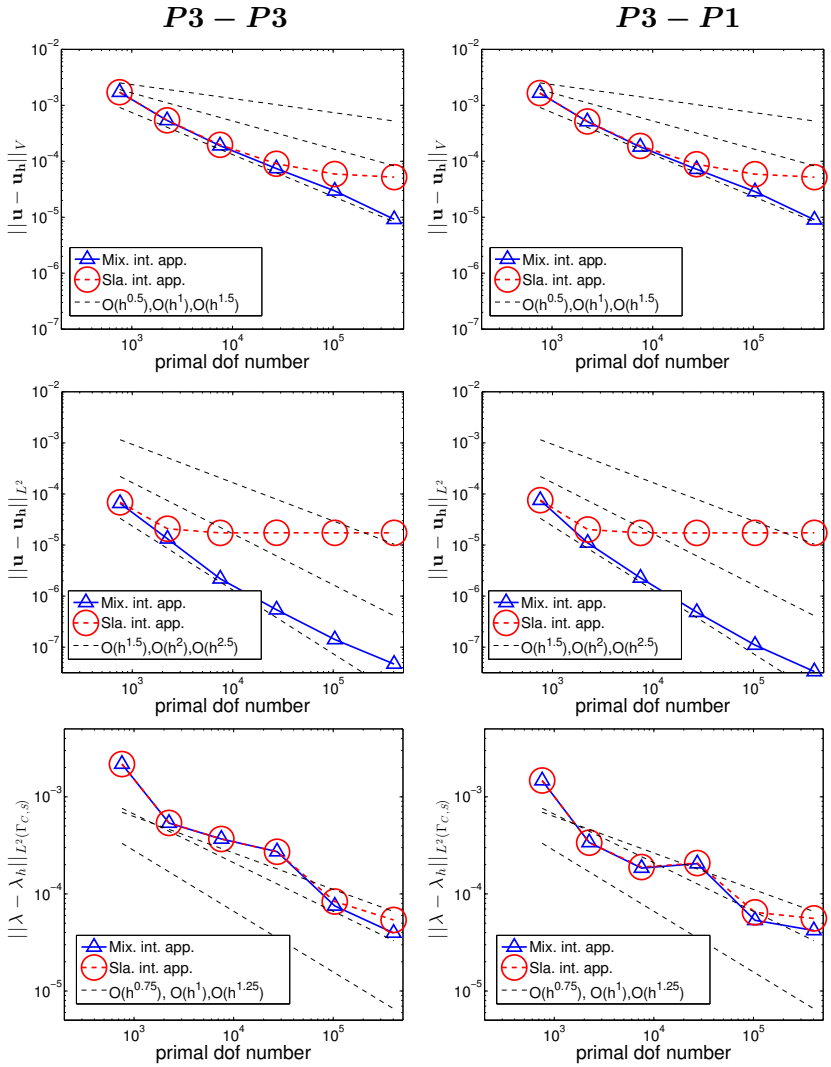

Figure 5.17: Test of Subsection 5.4.3 - V primal (top), L^2 primal (middle) and L^2 multiplier (bottom) error curves for the pairings $P3-P3$ (left) and $P3-P1$ (right) obtained with the slave integration approach (circles) and the mixed integration approach (triangles).

5.5 Conclusion

In this chapter, isogeometric methods were introduced to solve a linear frictionless deformable-deformable contact problem in a Lagrange multiplier formulation. The discrete problem is solved via an active set strategy with a status check of multiplier and gap control values. We note that it requires a projection of the gap in the multiplier space. The use of a lumped L^2-projection has shown optimal numerical results.

The methods are referred as control point approaches as the active region of contact is defined as the support of the active multiplier functions. They are also referred as mortar-like approaches as all the constraints are

imposed weakly by the use of a Lagrange multiplier.

Multiplier spaces of different degrees have been discussed. The possibility to take different degree pairings allows a good compromise between a good displacement approximation space in each subdomain and the highest worthwhile order which can be chosen to approximate a contact problem due to its regularity limitation.

These mortar-like methods have the advantage to be less expensive than the ones which built a third mesh to lead the integral evaluation thanks to a mixed integration approach based on existing quadrature rules.

Numerical results obtained with these methods have shown a machine precision fulfilment of a constant pressure transmission as their optimality on different tests. We compared this integration approach with the slave integration one. In this later case, the impact of the approximate integration is visible on the solution (displacement and multiplier). This study has good perspectives such as a completion by theoretical studies and an extension to the nonlinear context.

Conclusions and perspectives

In this work, mixed isogeometric methods have been studied in order to design variationally consistent methods for interface problems such as mortar and contact problems. The originality of this work relies on two main aspects. First, the possibility to use different degree pairings to solve efficiently mortar and contact problems has been proved numerically. In the mortar context, we have also developed a formal theory. Secondly, even though the evaluation of the mixed terms requires, in principle, the definition of a merged mesh, an alternative integration approach that bypasses the construction of this mesh has been proposed and analysed in both cases.

Let us now discuss the possible perspectives to this work, some being already ongoing ones. In the mortar context, the future work may be directed to the merged mesh construction for any slave and master boundary shapes in order to complete the validation of the presented process. This work is the next step of the ongoing work led with A. Buffa and M. Martinelli.

In the contact context, we mention the extension to more complete contact problems, i.e., in large deformations for which the contact boundaries are updated during the resolution process, e.g., in a Newton iteration loop. We refer to the ongoing work of A. Buffa and M. Fabre. We also mention the extension to friction problems and also self-contact ones. Furthermore, once the segmentation process would be completely effective in the mortar context, mortar-like contact methods will be designed on it. We already note that without a segmentation process as stable tools to find the spline root(s) no element approach can be considered.

To finish, we just do the following comment: method optimality has a cost even though its lack is not always observed, it is necessary to be aware of it.

Appendix - Point-wise ray-tracing and projection algorithms

In this appendix, we briefly give the contents of some point-wise tools used in the proposed methods. We refer to [92] for more details, and note that each tool involves the resolution of a non-linear problem. To do so, we considered a Newton-Raphson approach but point out that others can also be used. We present hereafter the projection operation applied to a slave point, the point inversion operation applied to either a master or a slave point, and the ray-tracing operation applied to a master point.

Projection method Let us consider a slave point $\boldsymbol{x_S}$, finding its projected point(s) $\overline{\boldsymbol{x}}_{\boldsymbol{M}}$ on the master corresponds to find the point(s) at the minimal distance to it on the master, i.e., solved the following minimisation distance problem:

$$\min_{\boldsymbol{x_M} \in \Gamma_{C,M}} d(\boldsymbol{x_S}, \boldsymbol{x_M}).$$

This problem can be expressed by the following orthogonality relation:

$$\boldsymbol{x_S}\overline{\boldsymbol{x}}_{\boldsymbol{M}}(\boldsymbol{\zeta}) \cdot \boldsymbol{t}_{\boldsymbol{\Gamma_M}}(\boldsymbol{\zeta}) = 0,$$

i.e., the vector defined by the slave point and its projected point is collinear with the master normal defined in that point, and thus orthogonal to the tangent one(s). In the two-dimensional case, it is written:

$$f_P(\boldsymbol{\zeta}) = 0,$$

with $f_P(\boldsymbol{\zeta}) = (\overline{\boldsymbol{x}}_{\boldsymbol{M}}(\boldsymbol{\zeta}) - \boldsymbol{x_S}) \cdot \boldsymbol{t}_{\boldsymbol{\Gamma_M}}(\boldsymbol{\zeta}) = (\mathbf{F}_M(\boldsymbol{\zeta}) - \boldsymbol{x_S}) \cdot \mathbf{F}'_M(\boldsymbol{\zeta})$. This non-linear problem is solved for each slave point. It results in master parametric coordinates $\boldsymbol{\zeta}$ which ensure the proper orthogonality condition.

As mentioned previously, Newton-Raphson algorithm is used to solve it, see its details for the two-dimensional case in the box below. We note that according to the initialisation of the Newton-Raphson either no solution or one solution is found, in this later case with a quadratic speed of convergence. We emphasise as it is well-known, that this algorithm is really sensible to its initialisation.

Newton-Raphson strategy

1. Initialisation of $\boldsymbol{\zeta}_0$
2. At iteration i, compute

$$\Delta\boldsymbol{\zeta}_i = \frac{f_P(\boldsymbol{\zeta}_i)}{f_P^{'}(\boldsymbol{\zeta}_i)} = \frac{(\mathbf{F}_M(\boldsymbol{\zeta}_i) - \boldsymbol{x_S}) \cdot \mathbf{F}_M^{'}(\boldsymbol{\zeta}_i)}{\mathbf{F}_M^{''}(\boldsymbol{\zeta}_i) \cdot (\mathbf{F}_M(\boldsymbol{\zeta}_i) - \boldsymbol{x_S}) + \mathbf{F}_M^{'}(\boldsymbol{\zeta}_i) \cdot \mathbf{F}_M^{'}(\boldsymbol{\zeta}_i)}$$

3. Update the solution $\boldsymbol{\zeta}_{i+1}$ as $\boldsymbol{\zeta}_{i+1} = \boldsymbol{\zeta}_i - \Delta\boldsymbol{\zeta}_i$
4. Check convergence with one of the two following relations:
   - point coincidence $\quad \|(\mathbf{F}_M(\boldsymbol{\zeta}_i) - \boldsymbol{x_S})\| \leq \varepsilon_1$
   - zero cosine $\quad \dfrac{|(\mathbf{F}_M(\boldsymbol{\zeta}_i) - \boldsymbol{x_S}) \cdot \mathbf{F}_M^{'}(\boldsymbol{\zeta}_i)|}{\|(\mathbf{F}_M(\boldsymbol{\zeta}_i) - \boldsymbol{x_S})\| \|\mathbf{F}_M^{'}(\boldsymbol{\zeta}_i)\|} \leq \varepsilon_2$

   with ε_1 and ε_2 two convergence parameters.
5. Go to 2. until convergence is reached, incrementing the iteration index i.

Newton-Raphson strategy written for the two-dimensional point projection problem.

In the three-dimensional case, i.e., for two-dimensional interface case, it results analogously for each point in a non-linear matrix system.

Point inversion method Let us consider a point $\boldsymbol{x}$, either slave or master. Finding the point $\boldsymbol{\zeta}$ in the slave parametric space, resp. master parametric space, it is the image by the slave mapping $\mathbf{F}_S$, resp. master mapping $\mathbf{F}_M$, can be done by using the projection algorithm described above. In this case the point $\boldsymbol{x}$ already belongs to the domain it is projected to. Thus its relative parametric coordinates are obtained by an achievement of a point coincidence relation in the resolution process.

Ray-tracing method Let us consider a master point $\boldsymbol{x_M}$, finding its ray-traced point $\widetilde{\boldsymbol{x}}_{\boldsymbol{S}}$ on the slave corresponds to find the point where the master

normal intersects the slave starting from this master point. This problem can be expressed by the following orthogonality relation:

$$\widetilde{\boldsymbol{x}}_{\boldsymbol{S}}(\boldsymbol{\zeta})\boldsymbol{x}_{\boldsymbol{M}} \cdot \boldsymbol{t}_{\boldsymbol{\Gamma}_{\boldsymbol{M}}} = 0,$$

i.e., the vector defined by the master point and its ray-traced point is collinear with the master normal defined in that point, and orthogonal to the tangent one(s), which can be written:

$$f_R(\boldsymbol{\zeta}) = 0,$$

with $f_R(\boldsymbol{\zeta}) = (\boldsymbol{x}_{\boldsymbol{M}} - \widetilde{\boldsymbol{x}}_{\boldsymbol{S}}(\boldsymbol{\zeta})) \cdot \boldsymbol{t}_{\boldsymbol{\Gamma}_{\boldsymbol{M}}} = -(\boldsymbol{x}_{\boldsymbol{M}} - \mathbf{F}_S(\boldsymbol{\zeta})) \cdot \mathbf{F}'_M$ in the two-dimensional case. This latter problem is the non-linear problem that is solved for each master point. It results in slave parametric coordinates $\boldsymbol{\zeta}$ which ensure the proper orthogonality condition.

In the case this non-linear problem is solved with Newton-Raphson algorithm, the specific computation of $\Delta\boldsymbol{\zeta}_i$ is:

$$\Delta\boldsymbol{\zeta}_i = \frac{f_R(\boldsymbol{\zeta}_i)}{f'_R(\boldsymbol{\zeta}_i)} = \frac{-(\boldsymbol{x}_{\boldsymbol{M}} - \mathbf{F}_S(\boldsymbol{\zeta})) \cdot \mathbf{F}'_M}{\mathbf{F}'_S(\boldsymbol{\zeta}_i) \cdot \mathbf{F}'_M},$$

and the convergence check relations are:

- point coincidence $\quad \|(\boldsymbol{x}_{\boldsymbol{M}} - \mathbf{F}_S(\boldsymbol{\zeta}))\| \leq \varepsilon_1,$
- zero cosine $\quad \dfrac{|(\boldsymbol{x}_{\boldsymbol{M}} - \mathbf{F}_S(\boldsymbol{\zeta})) \cdot \mathbf{F}'_M|}{\|(\boldsymbol{x}_{\boldsymbol{M}} - \mathbf{F}_S(\boldsymbol{\zeta}))\|\|\mathbf{F}'_M\|} \leq \varepsilon_2.$

The three-dimensional case is also analogously treated with a non-linear matrix system for each point.

Remark 21. *We note that in the case Newton-Raphson algorithm does not converge, refining the boundary domain on which a point is either projected or ray-traced may improve the algorithm behaviour as it is initialised to the knot which has the closest image to the point on the domain. This refinement procedure is obviously done only in the determination of the projected, resp. ray-traced, point purpose and thus is not affecting the approximation space. Classical improvement strategies to ensure a convergence of the Newton-Raphson algorithm can also be used.*

Bibliography

[1] P. Alart and A. Curnier. "A mixed formulation for frictional contact problems prone to Newton like solution methods." In: *Comput. Methods Appl. Mech. Eng.* 92.3 (1991), pp. 353–375.

[2] T. Apel, A-M. Sändig, and J.R. Whiteman. "Graded Mesh Refinement and Error Estimates for Finite Element Solutions of Elliptic Boundary Value Problems in Non-smooth Domains". In: *Math. Methods Appl. Sci.* 19.1 (1996), pp. 63–85.

[3] A. Apostolatos, M. Breitenberger, R. Wüchner, and K-U. Bletzinger. "Domain Decomposition Methods and Kirchhoff-Love Shell Multipatch Coupling in Isogeometric Analysis". In: *Isogeometric Analysis and Applications 2014*. Ed. by B. Jüttler and B. Simeon. Vol. 107. 2015, pp. 73–101.

[4] A. Apostolatos, R. Schmidt, R. Wüchner, and K-U. Bletzinger. "A Nitsche-type formulation and comparison of the most common domain decomposition methods in isogeometric analysis". In: *Int. J. Numer. Methods Eng.* 97.7 (2014), pp. 473–504.

[5] Y. Bazilevs, L. Beirão Da Veiga, J.A. Cottrell, T.J.R. Hughes, and G. Sangalli. "Isogeometric Analysis: Approximation, stability and error estimates for h-refined meshes". In: *Math. Models Methods Appl. Sci.* 16.7 (2006), pp. 1031–1090.

[6] L. Beirão Da Veiga, A. Buffa, G. Sangalli, and R. Vàsquez. "Mathematical analysis of variational isogeometric methods". In: *Acta Numerica* 23 (2014), pp. 157–287.

[7] L. Beirão Da Veiga, D. Cho, and G. Sangalli. "Anisotropic NURBS approximation in isogeometric analysis". In: *Comput. Methods Appl. Mech. Eng.* 209-212 (2012), pp. 1–11.

[8] F. Ben Belgacem. "The mortar finite element method with Lagrange multipliers". In: *Numer. Math.* 84.2 (1999), pp. 173–197.

[9] F. Ben Belgacem, P. Hild, and P. Laborde. "Extension of the mortar finite element method to a variational inequality modeling unilateral contact". In: *Math. Models Methods Appl. Sci.* 9.2 (1999), pp. 287–303.

[10] F. Ben Belgacem and Y. Maday. "The mortar finite element method for three dimensional finite elements". In: *Math. Model. Numer. Anal.* 31.2 (1997), pp. 289–302.

[11] C. Bernardi, Y. Maday, and A. T. Patera. "A new nonconforming approach to domain decomposition: the mortar element method". In: *Nonlinear partial differrential equations and their applications.* Ed. by H. B. et.al. Vol. XI. Collège de France. 1994, pp. 13–51.

[12] C. Bernardi, Y. Maday, and A. T. Patera. "Domain Decomposition by the Mortar Element Method". English. In: *Asymptotic and Numerical Methods for Partial Differential Equations with Critical Parameters*. Ed. by H. Kaper et. al. Vol. 384. NATO ASI Series. Springer Netherlands, 1993, pp. 269–286. ISBN: 978-94-010-4798-2.

[13] D. Boffi, F. Brezzi, and M. Fortin. *Mixed Finite Element Methods and Applications*. Berlin: Springer, 2013.

[14] P. Boieri, F. Gastaldi, and D. Kinderlehrer. "Existence, Uniqueness, and Regularity Results for the Two-Body Contact Problem". In: *Appl. Math. Optim.* 15 (1987), pp. 251–277.

[15] D. Braess. *Finite elements. Theory, fast solvers, and applications in solid mechanics*. Third. Cambridge: Cambridge University Press, 2007.

[16] D. Braess, W. Dahmen, and C. Wieners. "A Multigrid Algorithm for the Mortar Finite Element Method". In: *SIAM J. Numer. Anal.* 37 (1999), pp. 48–69.

[17] E. Brivadis, A. Buffa, B. Wohlmuth, and L. Wunderlich. "Isogeometric mortar methods". In: *Comput. Methods Appl. Mech. Eng.* 284 (2015), pp. 292–319.

[18] E. Brivadis, A. Buffa, B. Wohlmuth, and L. Wunderlich. "The Influence of Quadrature Errors on Isogeometric Mortar Methods". In: *Isogeometric Analysis and Applications 2014*. Ed. by B. Jüttler and B. Simeon. Vol. 107. 2015, pp. 33–50.

[19] S. Brunssen, F. Schmid, M. Schafer, and B. Wohlmuth. "A fast and robust method for contact problems by combining a primal-dual active set strategy and algebraic multigrid methods". In: *Int. J. Numer. Meth. Eng.* 69 (2007), pp. 524–543.

[20] F. Buchegger, B. Jüttler, and A. Mantzaflaris. "Adaptively refined multi-patch B-splines with enhanced smoothness". In: *Applied Mathematics and Computation* 272 (2016), pp. 159–172.

[21] A. Buffa, G. Sangalli, and C. Schwab. *Exponential Convergence of the hp Version of Isogeometric Analysis in 1D*. Tech. rep. 2012-39. Seminar for Applied Mathematics, ETH Zürich, 2012.

[22] A. Buffa, G. Sangalli, and R. Vàsquez. "Isogeometric analysis in electromagnetics: B-splines approximation". In: *Comput. Methods Appl. Mech. Eng.* 199.17 (2010), pp. 1143–1152.

[23] L. Cazabeau, C. Lacour, and Y. Maday. "Numerical quadrature and mortar methods". In: *Computational Science for the 21st Century*. John Wiley and Sons, 1997, pp. 119–128.

[24] D. Chapelle and K. J. Bathe. "The inf-sup test". In: *Computers and Structures* 47 (1993), pp. 537–545.

[25] F. Chouly, M. Fabre, P. Hild, J. Pousin, and Y. Renard. "Residual-based a posteriori error estimation for contact problems approximated by Nitsche's method." In: *IMA J. Numer. Anal.* submitted (2016).

[26] F. Chouly and P. Hild. "A Nitsche-based method for unilateral contact problems: numerical analysis". In: *SIAM J. Numer. Anal.* 51 (2013), pp. 1295–1307.

[27] F. Chouly, P. Hild, and Y. Renard. "Symmetric and non-symmetric variants of Nitsche's method for contact problems in elasticity : theory and numerical experiments." In: *Math. Comp.* 84 (2015), pp. 1089–1112.

[28] E. Cohen and L. Schumaker. "Rates of convergence of control polygons". In: *Comput. Aided Geom. Design* 2 (1985), pp. 229–235.

[29] A. Collin, G. Sangalli, and T. Takacs. "Approximation properties of multi-patch C1 isogeometric spaces". arXiv:1509.07619v2, Submitted. 2015.

[30] P. Cooverits, P. Hild, K. Lhalouani, and T. Sassi. "Mixed Finite Element Methods for Unilateral Problems: Convergence Analysis and Numerical Studies". In: *Mathematics of Computation* 71 (2002), pp. 1–25.

[31] J. A. Cottrell, T. J. R. Hughes, and Y. Bazilevs. *Isogeometric Analysis: Towards Integration of CAD and FEA*. Wiley, 2009.

[32] J. A. Cottrell, A. Reali, Y. Bazilevs, and T.J.R. Hughes. "Isogeometric analysis of structural vibrations". In: *Comput. Methods Appl. Mech. Eng.* 195.5257-5296 (2006).

[33] J. A. Cottrell, A. Reali, and T.J.R. Hughes. "Studies of refinement and continuity in isogeometric structural analysis". In: *Comput. Methods Appl. Mech. Eng.* 196 (2007), pp. 41–44.

[34] C. De Falco, A. Reali, and R. Vàsquez. "GeoPDEs: A research tool for isogeometric analysis of PDEs". In: *Adv. Eng. Softw.* 42(12) (2011), pp. 1020–1034.

[35] C. De Boor. *A practical guide to splines*. Ed. by Springer. Vol. 27. Applied Mathematical Sciences, 2001.

[36] C. De Boor and R. E. Lyche. "On splines and their minimum properties". In: *J. Math. Mech.* 15 (1966), pp. 953–970.

[37] L. De Lorenzis, I. Temizer, P. Wriggers, and G. Zavarise. " A large deformation frictional contact formulation using NURBS-based isogeometric analysis". In: *Int. J. Numer. Methods Eng.* 87 (2011), pp. 1278–1300.

[38] L. De Lorenzis, P. Wriggers, and T. J. R. Hughes. "Isogeometric contact: a review". In: GAMM-Mitt.37 (2014), pp. 85–123.

[39] L. De Lorenzis, P. Wriggers, and G. Zavarise. " A mortar formulation for 3D large deformation contact using NURBS-based isogeometric analysis and the augmented Lagrangian method". In: *Comput. Methods Appl. Mech. Eng.* 49 (2012), pp. 1–20.

[40] T. Dickopf and R. Krause. "Efficient simulation of multi-body contact problems on complex geometries: A flexible decomposition approach using constrained minimization". In: *Int. J. Numer. Meth. Eng.* 77 (2009), pp. 1834–1862.

[41] R. Dimitri, L. De Lorenzis, M. A. Scott, P. Wriggers, R. L. Taylor, and G. Zavarise. "Isogeometric large deformation frictionless contact using T-splines". In: *Comput. Methods Appl. Mech. Eng.* 269 (2014), pp. 394–414.

[42] M. Dittmann, M. Franke, I. Temizer, and C. Hesch. "Isogeometric Analysis and thermomechanical Mortar contact problems". In: *Comput. Methods Appl. Mech. Eng.* 274 (2014), pp. 192–212.

[43] W. Dornisch, G. Vitucci, and S. Klinkel. "The weak substitution method - an application of the mortar method for patch coupling in NURBS-based isogeometric analysis". In: *Int. J. Numer. Methods Eng.* 00 (2014). DOI: 10.1002/nme.4918, pp. 1–30.

[44] N. El-Abbasi and K. J. Bathe. "Stability and patch test performance of contact discretizations and a new solution algorithm". In: *Computers and Structures* 79.1473-1486 (2001).

[45] A. Ern and J.L. Guermond. *Theory and Practise of Finite Elements*. Springer, 2004.

[46] M. Fabre, J. Pousin, and Y. Renard. "A fictitious domain method for frictionless contact problems in elasticity using Nitsche's method". In: *SMAI J. of Comput. Math.* 2.19-50 (2016).

[47] P. Farah, A. Popp, and W. A. Wall. "Segment-based vs. element-based integration for mortar methods in computational contact mechanics". In: *Comput. Mech.* DOI 10.1007/s00466-014-1093-2 (2014).

[48] K.A. Fischer and P. Wriggers. "Frictional 2D contact formulation for finite deformations based on the mortar method". In: *Comput. Mech.* 36 (2005), pp. 226–244.

[49] M. Fortin and R. Glowinski. *Augmented Lagrangian Methods: applications to the numerical solution of boundary-value problems*. Elsevier, 1983.

[50] R. Glowinski, J.L. Lions, and R. Trémolières. *Numerical analysis of variational inequalities*. Vol. 8. North-Holland Publishing Company, 1981.

[51] P. Grisvard. *Elliptic Problems in Nonsmooth Domains*. Philadelphia: SIAM, 2011.

[52] J. Haslinger, I. Hlaváček, and J. Nečas. "Numerical Methods for Unilateral problems in Solid Mechanics". In: Handbook of Numerical Analysis, Volume IV, Part 2 (1996), pp. 313–485.

[53] C. Hesch and P. Betsch. "Isogeometric analysis and domain decomposition methods". In: *Comput. Methods Appl. Mech. Eng.* 213–216 (2012), pp. 104–112.

[54] C. Hesch, M. Franke, M. Dittmann, and I. Temizer. "Hierarchical NURBS and a higher-order phase-field approach to fracture for finite-deformation contact problems". In: *Comput. Methods Appl. Mech. Eng.* 301 (2016), pp. 242–258.

[55] P. Hild. "Numerical Implementation of Two Nonconforming Finite Element Methods for Unilateral Contact". In: *Comput. Methods Appl. Mech. Eng.* 184.99-123 (2000).

[56] P. Hild and P. Laborde. "Quadratique Finite Element Methods for Unilateral Contact Problems". In: *Appl. Numer. Math.* 41 (2002), pp. 401–421.

[57] M. Hintermüller, K. Ito, and K. Kunisch. "The primal-dual active set strategy as a semismooth Newton Method". In: *SIAM J. Numer. Anal.* 13.3 (2003), pp. 865–888.

[58] I. Hlaváček, J. Haslinger, J. Nečas, and J. Lovisek. *Solution of variational inequalities in Mechanics*. Springer, 1988.

[59] S. Hüeber and B. Wohlmuth. "A primal–dual active set strategy for non-linear multibody contact problems". In: *Comput. Methods Appl. Mech. Eng.* 194 (2005), pp. 3147–3166.

[60] T. J. R. Hughes, J. A. Cottrell, and Y. Bazilevs. "Isogeometric analysis: CAD, finite elements, NURBS, exact geometry and mesh refinement". In: *Comput. Methods Appl. Mech. Eng.* 194.39-41 (2005), pp. 4135–4195.

[61] T.J.R. Hughes, J. A. Evans, and A. Reali. "Finite element and nurbs approximations of eigenvalue, boundary-value, and initial-value problems." In: *Comput. Methods Appl. Mech. Eng.* 272 (2014), pp. 290–320.

[62] K. Ito and K. Kunisch. *Lagrange multiplier approach to variational problems and applications*. SIAM, 2008.

[63] K.L. Johnson. *Contact Mechanics*. Cambridge University Press, 1987.

[64] M. Kapl, F. Buchegger, M. Bercovier, and B. Jüttler. "Isogeometric analysis with geometrically continuous functions on planar multi-patch geometries". In: *Comput. Methods Appl. Mech. Eng.* (2016), in press.

[65] M. Kapl, V. Vitrih, B. Jüttler, and K. Birner. "Isogeometric analysis with geometrically continuous functions on two-patch geometries". In: *Computers and Mathematics with Applications* 70 (2015), pp. 1518–1538.

[66] N. Kikuchi and J.T. Oden. *Contact Problems in elasticity. A Study of Variational Inequalities and Finite Elemnt Methods*. SIAM, 1988.

[67] J.-Y. Kim and S.-K. Youn. "Isogeometric contact analysis using mortar method". In: *Int. J. Numer. Methods Eng.* 89.12 (2012), pp. 1559–1581.

[68] S. K. Kleiss, C. Pechstein, B. Jüttler, and S. Tomar. "IETI - Isogeometric Tearing and Interconnecting". In: *Comput. Methods Appl. Mech. Eng.* 247-248 (2012), pp. 201–215.

[69] R. Krause and B. Wohlmuth. "Nonconforming domain decomposition techniques for linear elasticity." In: *East-West J. Numer. Math.* 8.3 (2000), pp. 177–206.

[70] B. Lamichhane. "Higher Order Mortar Finite Elements with Dual Lagrange Multiplier Spaces and Applications". PhD thesis. Universität Stuttgart, 2006.

[71] B. Lamichhane and B. Wohlmuth. "Biorthogonal Bases with Local Support and Approximation Properties". In: *Math. Comp.* 76 (2007), pp. 233–249.

[72] U. Langer and E. Moore. *Discontinuous Galerkin isogeometric analysis of elliptic PDEs on surfaces*. Tech. rep. 01. RICAM report, 2014.

[73] T.A. Laursen. *Computational Contact and Impact Mechanics*. Springer, 2002.

[74] T.A. Laursen and J.C. Simo. "A continuum-based Finite Element formulation for the implicit solution of multibody, large deformation frictional contact problems". In: *Int. J. Numer. Meth. Eng.* 36 (1993), pp. 3451–3485.

[75] P. Le Tallec. *Modélisation et calcul des milieux continus*. Ellipses, 2009.

[76] J. Li, J. M. Melenk, B. Wohlmuth, and J. Zou. "Optimal A Priori Estimates for Higher Order Finite Elements for Elliptic Interface Problems". In: *Appl. Numer. Math.* 60 (2010), pp. 19–37.

[77] S. Lipton, J. A. Evans, Y. Bazilevs, T. Elguedj, and T.J.R. Hughes. "Robustness of isogeometric structural discretizations under severe mesh distortion". In: *Comput. Methods Appl. Mech. Eng.* 199.5 (2010), pp. 357–373.

[78] J. Lu. "Isogeometric contact analysis: Geometric basis and formulation for frictionless contact". In: *Comput. Methods Appl. Mech. Eng.* 200 (2011), pp. 726–741.

[79] A.A Lubrecht. *An introduction to ElastoHydrodynamic Lubrication*. INSA Lyon. Course in the department of mechanical engineering and development, 2009.

[80] T. Lyche and K. Morken. *Spline methods*. University of Oslo. Course in the department of informatics, 2011.

[81] Y. Maday, F. Rapetti, and B. I. Wohlmuth. "The influence of quadrature formulas in 2D and 3D mortar element methods." English. In: *Recent developments in domain decomposition methods. Some papers of the workshop on domain decomposition, ETH Zürich, Switzerland, June 7–8. 2001*. Springer, 2002, pp. 203–221. ISBN: 3-540-43413-5.

[82] A. E. Maliki, M. Fortin, N. Tardieu, and A. Fortin. "Iterative solvers for 3D linear and nonlinear elasticity problems: Displacement and mixed formulations". In: *Int. J. Numer. Meth. Eng.* 83 (2010), pp. 1780–1802.

[83] A. El Maliki, M. Fortin, J. Deteix, and A. Fortin. "Preconditioned iteration for saddle-point systems with bound constraints arising in contact problems". In: *Comput. Methods Appl. Mech. Eng.* 254 (2013), pp. 114–125.

[84] L. Marcinkowski. "A Balancing Domain Decomposition Method for a Discretization of a Plate Problem on Nonmatching Grids". In: *Parallel Processing and Applied Mathematics*. Ed. by Roman Wyrzykowski, Jack Dongarra, Konrad Karczewski, and Jerzy Wasniewski. Lecture Notes in Computer Science. Berlin: Springer, 2010, pp. 70–79.

[85] L. Marcinkowski. "A mortar element method for some discretizations of a plate problem". In: *Numer. Math.* 93.2 (2002), pp. 361–386.

[86] T.W. McDevitt and T.A. Laursen. "A mortar-finite element formulation for frictional contact problems". In: *Int. J. Numer. Meth. Eng.* 48 (2000), pp. 1525–1547.

[87] J. M. Melenk and B. Wohlmuth. "Quasi-optimal approximation of surface based Lagrange multipliers in finite element methods". In: *SIAM J. Numer. Anal.* 50.4 (2012), pp. 2064–2087.

[88] S. Morganti, F. Auricchio, D.J. Benson, F.I. Gambarin, S. Hartmann, T.J.R. Hughes, and A. Reali. "Patient-specific isogeometric structural analysis of aortic valve closure". In: *Comput. Methods Appl. Mech. Eng.* 284 (2015), pp. 508–520.

[89] M. Moussaoui and K. Khodja. "Régularité des solutions d'un problème mêlé Dirichlet–Signorini dans un domaine polygonal plan". In: *Commun. Partial Differ. Equ.* 17 (1992), pp. 805–826.

[90] V. P. Nguyen, P. Kerfriden, M. Brino, S. Bordas, and E. Bonisoli. "Nitsche's method for two and three dimensional NURBS patch coupling". In: *Comput. Mech.* 53 (2014), pp. 1163–1182.

[91] P. Oswald and B.I. Wohlmuth. "On polynominal reproduction of dual FE bases". In: *Domain Decomposition Methods in Science and Engineering*. Ed. by N. Debit, M. Garbey, R.H.W. Hoppe, D. Keyes, Y. Kuznetsov, and J. Périaux. 13th International Conference on Domain Decomposition Methods, Lyon, France. CIMNE, 2002, pp. 85–96.

[92] L. Piegl and W. Tiller. *The NURBS Book*. Springer, 1997.

[93] G. Pietrzak and A. Curnier. "Large deformation frictional contact mechanics: continuum formulation and augmented Lagrangian treatment". In: *Comput. Methods Appl. Mech. Eng.* 177 (1999), pp. 351–381.

[94] A. Popp and W.A. Wall. "Dual mortar method for computational contact mechanics - overview and recent developments". In: *Gamm Mitt* 1 (2014), pp. 66–84.

[95] M.A. Puso. "A 3D mortar method for solid mechanics". In: *Int. J. Numer. Meth. Eng.* 59 (2004), pp. 315–336.

[96] M.A. Puso and T.A. Laursen. "A mortar segment-to-segment contact method for large deformation solid mechanics". In: *Comput. Methods Appl. Mech. Eng.* 193 (2004), pp. 601–629.

[97] Y. Renard. "Generalized Newton's methods for the approximation and resolution of frictional contact problems in elasticity." In: *Comput. Methods Appl. Mech. Eng.* 256 (2013), pp. 38–55.

[98] D.F. Rogers. *An Introduction to NURBS With Historical Perspective,* Academic Press, San Diego, CA, 2001.

[99] M. Ruess, D. Schillinger, A. I. Ozcan, and E. Rank. "Weak coupling for isogeometric analysis of non-matching and trimmed multi-patch geometries". In: *Comput. Methods. Appl. Mech. Eng.* 269 (2014), pp. 46–71.

[100] L. Schumaker. *Spline Functions: Basic Theory*. Third. Cambridge: Cambridge University Press, 2007.

[101] C. Schwab. *p- and hp- Finite Element Methods: Theory and Applications in Solid and Fluid Mechanics*. Oxford Univ. Press, 1998.

[102] A. Seitz, P. Farah, J. Kremheller, B. I. Wohlmuth, W. A. Wall, and A. Popp. "Isogeometric dual mortar methods for computational contact mechanics". In: *Comput. Methods Appl. Mech. Eng.* 301 (2016), pp. 259–280.

[103] R.L. Taylor and P. Papadopoulos. "On a Patch Test for Contact Problems in Two Dimensions". In: (1991). Ed. by Spinger-Verlag, pp. 690–702.

[104] I. Temizer, P. Wriggers, and T. J. R. Hughes. "Three-dimensional mortar-based frictional contact treatment in isogeometric analysis with NURBS". In: *Comput. Methods Appl. Mech. Eng.* 209-212 (2012), pp. 115–128.

[105] I. Temizer, P. Wriggers, and T.J.R. Hughes. "Contact treatment in isogeometric analysis with NURBS". In: *Comput. Methods Appl. Mech. Eng.* 200 (2011), pp. 1100–1112.

[106] S. Timoshenko and J. N. Goodier. *Theory of elasticity*. New York: Mc Graw-Hill, 1951.

[107] S. Triebenbacher, M. Kaltenbacher, B. Wohlmuth, and B. Flemisch. "Applications of the Mortar Finite Element Method in Vibroacoustics and Flow Induced Noise Computations". In: *Acta Acust. united Ac.* 96.3 (2010), pp. 536–553.

[108] M. Tur, F.J. Fuenmayor, and P. Wriggers. "A mortar-based frictional contact formulation for large deformations using Lagrange multipliers". In: *Comput. Methods Appl. Mech. Eng.* 198 (2009), pp. 2860–2873.

[109] R. Vàsquez. "A new design for the implementation of isogeometric analysis in Octave and Matlab: GeoPDEs 3.0". In: *Comput. Methods Appl. Mech. Eng.* 72 (2016), pp. 523–554.

[110] L. Wahlbin. *Superconvergence in Galerkin Finite Element Methods*. Lecture Notes in Mathematics 1605. Berlin: Springer, 1995.

[111] B. Wohlmuth. *Discretization Methods and Iterative Solvers Based on Domain Decomposition*. Lecture Notes in Computational Science and Engineering 17. Berlin: Springer, 2001.

[112] B. Wohlmuth. "Variationally consistent discretization schemes and numerical algorithms for contact problems". In: *Acta Numerica* 20 (2011), pp. 569–734.

[113] B. Wohlmuth and R. H. Krause. "Monotone multigrid methods on nonmatching grids for nonlinear multibody contact problems". In: *SIAM J. Numer. Anal.* 25.1 (2003), pp. 324–247.

[114] B. Wohlmuth, A. Popp, M.W. Gee, and W.A. Wall. "An abstract framework for a priori estimates for contact problems in 3D with quadratic finite elements". In: *Comput. Mech.* 49 (2012), pp. 735–747.

[115] P. Wriggers. *Computational Contact Mechanics*. 2nd ed. Berlin: Springer, 2006.

[116] J. Xu, F. Chen, and J. Deng. "Two-dimensional domain decomposition based on skeleton computation for parameterization and isogeometric analysis". In: *Comput. Methods Appl. Mech. Eng.* (2016), to appear.

[117] X. Xu, L. Li, and W. Chen. "A Multigrid Method for the Mortar-type Morley Element Approximation of a Plate Bending Problem". In: *SIAM J. Numer. Anal.* 39.5 (2002), pp. 1712–1731.

[118] M. Zarroug. "Elements de contact frottant et applications". PhD thesis.

[119] L. Zhen, F. Gillot, and L. Jezequel. "A C0/G1 multiple patches connection method in isogeometric analysis". In: *Applied Mathematical Modeling* 39.15 (2015), pp. 4405–4420.